



UNIVERSITÀ DEGLI STUDI DI TRIESTE

SEDE AMMINISTRATIVA DEL DOTTORATO DI RICERCA

XXI CICLO DEL
DOTTORATO DI RICERCA IN
FISICA

High frequency dynamics of fluid binary mixtures

(Settore scientifico-disciplinare FIS/03–Fisica della Materia)

DOTTORANDA

Maria Grazia Izzo

Coordinatore corso di Dottorato

Prof. Gaetano Senatore

Relatore

Prof. Giorgio Pastore

Correlatore

Dr. Claudio Masciovecchio

Anno accademico 2008-2009

Contents

Introduction	1
1 Collective modes and fluid dynamics	9
1.1 Fluid dynamics: time correlation functions	9
1.1.1 Static correlation functions	14
1.1.2 Frequency sum rules	16
1.2 Classical Hydrodynamics	18
1.2.1 Hydrodynamics of single component fluids	19
1.2.2 Hydrodynamics of binary mixtures	24
1.2.2.1 Neutral systems	25
1.2.2.2 "Hydrodynamic" description of fast and slow sound modes?	28
1.2.2.3 Ionic systems	31
1.3 Mesoscopic region: the memory function approach	37
1.3.1 One-component systems: the case of density fluctuations . .	39
1.3.2 Generalization to binary mixtures	45
1.3.3 Optic-like modes and viscoelastic model in binary ionic systems	48
1.4 Single particle limit	49

2	Inelastic Scattering from fluids	55
2.1	Cross section for a scattering process	56
2.1.1	Inelastic Neutron Scattering	60
2.1.2	Inelastic X-Ray Scattering	61
2.1.3	INS vs IXS	63
2.2	Inelastic scattering from a binary mixture	68
2.3	IXS spectrometer: beamline ID-28 at ESRF	69
2.4	INS spectrometer: BRISP at ILL	74
2.5	Experimental setup	78
2.5.1	The high-pressure cell	80
2.5.2	Low temperature assembly for <i>He/Ne</i> mixture	82
2.5.3	The high-temperature Nb cell	82
3	The Helium/Neon mixtures from the mesoscopic to the single particle regimes	85
3.1	The IXS experiment	85
3.2	Ancillary measurements	87
3.3	Mesoscopic regime: data analysis	88
3.3.0.1	Model function for <i>He</i> in the mesoscopic region	90
3.3.0.2	Model function for <i>He/Ne</i> mixtures in the meso- scopic region	91
3.4	Mesoscopic region: experimental results	94
3.4.1	Longitudinal Current Spectra	97
3.4.2	Zero order memory function	99
3.4.3	Higher order memory function	104
3.4.4	Sound velocities	104
3.4.5	Relaxation times	108
3.4.6	Viscosity	116

3.5	Single particle regime	120
3.5.1	Data analysis	121
3.5.2	Experimental results	126
4	From hydrodynamic to kinetic modes: crossover region in molten	
	<i>RbF</i>	129
4.1	The INS experiment	129
4.1.1	Ancillary measurements	130
4.1.2	Data analysis	131
4.1.3	Experimental results	134
4.1.3.1	A ionic mixture in the two-component regime? . .	136
4.1.3.2	Thermal fluctuations kinetic mode and GCM ap- proach	139
	Conclusions	143

Introduction

Atoms or molecules that make up a gas or liquid are in constant motion. The motion of one particle may influence its neighbors, producing large-scale collective motions in which particles behave in a coordinated fashion. In 1986 [1], on the basis of computer simulation, it was shown that a liquid consisting of two components, one made up of lightweight particles and the other of heavy particles, would have, at sufficiently short wavelength, a special collective mode that travels through the mixture like a sound wave but at a speed faster than that of ordinary sound in the mixture (adiabatic sound speed). This novel type of internal motion has been dubbed “fast sound”. The heavier component of the mixture has been later [2, 3] considered to support a second acoustic excitation, experimentally observed, and dispersing with a sound velocity lower than the adiabatic one. The heavy and light component in the binary mixture, then, apparently behave somewhat independently. However, the details of how the constituent particles carry this type of motion are not yet completely understood.

One way to characterize the fluid mixture dynamics is the experimental determination of the fluctuations spectrum over the largest possible frequency (ω) and momentum (Q) range¹. This can be achieved by measuring the dynamic structure

¹ Q and ω are the variables Fourier conjugate of the space, \mathbf{r} , and the time, t , respectively.

factor $S(\mathbf{Q}, \omega)$. It is the time and space Fourier transform of density fluctuation correlation function. In fact, in the case of binary mixtures and, more generally, for complex fluids, the return to thermodynamic equilibrium after a fluctuation is characterized by more than one time scale, τ_α . The major sensibility of $S(Q, \omega)$ to the relaxation process associated to τ_α is obtained at momentum Q : $\omega(Q)\tau_\alpha \sim 1$. For such systems it is therefore crucial to investigate the dynamic structure factor in a frequency and momentum range enough large in order to characterize all the dynamics of the system.

In a one-component fluid the average time for intermolecular interactions, τ (usually in the *ps* range) and the corresponding average intermolecular correlation length, λ (usually of the same order as the mean free path, i.e. a few *nm*) are the “special” time and length scales, which mark the border between the classical and molecular hydrodynamics. When the system is probed at (Q, ω) -values lower than $(\lambda^{-1}, \tau^{-1})$, its behavior can be described in the frame of classical hydrodynamics. In this case changes in the fluid occur so slowly that the system can be considered to be in a state of local thermodynamic equilibrium. Moreover, the knowledge of the space-time variations of a limited number of conserved variables (namely: particle number, momentum and energy) are sufficient to characterize the thermodynamic state of the system. The fluid dynamics is then fully determined by thermodynamic parameters and macroscopic transport coefficients, while information on the underlying microscopic (i.e., inter- and intra-molecular) processes cannot be directly determined. As general result, the dynamics of density fluctuations in this regime is characterized by the presence of a few collective modes such as, e.g., longitudinal acoustic modes propagating with the adiabatic sound velocity and non-propagating thermal and/or interdiffusion modes. When the condition of slow variation is not fully satisfied, one can expect deviations in the fluid behavior with respect to the hydrodynamic expectations. The magnitude of such deviations

increases up to become the leading dynamical features when the probed (Q, ω) -range is of the same order as $(\lambda^{-1}, \tau^{-1})$, i.e. in the so-called mesoscopic region [4]. Despite there are no assessed theoretical framework able to provide an analytical description of the dynamics in the mesoscopic regime, it is possible to extend the hydrodynamic results by replacing the thermodynamic quantities and transport coefficients by functions varying in both space and time. This frame, usually referred to as a generalized hydrodynamics, relies upon the basic phenomenological observation that the departure from classical hydrodynamics is rather smooth. A formal approach to generalized hydrodynamics is provided by the memory function formalism introduced by Zwanzig and Mori [5], which is based on the generalized Langevin Equation. The explicit calculation of $S(\mathbf{Q}, \omega)$, however, needs suitable approximations. These can be introduced either by making an ansatz for the analytical shape of memory function or by numerically solving the generalized Langevin Equation in the Markovian approximation [6]. Both approaches predict the existence of collective modes in the density fluctuations spectrum, a subset of which can be viewed as an extension of classical hydrodynamic modes to the mesoscopic region. Several experimental data from single component fluids, both in the liquid and gaseous phase, were interpreted using such a generalized hydrodynamics frame.

For more complex systems, such as disparate mass fluid binary mixtures, other characteristic length and time scales can affect the dynamic behavior of the system. In the more general statement the relaxation process of density fluctuations towards thermodynamic equilibrium can be characterized by (at least) three distinct time-scales [7]:

- the Maxwellization time, τ_M , which, is a global measure of the relaxation timescale for density fluctuations following a mechanical perturbation. τ_M can be, in a first approximation, estimated from the average time between

intermolecular collisions in the mixture;

- the collisional relaxation time, τ_{coll} , of the single specie. This timescale accounts, separately, for the relaxation towards equilibrium of two subsystems associated with the two mixture components. The thermodynamic parameters (e.g., temperature, average molecular velocity, etc...) characterizing these equilibrium states may be different with respect to the ones associated with the (macroscopic) thermodynamic equilibrium state of the whole system;
- the characteristic time for the equilibration of the two subsystems, τ_{Δ} , which is the time needed to reach the global thermodynamic equilibrium. Here the differences in the thermodynamic parameters among the two mixture components vanishes.

The aforementioned scales may present large differences in their actual values. For instance, in disparate mass binary mixtures kinematic effects related to inefficient kinetic energy exchanges in the collisions between particles of different species may turn into a large difference between τ_{coll} and τ_M with respect to the slower relaxation time, τ_{Δ} . Therefore the departure from classical hydrodynamics, which is expected to occur when the probed frequency is on the same order as the slower characteristic timescale, is usually represented by the condition $\omega \approx \tau_{\Delta}^{-1}$.

In such a crossover region peculiar behaviors of collective modes have been hypothesized. Among them, the “fast” and “slow” sound modes, previously introduced. The first theoretical prediction of existence of a such “double” sound propagation regime has been done in the framework of the so called “two-temperature” theory [8]. Within this frame, for $\tau_{\Delta}^{-1} < \omega < \tau_M^{-1}$, following a Chapman-Enskog type procedure [9] a generalized “hydrodynamic set” of equations, which allow a temperature difference between the two species subsets, can be derived. The

initial deviations from classical hydrodynamics can be then regarded as momentum and temperature relaxations processes between these subsets. As a result, a “double” sound propagation occurring at frequencies higher than a certain critical value was predicted in a disparate-mass gaseous mixture (*He/Xe*) [10]. Qualitatively similar results have been obtained by Campa and Cohen [11, 12]. They derived the lineshape of $S(\mathbf{Q}, \omega)$ through the calculation of the eigenvalues of the pseudo-Liouville-operator for hard spheres. Again, at sufficiently high frequencies the eigenmodes results in two propagating modes. One of them can be regarded as an extension of ordinary longitudinal sound mode, whereas the second one, of kinetic character, can be identified with the “fast sound” mode, which is prevalently supported by the lighter particles subset. This approach seems to be not limited to disparate gaseous mass mixtures, but it also holds for systems with liquid-like density and small mass ratio. To this respect it is also to notice that an “hydrodynamic” approach similar to that one of “two-temperature” theory can be also applied to a generic fluid [13].

Experimental evidences of two coexisting modes principally come from inelastic scattering experiments and molecular dynamics simulations performed on nobles gas mixtures [2] (in particular on *He/Ne* mixtures [14–16]) and molten alloy, such as *Li₄Pb* [1, 17]. The experimental contribution to the understanding of this kind of dynamics is, however, quite limited, both because of the difficulties in discerning two simultaneous excitations in the spectra [18] and because of the limited Q -range accessible by most of instruments [19]. These limitations often avoided the possibility to experimentally corroborate theoretical predictions [14–16]. These difficulties are got worse by the lack of a well assessed phenomenological model to be used to evaluate the experimental spectra from binary mixtures in the mesoscopic region. One of the aim of the present work is to test the reliability of a data analysis procedure based on the generalization of the memory function

formalism to binary mixtures [20]. Despite of this formalism has been extensively used to derive a large amount of information about the relaxation dynamics in single component (both atomic and molecular) fluids in the mesoscopic range [21–23], its extension to binary mixture was never used to evaluate experimental data.

So far experimental investigations on fluid binary mixtures were accomplished in the intermediate Q region, where the condition $\omega\tau_\Delta \sim 1$ is met, and focused on the detection of fast and slow sound modes and characterization of their dispersion. Despite of the relevance of such kind of investigation, precious information on the equilibration process can be obtained by investigating the high Q -region, where the so-called Impulse Approximation (IA) [24] is met. In such an asymptotic high- Q limit the scattering process can be approximated by an (almost free) recoil of the target particle. As a consequence, $S(\mathbf{Q}, \omega)$ can be straightforwardly related to the particle momentum distribution function, $n(P)$. In the case of binary mixtures the knowledge of $n(P)$ can provide precious information on the underlying physical mechanism ruling the microscopic dynamics. In fact, one can separate the two distinct contributions related to the momentum distribution functions of both mixtures components. It can be, then, hypothesized that the peculiar equilibration process of disparate mass binary mixtures, i.e Maxwellization followed by temperature particles subsets equilibration, can fingerprint the probed momentum distributions. A second part of the experimental work done on the *He/Ne* mixtures is focused to the study of the momentum distributions by analysis of their dynamic structure factors in IA region.

The study of dynamics in binary mixtures with long-range potential interaction between particles is approached in the last part of the thesis. The chosen prototype sample is molten *RbF* (melting temperature ~ 1100 K). Experimental data in the Q -range ($2 \div 11$ nm⁻³) at the crossover between the hydrodynamic

and mesoscopic region were obtained by Inelastic Neutron Scattering (INS). Ionic systems are characterized by the long-range Coulomb interaction potential. The main difference with respect to electrically neutral mixtures, as $He_{0.8}Ne_{0.2}$, relies upon the fact that in ionic systems the Coulomb force acts as a restoring force for mass-concentration fluctuations. In the low- Q range it is possible to distinguish between two regimes, depending on the values of electric conduction coefficient, σ , and adiabatic sound velocity, c_s . If $4\pi\sigma/\epsilon \ll c_s Q$, where ϵ is the dielectric constant of the system, the so-called two-components regime is met. Here the dynamics of ionic mixtures is isomorphous to a neutral one with electric conduction playing the role of interdiffusion. In the opposite limit, i.e. when $4\pi\sigma/\epsilon \gg c_s Q$ (Kubo regime), concentration fluctuations are decoupled from the other dynamical variables, which are associated to collective modes in analogy with the case of single-component fluid. In case the Q -value marking the border between hydrodynamic and mesoscopic regions falls in the Kubo regime, the existence of an optic-like kinetic mode associated with concentration fluctuations was inferred [25]. This mode is observable only in the mesoscopic region, since its intensity vanishes at low- Q . However, only a few experimental evidences of such a mode are reported in literature [26, 27]. The possible existence of collective kinetic modes in the mesoscopic region for binary mixtures is also supported by computation results obtained using the generalized collective mode approach [6, 28–31]. This framework furnishes an unified description of collective dynamics in binary mixtures (both ionic and neutral) and hypothesize an optic-like nature for fast sound in both ionic and neutral systems, if suitable conditions for transport coefficients are fulfilled [31].

The thesis is set out as described in the following:

- Chapter 1 is devoted to the description of fluid dynamics for both one and two-component systems. The analytical results concerning the hydrodynam-

ics and single particle limit are discussed. Particular emphasis is given to the decoupled sound propagation phenomenon and to the memory function formalism generalized to binary mixtures. This formalism will be directly used for the first time to analyze experimental data from He/Ne mixtures in the mesoscopic regime.

- Chapter 2 discusses the general principles of inelastic scattering spectroscopy and, more specifically, the employed techniques: i.e. Inelastic X-ray (IXS) and Neutron scattering (INS). In this chapter we also report on the experimental setup we used in order to perform the various experiments.
- Chapter 3 presents and discuss the experimental data, the data analysis and the results obtained by IXS on fluid He/Ne mixtures. Both the mesoscopic and IA regimes were investigated. The observed behavior was cast in a common framework, essentially based on the “two temperature approach”.
- Chapter 4 reports the INS experiment on RbF. The obtained results are qualitatively discussed in the “two temperature” and in the generalized collective mode frame.

Collective modes and fluid dynamics

1.1 Fluid dynamics: time correlation functions

The measurable properties of a fluid can be related to its microscopic dynamics through time correlation functions. The latter are space-time functions which describe the thermal fluctuations occurring in a fluid in thermodynamic equilibrium. These fluctuations occur at different time and length scales, and they also can describe the response of the fluid to a weak external perturbation. This response can be directly measured by inelastic scattering techniques. Through these experiments it is then possible to understand the molecular origin of transport coefficients and generalize them when the fluid is perturbed at high frequency and short wavelength.

The fluid can be identified with a statistical mechanical system of volume V containing N particles of mass M . There are no external field imposed on the system, so it will be invariant to spatial translation, rotation, inversion and time translation. The system Hamiltonian has, therefore, the form:

$$\mathbf{H} = \sum_{j=1,N} \frac{\mathbf{P}_j^2}{2M} + \frac{1}{2} \sum_{j \neq l}^{1,N} v(|\mathbf{R}_j - \mathbf{R}_l|), \quad (1.1)$$

where \mathbf{R}_j and \mathbf{P}_j denote the position and momentum of particle j and $v(|R_j - R_l|)$.

The equilibrium distribution of particle positions and momenta is assumed to be the canonical ensemble.

A dynamical variable $\mathbf{A}(\mathbf{r}, t)$ is a function of the $6N$ -dimensional phase coordinate, $\Gamma = \{\mathbf{R}_1, \dots, \mathbf{R}_N, \mathbf{P}_1, \dots, \mathbf{P}_N\}$. A general time correlation function is defined as:

$$C_{BA}(\mathbf{r}, t, \mathbf{r}', t') = V \langle \delta A(\mathbf{r}', t') \delta B(\mathbf{r}, t) \rangle = C_{BA}(|\mathbf{r} - \mathbf{r}'|, t - t') \equiv C_{BA}(\mathbf{r}, t), \quad (1.2)$$

where

$$\delta A(\mathbf{r}, t) = A(\mathbf{r}, t) - \langle A(\mathbf{r}, t) \rangle \quad (1.3)$$

is the fluctuation in the dynamical variable $A(\mathbf{r}, t)$ and $\langle \dots \rangle$ indicates the thermal average. The last equality follows from the space and time invariance of the fluid. For $t = 0$ $C_{BA}(\mathbf{r}, t)$ assumes its maximum value and it goes to zero in the limit $t \rightarrow \infty$, indicating the loss, in such a limit, of any correlation between the two variables [4].

The dynamical variables of particular interest in the study of microscopic dynamics in single component fluids are the number density:

$$n(\mathbf{r}, t) = \frac{1}{\sqrt{N}} \sum_{j=1, N} \delta(\mathbf{r} - \mathbf{R}_j(t)), \quad (1.4)$$

the current density:

$$j(\mathbf{r}, t) = \frac{1}{\sqrt{N}} \sum_{j=1, N} \mathbf{v}_j(t) \delta(\mathbf{r} - \mathbf{R}_j(t)), \quad (1.5)$$

and the single particle density:

$$n_s(\mathbf{r}, t) = \delta(\mathbf{r} - \mathbf{R}_1(t)). \quad (1.6)$$

In the case of binary mixtures another variable, the concentration fluctuation δc plays a relevant role. It is defined as:

$$c = x_2 n_1(\mathbf{r}, t) - x_1 n_2(\mathbf{r}, t), \quad (1.7)$$

with $x_{1(2)}$ and $n_{1(2)}$ the concentration and partial density, respectively, of the two specie components, labelled with subscript 1 and 2. The average values of these variables are \sqrt{N}/V , 0, $1/V$ and 0, respectively. In binary mixtures the dynamical variables, δn and δc , can be expressed also in terms of partial densities fluctuations, δn_1 and δn_2 , using the relation:

$$\begin{pmatrix} \delta \hat{n} \\ \delta \hat{c} \end{pmatrix} = \begin{pmatrix} x_1^{1/2} & x_2^{1/2} \\ x_2^{1/2} & -x_1^{1/2} \end{pmatrix} \cdot \begin{pmatrix} \delta \hat{n}_1 \\ \delta \hat{n}_2 \end{pmatrix} = \begin{pmatrix} x_1^{1/2} \delta \hat{n}_1 + x_2^{1/2} \delta \hat{n}_2 \\ x_2^{1/2} \delta \hat{n}_1 - x_1^{1/2} \delta \hat{n}_2 \end{pmatrix}, \quad (1.8)$$

The description of system dynamics in terms of δn , δc or δn_1 δn_2 is usually referred to as Bhatia-Thornton (BT) [32] or Faber-Ziman (FZ) [33] representation, respectively.

The density-density correlation function, or van Hove pair correlation function [34], can then be written as:

$$G(\mathbf{r}, t) = V \langle \delta n(\mathbf{r}, t) \delta n(\mathbf{0}, 0) \rangle = \frac{V}{N} \langle \sum_{j,l=1,N} \delta(\mathbf{r} - \mathbf{R}_j(t)) \delta(\mathbf{0} - R_l(0)) \rangle \quad (1.9)$$

Analogously the current-current pair correlation function is defined as:

$$J_{\alpha\beta}(\mathbf{r}, t) = V \langle j_\alpha(\mathbf{r}, t) j_\beta(\mathbf{0}, 0) \rangle, \quad (1.10)$$

where α and β are the cartesian indices. For spherical symmetric systems, such as fluids, only the purely longitudinal and transverse component $J_L(\mathbf{r}, t)$ and $J_T(\mathbf{r}, t)$ are meaningful [4]. The concentration and density-concentration correlation functions are defined as:

$$C(\mathbf{r}, t) = V \langle c(\mathbf{r}, t) c(\mathbf{0}, 0) \rangle, \quad (1.11)$$

$$P(\mathbf{r}, t) = V \langle n(\mathbf{r}, t) c(\mathbf{0}, 0) \rangle, \quad (1.12)$$

The variable $n_s(\mathbf{r}, t)$ describes the localization of a given particle. The respective correlation function, the so called van Hove self-correlation function, is:

$$G_s(\mathbf{r}, t) = V \langle \delta n_s(\mathbf{r}, t) \delta n_s(\mathbf{0}, 0) \rangle = V \langle \delta(\mathbf{r} - \mathbf{R}_1(t)) \delta(\mathbf{0} - R_1(0)) \rangle. \quad (1.13)$$

In inelastic spectroscopy measurement the experimental observables are the time and space Fourier transform of $G(\mathbf{r}, t)$, $C(\mathbf{r}, t)$ and $P(\mathbf{r}, t)$, the dynamic structure factors:

$$S^{nn}(\mathbf{Q}, \omega) = \int_V d\mathbf{r} \int_{-\infty}^{\infty} dt G(\mathbf{r}, t) e^{i(\mathbf{Q}\cdot\mathbf{r}-\omega t)}, \quad (1.14)$$

$$S^{cc}(\mathbf{Q}, \omega) = \int_V d\mathbf{r} \int_{-\infty}^{\infty} dt C(\mathbf{r}, t) e^{i(\mathbf{Q}\cdot\mathbf{r}-\omega t)}, \quad (1.15)$$

$$S^{nc}(\mathbf{Q}, \omega) = \int_V d\mathbf{r} \int_{-\infty}^{\infty} dt P(\mathbf{r}, t) e^{i(\mathbf{Q}\cdot\mathbf{r}-\omega t)}, \quad (1.16)$$

and the time-space Fourier transform of $G_s(\mathbf{r}, t)$, the self dynamic structure factor:

$$S_i(\mathbf{Q}, \omega) = \int_V d\mathbf{r} \int_{-\infty}^{\infty} dt G_s(\mathbf{r}, t) e^{i(\mathbf{Q}\cdot\mathbf{r}-\omega t)}, \quad (1.17)$$

where the momentum, \mathbf{Q} , and the angular frequency, ω , are the Fourier conjugates of \mathbf{r} and t , respectively. The concentration-concentration dynamic structure factor is defined as:

$$S^{cc}(\mathbf{Q}, \omega) = \int_V d\mathbf{r} \int_{-\infty}^{\infty} dt C(\mathbf{r}, t) e^{i(\mathbf{Q}\cdot\mathbf{r}-\omega t)}, \quad (1.18)$$

The partial dynamic structure factors, $S^{\alpha\beta}(Q, \omega)$ ($\alpha, \beta = 1, 2$) can be also defined:

$$S^{\alpha\beta}(\mathbf{Q}, \omega) = \frac{1}{(x_\alpha x_\beta)^{1/2}} \int_V d\mathbf{r} \int_{-\infty}^{\infty} dt \langle \delta n_\alpha \delta n_\beta \rangle e^{i(\mathbf{Q}\cdot\mathbf{r}-\omega t)} \quad (1.19)$$

When the cross term $S^{\alpha\beta}$ (with $\alpha \neq \beta$) is equal to zero, the dynamical variables δn_1 and δn_2 . This occurs in the high Q limit where the scattering is entirely incoherent. Besides $S^{cc}(Q, \omega)$ and $S^{nn}(Q, \omega)$ the cross partial BT dynamic structure factor, S^{nc} can be defined. From 1.8 follows that the partial BT dynamic structure factors are linear combinations of the FZ ones. These relations are most compactly written if one defines the matrix $\tilde{\mathbf{S}}(k, \omega)$ of modified BT partial dynamic structure factors and the matrix $\mathbf{S}(k, \omega)$ of FZ partial dynamic structure factors, respectively:

$$\mathbf{S} = \begin{pmatrix} S^{11} & S^{12} \\ S^{21} & S^{22} \end{pmatrix}; \quad (1.20)$$

$$\tilde{\mathbf{S}} = \begin{pmatrix} S^{nn} & \frac{S^{nc}}{(x_1 x_2)^{1/2}} \\ \frac{S^{cn}}{(x_1 x_2)^{1/2}} & \frac{S^{cc}}{(x_1 x_2)} \end{pmatrix}. \quad (1.21)$$

It is

$$\tilde{\mathbf{S}}(k, \omega) = \mathbf{X} \mathbf{S}(k, \omega) \mathbf{X}, \quad (1.22)$$

where the basis changing matrix, defined in 1.8 is

$$\mathbf{X}^{-1} = \mathbf{X} = \begin{pmatrix} x_1^{1/2} & x_2^{1/2} \\ x_2^{1/2} & -x_1^{1/2} \end{pmatrix}. \quad (1.23)$$

In the low- Q limit one may expect that δn and δc are independent variables, as in the case of ionic crystals. Therefore in the BT representation $S^{nc}(Q, \omega)$ vanish and the description of the dynamics is greatly simplified.

The spatial Fourier transform of $G(\mathbf{r}, t)$, $C(\mathbf{r}, t)$, $P(\mathbf{r}, t)$ and $G_s(\mathbf{r}, t)$, the intermediate scattering functions, are convenient quantities in actual calculation and general discussion. They are defined as:

$$F^{nn}(\mathbf{Q}, t) = \int_V d\mathbf{r} G(\mathbf{r}, t) e^{i\mathbf{Q}\cdot\mathbf{r}}, \quad (1.24)$$

$$F^{cc}(\mathbf{Q}, t) = \int_V d\mathbf{r} C(\mathbf{r}, t) e^{i\mathbf{Q}\cdot\mathbf{r}}, \quad (1.25)$$

$$F^{nc}(\mathbf{Q}, t) = \int_V d\mathbf{r} P(\mathbf{r}, t) e^{i\mathbf{Q}\cdot\mathbf{r}}, \quad (1.26)$$

$$F_s(\mathbf{Q}, \omega) = \int_V d\mathbf{r} G_s(\mathbf{r}, t) e^{i\mathbf{Q}\cdot\mathbf{r}}, \quad (1.27)$$

Exploiting the continuity equation and straightforward algebra the longitudinal current correlation function, $J_L(\mathbf{Q}, \omega)$, i.e. the time and space Fourier transform of $J_L(\mathbf{r}, t)$, can be related to $S^{nn}(\mathbf{Q}, \omega)$:

$$J_L(\mathbf{Q}, \omega) = \frac{\omega^2}{Q^2} S(\mathbf{Q}, \omega). \quad (1.28)$$

By virtue of the isotropy of the system analyzed the direction of \mathbf{Q} is irrelevant and can be neglected. A remark on a general property of $C_{BA}(Q, \omega)$ is worth. In

quantum mechanics the dynamical variables evaluated at different times do not commute. The order in which they appear in the thermal average is significant. $C_{BA}(Q, \omega)$ satisfies the so-called detailed balance condition:

$$C_{BA}(Q, \omega) = e^{\hbar\omega/k_B T} C_{AB}(-Q, -\omega), \quad (1.29)$$

where k_B is the Boltzmann constant. If $C_{BA}(Q, \omega)$ refers to a spectral distribution, 1.29 implies that it is not symmetrical in ω . The energy gain side (Stokes) is higher than the energy loss one (Anti-Stokes).

In order to interpret experimental data, a general expression for $S_i(Q, \omega)$, $S^{nn}(Q, \omega)$, $S^{cc}(Q, \omega)$, $S^{nc}(Q, \omega)$, or alternatively $S^{\alpha\beta}$ is needed. A N -body dynamical problem has, therefore, to be solved. Except the case of an ideal crystal or an ideal gas, the formal solution of this N -body dynamical problem is in practise impossible. Nevertheless, as shown in the following, depending on the (Q, ω) region one is interested to, they exist different approach to mendelize the dynamic structure factors.

1.1.1 Static correlation functions

Conversely to $C_{BA}(Q, t)$, the calculation of the equal time or static correlation function, $C_{BA}(Q, 0)$ doesn't require a solution of the N -body dynamical problem. Because the thermal average is defined with respect to a time-independent ensemble $C_{BA}(Q, 0)$ is an equilibrium property of the system. The basic information it carries on are the equilibrium distribution of particle positions and the intermolecular potential function with its derivatives.

In the case of one-component fluid, for $nn \equiv F(Q, t)$ the correlation functions $F(Q, t)$, $F_s(Q, t)$ and $J_L(Q, t)$ it is found:

$$F(Q, 0) = 1 + n \int d\mathbf{r} e^{i\mathbf{Q}\cdot\mathbf{r}} [g(\mathbf{r}) - 1] \equiv S(Q), \quad (1.30)$$

$$F_s(Q, 0) = 1, \quad (1.31)$$

$$J_L(Q, 0) = v_0^2, \quad (1.32)$$

where $n = N/V$, v_0 is the single particle averaged speed: $\langle \mathbf{v}_1(0) \cdot \mathbf{v}_1(0) \rangle = 3v_0^2 = 3k_B T/M$ and $g(r)$ is the equilibrium pair distribution function:

$$g(r) = \frac{1}{n^2} \sum_{j \neq l}^{1,N} \langle \delta(\mathbf{r} - \mathbf{R}_j) \delta(\mathbf{R}_l) \rangle. \quad (1.33)$$

The quantity $S(Q)$ is called static structure factor, which, in fluids, shows a maximum at Q_M . It is related to the corresponding maximum of the pair correlation function ($Q_M \sim 2\pi/r_M$), being r_M of about the average intermolecular distance. By the definition of $F(Q, t)$ and $S(Q)$ the following relation is readily found:

$$S(Q) = F(Q, 0) = \left[\int_{-\infty}^{\infty} e^{i\omega t} S(Q, \omega) d\omega \right]_{t=0} = \int_{-\infty}^{\infty} S(Q, \omega) d\omega. \quad (1.34)$$

For a binary-component system they remain defined the static correlation functions:

$$F^{\alpha\beta}(Q, 0) = \delta_{\alpha\beta} + n\sqrt{x_\alpha x_\beta} \int d\mathbf{r} e^{i\mathbf{Q}\cdot\mathbf{r}} [g_{\alpha\beta}(\mathbf{r}) - 1] \equiv S^{\alpha\beta}(Q) \quad \alpha \beta = 1, 2, \quad (1.35)$$

where x_α and x_β are the species concentration. Since $g_{12} = g_{21}$, it follows that $S_{12} = S_{21}$. As mentioned in the previous section, in $Q \rightarrow \infty$ limit, $S^{\alpha\beta}(Q) \rightarrow \delta_{\alpha\beta}$ ($S(Q) \rightarrow 1$ for a simple liquid) indicating the vanishing of correlation at very short distances. In the $Q \rightarrow 0$ limit the static structure factors are related to macroscopic transport coefficients. For a monoatomic fluid it is found:

$$S(Q \rightarrow 0) = \frac{n\chi_T}{k_B T}, \quad (1.36)$$

where χ_T is the isothermal compressibility. In the case of a binary component system, the low Q limit of the dynamic structure factors are more directly linked

to the macroscopic properties if the Bhatia-Thornton representation is used:

$$\begin{aligned}
 S^{nn}(Q \rightarrow 0) &= nk_B T \chi_T + \Delta^2 k_B T \left[\left(\frac{\partial^2 g}{\partial x_1^2} \right)_{T,P} \right]^{-1}, \\
 S^{nc}(Q \rightarrow 0) &= S^{cn}(Q \rightarrow 0) = -x_1 x_2 \Delta k_B T \left[\left(\frac{\partial^2 g}{\partial x_1^2} \right)_{T,P} \right]^{-1}, \\
 S^{cc}(Q \rightarrow 0) &= (x_1 x_2)^{1/2} k_B T \left[\left(\frac{\partial^2 g}{\partial x_1^2} \right)_{T,P} \right]^{-1},
 \end{aligned} \tag{1.37}$$

where g is the Gibbs free density energy and Δ is the dilatation factor: $\Delta = \frac{1}{n} \left(\frac{\partial n}{\partial x_1} \right)_{T,P,n}$.

1.1.2 Frequency sum rules

Given a correlation function of a dynamical variable, the corresponding static correlation function specifies its initial value. Time derivative correlation functions are, themselves, correlation functions, and their $t = 0$ values are static correlation functions. These are called frequency sum rules, and can be exploited to describe the short time behavior of time correlation function through a Fourier series expansion. More specifically, in the case of density fluctuation for monoatomic fluids, one has:

$$F(Q, t) = \frac{1}{2\pi} \int_{-\infty}^{\infty} dt S(Q, \omega) e^{i\omega t} = \tag{1.38}$$

$$= \langle \omega^0(Q) \rangle - \frac{t^2}{2} \langle \omega^2(Q) \rangle + \frac{t^4}{4!} \langle \omega^4(Q) \rangle - \dots, \tag{1.39}$$

where

$$\langle \omega^n \rangle = \frac{1}{2\pi} \int_{-\infty}^{\infty} d\omega \omega^n S(Q, \omega), \tag{1.40}$$

with $S(Q, \omega) \equiv S^{mn}(Q, \omega)$. All the odd moments vanish because $S(Q, \omega)$ is an even function in frequency. The first coefficients for density fluctuations are [4]:

$$\begin{aligned}\langle \omega^0(Q) \rangle &= \int_{-\infty}^{\infty} d\omega S(Q, \omega) = S(Q) \\ \langle \omega^2(Q) \rangle &= \int_{-\infty}^{\infty} d\omega \omega^2 S(Q, \omega) = \frac{Q^2 k_B T}{M} \\ \langle \omega^4(Q) \rangle &= \int_{-\infty}^{\infty} d\omega \omega^4 S(Q, \omega) = \frac{Q^4 k_B T}{M} \left(3k_B T + n \int d\mathbf{r} g(\mathbf{r}) \frac{\partial^2 \varphi}{\partial z^2} \left(\frac{1 - \cos(\mathbf{Q} \cdot \mathbf{r})}{Q^2} \right) \right),\end{aligned}\tag{1.41}$$

where $\varphi(\mathbf{r})$ is the pair interaction potential and z denotes the direction of \mathbf{Q} . In the case of binary mixtures

$$F^{\alpha, \beta}(Q, t) = \frac{1}{2\pi} \int_{-\infty}^{\infty} dt S^{\alpha, \beta}(Q, \omega) e^{i\omega t} = \tag{1.42}$$

$$= \langle \omega^0(Q) \rangle^{\alpha, \beta} - \frac{t^2}{2} \langle \omega^2(Q) \rangle^{\alpha, \beta} + \frac{t^4}{4!} \langle \omega^4(Q) \rangle^{\alpha, \beta} - \dots \tag{1.43}$$

The spectral momenta are [35]:

$$\begin{aligned}\langle \omega^0(Q) \rangle^{\alpha\beta} &= \int_{-\infty}^{\infty} d\omega S^{\alpha\beta}(Q, \omega) = S^{\alpha\beta}(Q) \\ \langle \omega^2(Q) \rangle^{\alpha\beta} &= \int_{-\infty}^{\infty} d\omega \omega^2 S^{\alpha\beta}(Q, \omega) = \delta_{\alpha\beta} \frac{Q^2 k_B T}{M_\alpha} \\ \langle \omega^4(Q) \rangle^{\alpha\beta} &= \int_{-\infty}^{\infty} d\omega \omega^4 S^{\alpha\beta}(Q, \omega) = \delta_{\alpha\beta} Q^2 \frac{k_B T}{M_\alpha M_\beta} \cdot \\ &\quad \cdot \left(3Q^2 k_B T + \sum_{i=\alpha, \beta} n_i \int d\mathbf{r} g_{\alpha\beta}(\mathbf{r}) \frac{\partial^2 \varphi_{\alpha\beta}}{\partial z^2} \right) + \\ &\quad - \sqrt{n_\alpha n_\beta} Q^2 \frac{k_B T}{M_\alpha M_\beta} \int d\mathbf{r} g_{\alpha\beta}(\mathbf{r}) \cos(\mathbf{Q} \cdot \mathbf{r}) \frac{\partial^2 \varphi_{\alpha\beta}}{\partial z^2},\end{aligned}\tag{1.44}$$

where $g_{\alpha\beta}$ are the pair correlation functions, $\varphi_{\alpha\beta}(\mathbf{r})$ are the pair interaction potential, $n_{\alpha(\beta)}$ is the number density of particles of specie α .

The calculation of the coefficients $\langle \omega^n \rangle$ for $n > 4$ are very complicated and unusable in practice.

1.2 Classical Hydrodynamics

An exact expression for $S(Q, \omega)$ can be obtained in the framework of classical hydrodynamics, i.e. in the long-time (low ω) and long-wavelength (low Q) limit where the fluid can be regarded as a continuous medium. Hydrodynamic equations are appropriate to describe the system as far as dynamics are probed in a Q -range shorter as compared to the inverse velocity correlation length, λ^{-1} , and in a ω -range smaller as compared to the microscopic relaxation frequencies of the system. The velocity correlation length is the distance in the fluid over which a given particle can travel before collisions greatly change its velocity. It can be, therefore, identified with the mean free path. In a one component fluid, because all the particles in the system are equivalent by virtue of its isotropy, a single length scale remains defined. In a binary mixtures the dependence of the mean free path from the specie particles must be considered: three different length scale, λ_{12} , i.e. the distances over which a particle of kind 1 can travel without collisions with particle of kind 2, are introduced. The condition of validity for hydrodynamic equations is: $Q < \lambda_i^{-1}$, with $i = 1, 2$. The second condition concerns the relaxation frequencies characterizing the return to equilibrium in the fluid. For a general system three frequencies can be defined [36]: 1) ω_M , the Maxwellization frequency or stress relaxation frequency, i.e. the frequency at which the viscosity relaxes; 2) ω_u , the relaxation frequency for the relative velocity of two different particles in the fluid; 3) ω_Δ , the relaxation frequency for temperature equilibration between the two sub-system of species 1 and 2 in the fluid. Whereas in a one-component system ω_u and ω_Δ coincide with ω_M (that can be, indeed, assumed to be the relaxation frequency for the fluid) in a binary mixture they can be widely different, depending on the mixture characteristics. In such a system, ω_u and ω_Δ are identified with the relaxation frequency of relative velocity and temperature of two specie components, respectively. The return to equilibrium in a binary mixture is then characterized

by more than one time-scale. The condition of validity for the hydrodynamic equation is that ω is lower than the lowest between the frequencies ω_M , ω_u and ω_Δ .

1.2.1 Hydrodynamics of single component fluids

The classical hydrodynamic description of a one-component, isotropic, non-relativistic medium is based on the assumption that the macroscopic state of a single component fluid is given in terms of momentum, mass and energy conservation laws [37]. Such laws can be written as:

$$\frac{\partial}{\partial t}\rho(\mathbf{r}, t) + \nabla \cdot \mathbf{J}(\mathbf{r}, t) = 0 \quad (1.45)$$

$$\frac{\partial}{\partial t}\mathbf{J}(\mathbf{r}, t) + \nabla \cdot \tau(\mathbf{r}, t) = 0 \quad (1.46)$$

$$\frac{\partial}{\partial t}e(\mathbf{r}, t) + \nabla \cdot \mathbf{J}^e(\mathbf{r}, t) = 0, \quad (1.47)$$

where $\rho(\mathbf{r}, t)$ is the mass density, $\mathbf{J}(\mathbf{r}, t)$ is the momentum, e is the energy, and $\mathbf{J}(\mathbf{r}, t)$, $\tau(\mathbf{r}, t)$, $\mathbf{J}^e(\mathbf{r}, t)$ are the relative fluxes, respectively. To solve the system it's needed to introduce constitutive equations:

$$\mathbf{J} = \rho\mathbf{v} \quad (1.48)$$

$$\tau_{ij} = \rho v_i v_j - \sigma_{ij} \quad (1.49)$$

$$\mathbf{J}^e = e\mathbf{v} - \mathbf{Q}. \quad (1.50)$$

The subscript i indicates the i^{th} Cartesian component, $\mathbf{v}(\mathbf{r}, t)$ is the velocity of a particle in the fluid, σ_{ij} is the stress tensor and \mathbf{Q} is the energy flux due to heat conduction. The last two quantities are given by the Newtonian stress tensor and the Fourier's law, respectively:

$$\sigma_{ij} = -P\delta_{ij} + \eta_s \left(\nabla_i v_j + \nabla_j v_i - \frac{2}{3} \nabla \cdot \mathbf{v} \delta_{ij} \right) + \eta_B \nabla \cdot \mathbf{v} \delta_{ij} \quad (1.51)$$

$$Q_i = -\lambda \nabla_i T, \quad (1.52)$$

with η_s and η_B the shear and bulk viscosities, respectively, and λ the thermal conductivity coefficient. If, as it is the case in the hydrodynamic limit, the relaxation process are slower than the molecular motions, the system can be considered in local thermodynamic equilibrium state and the number of thermodynamic variables can be reduced. Exploiting the Equation of State (EoS), one of the three thermodynamic variables, e, ρ and P , can be expressed as a function of the other two. Moreover, since small fluctuations, δX , of variables $X = X_0 + \delta X$ around their equilibrium values are considered, one can use the following approximations: $\rho = \rho_0 + \delta\rho$, $\mathbf{J} = \delta\mathbf{J}$, $T = T_0 + \delta T$, and retaining only terms at first order in the variations. The Linearized Hydrodynamic Equations (*LHE*) are then obtained in the usual way by Fourier-Laplace transform:

$$\begin{aligned}
 z\delta\rho(\mathbf{Q}, z) + i\mathbf{Q} \cdot \mathbf{J}(\mathbf{Q}, z) &= \delta\rho(\mathbf{Q}, 0) \\
 i\frac{c_s^2}{\gamma}\mathbf{Q}\delta\rho(\mathbf{Q}, z) + (z + \rho_0\eta_L Q^2)\mathbf{J}(\mathbf{Q}, z) + i\alpha\rho_0\frac{c_s^2}{\gamma}\delta T(\mathbf{Q}, z) &= \mathbf{J}(\mathbf{Q}, 0) \\
 i\frac{\gamma-1}{\alpha}\mathbf{Q} \cdot \mathbf{J}(\mathbf{Q}, z) + (z + \gamma D_T Q^2)\rho_0\delta T(\mathbf{Q}, z) &= \rho_0\delta T(\mathbf{Q}, 0), \tag{1.53}
 \end{aligned}$$

where c_s is the adiabatic sound velocity ($c_s^2 = (\partial P/\partial\rho)_S$, with S the entropy), $\gamma = c_P/c_V$ the specific heat ratio, c_P and c_V the specific heat at constant pressure and volume, respectively, $\alpha = -\rho^{-1}(\partial\rho/\partial T)_P$ the thermal expansion coefficient, $\eta_L = (\frac{4}{3}\eta_s + \eta_B)/\rho_0$ the longitudinal viscosity, $D_T = \frac{\lambda}{\rho_0 c_P}$ the thermal diffusion coefficient. The set of five equations 1.53 in five variables can be cast into a 5×5 matrix and solved with to respect $\delta\rho(\mathbf{Q}, z)$:

$$\delta\rho(\mathbf{Q}, z) = \frac{\det \begin{pmatrix} \delta\rho(\mathbf{Q}, 0) & i\mathbf{Q} & 0 \\ \mathbf{J}(\mathbf{Q}, 0) & (z + \eta_L Q^2) & i\alpha\rho_0\frac{c_s^2}{\gamma} \\ \rho_0\delta T(\mathbf{Q}, 0) & i\frac{\gamma-1}{\alpha}\mathbf{Q} & (z + \gamma D_T Q^2)\rho_0 \end{pmatrix}}{\det \begin{pmatrix} z & i\mathbf{Q} & 0 \\ i\frac{c_s^2}{\gamma}\mathbf{Q} & (z + \eta_L Q^2) & i\alpha\rho_0\frac{c_s^2}{\gamma} \\ 0 & i\frac{\gamma-1}{\alpha}\mathbf{Q} & (z + \gamma D_T Q^2)\rho_0 \end{pmatrix}}. \tag{1.54}$$

From 1.54 a formal expression for mass-density fluctuations in the Fourier-Laplace space, $\langle \delta\rho(\mathbf{Q}, 0)^* \delta\rho(\mathbf{Q}, z) \rangle$, can be deduced. Through the definition 1.14, passing from Laplace to Fourier space, the expression for $S(Q, \omega)$ is then obtained.

The denominator of 1.54 can be expressed as $\prod_{j=1,5}(z - z_j)$, where z_j are the eigenvalues of the hydrodynamic modes. Since z_j are independent from the base, with the aim to gain some insight into the physics of the system, it is convenient to express eqs. 1.53 as a function of pressure, P , entropy per unit molecule $s = S/N$, longitudinal current $w = \nabla \cdot \mathbf{J}$, and transverse current $\mu_{1,2} = (\nabla \times \mathbf{J})_{1,2}$. The following set of equations is obtained:

$$\left[\frac{\partial}{\partial t} - (\gamma - 1)D_T \nabla^2 \right] \delta P(r, t) + c_s^2 w(r, t) - \rho_0 \alpha^{-1} (\gamma - 1) D_T \nabla^2 \delta s(r, t) = 0 \quad (1.55)$$

$$\left[\frac{\partial}{\partial t} - \nu_L \right] w(r, t) + \nabla^2 \delta P(r, t) = 0 \quad (1.56)$$

$$\left(\frac{\partial}{\partial t} - D_T \nabla^2 \right) \delta s(r, t) - \alpha \rho_0^{-1} D_T \nabla^2 \delta P(r, t) = 0 \quad (1.57)$$

$$\left(\frac{\partial}{\partial t} - \nu_s \nabla^2 \right) \mu_1(r, t) = 0 \quad (1.58)$$

$$\left(\frac{\partial}{\partial t} - \nu_s \nabla^2 \right) \mu_2(r, t) = 0, \quad (1.59)$$

where $\nu_s = \eta_s \rho^{-1}$ and $\nu_B = (\eta_s + \frac{2}{3}\eta_d)\rho^{-1}$ are called kinematic shear and bulk viscosity, respectively and $\nu_L = \frac{4}{3}\nu_s + \nu_B$ then denote the longitudinal kinematic viscosity. From a double Laplace-Fourier transform of eqs. 1.55-1.59, the matrix equivalent to the denominator in 1.54 is given:

$$\begin{pmatrix} [z + (\gamma - 1)D_T Q^2] & c_s^2 & \rho_0 \alpha^{-1} (\gamma - 1) D_T Q^2 & 0 & 0 \\ -Q^2 & [z + (\nu_L)] & 0 & 0 & 0 \\ \rho_0^{-1} \alpha D_T Q^2 & 0 & [z + D_T Q^2] & 0 & 0 \\ 0 & 0 & 0 & [z + \nu_s Q^2] & 0 \\ 0 & 0 & 0 & 0 & [z + \nu_s Q^2] \end{pmatrix} \quad (1.60)$$

The hydrodynamic modes are obtained as the roots of the determinant of the

1. Collective modes and fluid dynamics

matrix 1.60. The 2×2 minor on the bottom right yields two degenerate solutions:

$$z_s = -\nu_s Q^2. \quad (1.61)$$

They correspond to non propagating shear (transverse) modes. The non-propagating nature of transverse mode is a very well known macroscopic property of viscous fluids. Moreover since transverse current is uncoupled from density fluctuations, it is not possible to obtain shear modes in $S(Q, \omega)$ as far as the hydrodynamic limit is fulfilled. The eigenvalues of the upper left minor are the solutions of the following 3th order dispersion equation:

$$z^3 + z^2(\gamma D_T Q^2 + \nu_L Q^2) + z(c^2 Q^2 + \gamma D_T \nu_L Q^4) + D_T c^2 Q^4 = 0. \quad (1.62)$$

In the low Q limit, at order Q^2 , the roots are:

$$z_0 = -D_T Q^2 \quad (1.63)$$

$$z_{\pm} = \pm i c_s Q - \Gamma Q^2, \quad (1.64)$$

where

$$\Gamma = \frac{1}{2}[\nu_L + (\gamma - 1)D_T]. \quad (1.65)$$

This result points out the existence of three propagating modes in the hydrodynamic regime. The real root correspond to thermal diffusivity mode resulting from the entropy fluctuations at constant pressure. The complex roots account for the propagation of compressional waves, also referred to as longitudinal acoustic (LA) modes. They propagate with the adiabatic sound velocity, c_s , and have a lifetime (damping) $(\Gamma Q^2)^{-1}$. The coupling between thermal and LA modes is given by the non diagonal terms of matrix 1.60, and it is rather weak for ordinary fluids.

Assuming that $\langle \delta\rho^*(Q, 0)\mathbf{J}(Q, 0) \rangle = \langle \delta\rho^*(Q, 0)\delta T(Q, 0) \rangle = 0$, the correlation function for density fluctuations is:

$$\langle \delta\rho(Q, 0)^* \delta\rho(Q, z) \rangle = \frac{(z + \nu_L Q^2)(z + \gamma D_T Q^2) + (1 - \gamma^{-1})c_s^2 Q^2}{(z - z_0)(z - z_+)(z - z_-)} \langle \delta\rho^*(Q, 0)\delta\rho(Q, 0) \rangle, \quad (1.66)$$

being $\langle \delta\rho^*(Q, 0)\delta\rho(Q, 0) \rangle = S(Q)$. Passing from Laplace to Fourier space¹ and neglecting terms of order Q^4 , after some straightforward algebra, the so-called Rayleigh-Brillouin spectrum is obtained:

$$\begin{aligned} \frac{S(Q, \omega)}{S(Q)} &= \frac{\gamma-1}{\gamma} \frac{2D_T Q^2}{\omega^2 + (D_T Q^2)} + \frac{1}{\gamma} \left[\frac{\Gamma Q^2}{(\omega + c_s Q)^2 + (\Gamma Q^2)^2} + \frac{\Gamma Q^2}{(\omega - c_s Q)^2 + (\Gamma Q^2)^2} \right] + \\ &+ \frac{Q}{\gamma c_s} [\Gamma + (\gamma - 1)D_T] \left[\frac{(\omega + c_s Q)}{(\omega + c_s Q)^2 + (\Gamma Q^2)^2} - \frac{(\omega - c_s Q)}{(\omega - c_s Q)^2 + (\Gamma Q^2)^2} \right]. \end{aligned} \quad (1.68)$$

It is the sum of three Lorentian functions: 1) one centered at $\omega = 0$, whose width is given by $D_T Q^2$, usually called the Rayleigh peak, is related to the thermal diffusive mode; 2) other two Lorentians, symmetrically centered at $\pm c_s Q$ and having a width given by ΓQ^2 , usually referred to as the Stokes and anti-Stokes component of the Brillouin doublet, represent the LA modes. The asymmetric term in 1.68 ensures the fulfilment of the 1th sum rule for a classical fluid.

Despite that the Rayleigh-Brillouin spectrum describes the measured spectral density of simple fluids in their hydrodynamic limit very well, the spectrum represented in eq. 1.68 does not satisfy the 2nd sum rule, since $\int \omega^2 S(Q, \omega) d\omega = \infty$. An alternative description consists of replacing the two symmetric side Lorentians and the asymmetric term by a damped harmonic oscillator (DHO) function:

$$\frac{S^{DHO}(Q, \omega)}{S(Q)} = \frac{1}{\pi} \frac{(C_s Q)^2 \Gamma}{[\omega^2 - (C_s Q)^2]^2 + \omega^2 \Gamma^2} \quad (1.69)$$

This function is the space and time Fourier transform of the solution of the cardinal equation of a damped harmonic oscillator with characteristic frequency $\Omega_0 = C_s Q$ and damping coefficient $\Gamma_0 = \Gamma$. Equation 1.69 can be derived directly from eq. 1.54, if the terms $\propto Q^4$ are not neglected. The DHO expression preserves the 2nd-order sum rules.

¹The dynamic structure factor is obtained from $\tilde{F}(Q, z) = \langle \delta\rho(Q, 0)^* \delta\rho(Q, z) \rangle$ through the relation:

$$S(Q, \omega) = \frac{1}{\pi} \Re(\tilde{F}(Q, z = -i\omega)) \quad (1.67)$$

1.2.2 Hydrodynamics of binary mixtures

In the following the hydrodynamic of a neutral (1.2.2.1) and ionic (1.2.2.3) binary mixtures is briefly reported. To specify the thermodynamic state of a binary system three variables are needed (see sec.1.1). To obtain the hydrodynamic equations for such systems, the mass-concentration fluctuations, δc^m , related to concentration fluctuations δc defined in 1.1, has to be introduced:

$$\delta c^m = \rho_0^{-1}[(1 - c)\delta\rho_1(\mathbf{r}, t) - c]\delta\rho_2(\mathbf{r}, t), \quad (1.70)$$

with

$$\rho = \rho_1(\mathbf{r}, t) + \rho_2(\mathbf{r}, t) = M_1 n_1(\mathbf{r}, t) + M_2 n_2(\mathbf{r}, t) \quad (1.71)$$

$$c \equiv c_1 = \frac{M_1 n_1(\mathbf{r}, t)}{M_1 n_1(\mathbf{r}, t) + M_2 n_2(\mathbf{r}, t)} = \frac{1}{1 + R(x_1^{-1} - 1)}, \quad (1.72)$$

where $R = M_2/M_1$ the mass ratio between the specie components. The conservation laws 1.45-1.47 have to be extended to concentration fluctuations:

$$\frac{\partial}{\partial t}\rho(\mathbf{r}, t) + \nabla \cdot \mathbf{J}(\mathbf{r}, t) = 0 \quad (1.73)$$

$$\frac{\partial}{\partial t}\mathbf{J}(\mathbf{r}, t) + \nabla \cdot \tau(\mathbf{r}, t) = 0 \quad (1.74)$$

$$\frac{\partial}{\partial t}e(\mathbf{r}, t) + \nabla \cdot \mathbf{J}^e(\mathbf{r}, t) = 0 \quad (1.75)$$

$$\frac{\partial}{\partial t}c^m(\mathbf{r}, t) + \nabla \cdot \mathbf{J}^c(\mathbf{r}, t) = 0, \quad (1.76)$$

where J^c is the concentration flux. The constitutive equations for \mathbf{J} and τ are unchanged to respect a one-component fluid (and then equal for neutral or ionic systems), once the barycentric velocity:

$$\mathbf{v} = c \mathbf{v}_1 + (1 - c) \mathbf{v}_2 \quad (1.77)$$

is used in 1.48. Peculiar constitutive equation for J^e and J^c , conversely, have to be given. The case of neutral and ionic system will be considered separately in the following.

1.2.2.1 Neutral systems

The diffusion flux for a neutral binary mixture is:

$$\mathbf{J}^c = \rho_0 D_{12} \left(\nabla c^m + \frac{k_T}{T_0} \nabla T + \frac{k_P}{P_0} \nabla P \right), \quad (1.78)$$

with D_{12} the interdiffusion coefficient, k_T and k_P are the thermal and pressure diffusion ratio, respectively. The latter is defined as:

$$k_P = P_0 \left(\frac{\partial \mu}{\partial P} \right)_{T,c} \left[\left(\frac{\partial \mu}{\partial c} \right)_{T,P} \right]^{-1}, \quad (1.79)$$

where μ is the chemical potential per unit mass of the two component:

$$\mu = \frac{\mu_1}{M_1} - \frac{\mu_2}{M_2}, \quad (1.80)$$

it is related to the Gibbs free energy per unit mass through the thermodynamic relationship:

$$dg = \rho^{-1} dP - s dT + \mu dc. \quad (1.81)$$

The related term in 1.78 takes into account of the mass-concentration flux induced by the thermal gradient, according to the so-called Soret effect, and by the pressure gradient.

It is convenient to express equation 1.75 in terms of the entropy per unit mass, s :

$$\rho_0 T_0 \frac{\partial}{\partial t} s(\mathbf{r}, t) + \nabla \cdot \mathbf{J}^q(\mathbf{r}, t) = 0. \quad (1.82)$$

The heat flux $J^q(\mathbf{r}, t)$ is given by:

$$\mathbf{J}^q(\mathbf{r}, t) = \lambda \nabla T(\mathbf{r}, t) - A \mathbf{J}^c(\mathbf{r}, t). \quad (1.83)$$

The first term in 1.83 is equivalent to 1.52, the second one takes into account of the interdiffusion contribution to heat transfer according to the Dufour effect. The coefficient A is given by:

$$A = k_T \left(\frac{\partial \mu}{\partial c} \right)_{P,T} - T_0 \left(\frac{\partial \mu}{\partial T} \right)_{P,c}. \quad (1.84)$$

1. Collective modes and fluid dynamics

The conservation equations for the variables ρ , J , c^m and s , together with the constitutive equations, define a 6×6 hydrodynamic matrix. These equations are a closed set and can be, therefore, solved. As in the case of one-component fluid, however, it's convenient choose a more appropriate set of dynamical variables to solve the problem. By imposing the condition of statistical independence of the fluctuations of the thermodynamical variables, a suitable set of thermodynamical variables, fulfilling such requirement, is (P, c^m, u, ϕ) , where $u = \nabla \cdot \mathbf{v}$ is the divergence of the baricentric velocity (proportional to $J_L(Q, \omega)$), and

$$\phi = T - \frac{T_0 \alpha}{c_P \rho_0} P. \quad (1.85)$$

The transverse components of the longitudinal current that, as for the one-component fluid, are decoupled from the fluctuations of all the other variables, are here neglected. In this basis set the 4×4 hydrodynamic matrix is:

$$\begin{pmatrix} z + D_{12}Q^2 & D_{12}PQ^2 & SQ^2 & 0 \\ c_s^2 \rho_0^2 D_{12} ZPQ^2 & z + c_s^2 \rho_0^2 D_{12} ZP^2 Q^2 + c_s^2 \frac{T_0 \alpha^2}{c_P} D_T Q^2 & \rho_0 c_s^2 [\rho_0 SZPQ^2 + \alpha D_T Q^2] & \rho_0 c_s^2 \\ \frac{D_{12} k_T}{c_P} ZQ^2 & \frac{D_{12} k_T}{c_P} ZPQ^2 + \frac{T_0 \alpha}{\rho_0 c_P} D_T Q^2 & z + \frac{S k_T}{c_P} ZQ^2 + D_T Q^2 & 0 \\ 0 & -\frac{Q^2}{\rho_0} & 0 & 0 \end{pmatrix} \quad (1.86)$$

where $P = \frac{k_P}{P} + \frac{k_T \alpha}{\rho_0 c_P}$, $Z = \left(\frac{\partial \mu}{\partial c}\right)_{P,T}$ and $S = \frac{D_{12} k_T}{T_0}$. The 4th order dispersion relation for the neutral binary mixture, therefore, is:

$$(z - z_1)(z - z_2)(z - i c_s Q + \Gamma Q^2)(z + i c_s Q + \Gamma Q^2) = 0. \quad (1.87)$$

The roots are:

$$z_1 = \frac{Q^2}{2}(D_T + D) + \frac{Q^2}{2}[(D_T + D)^2 - 4 D_T D_{12}]^{1/2} \quad (1.88)$$

$$z_2 = \frac{Q^2}{2}(D_T + D) - \frac{Q^2}{2}[(D_T + D)^2 - 4 D_T D_{12}]^{1/2} \quad (1.89)$$

$$z_{\pm} = \pm i c_s Q - \gamma Q^2, \quad (1.90)$$

with

$$\Gamma = \frac{1}{2} \left[\eta_L + D_T(\gamma - 1) + D_{12}\rho_0^2 c_s^2 \left(\frac{\partial \mu}{\partial c^m} \right)_{P,T} B^2 \right], \quad (1.91)$$

being

$$B = D_{12} \left[1 + \frac{k_T^2}{T_0 c_P} \left(\frac{\partial \mu}{\partial c} \right)_{P,T} \right]. \quad (1.92)$$

Two diffusive modes and two propagating modes, with the adiabatic sound speed c_s , exist in the hydrodynamic limit for a neutral binary mixture. It is to observe that, following the Onsager symmetry relations rules, the number of propagating modes should be at most $2m$, where m is the number of dynamical variables odd for time inversion operation and coupled to n even dynamical variables, with $n \geq m$. Consequently, analyzing the given set of dynamical variables, the diffusive nature of the modes z_1 and z_2 is defined by such rules. Following the same steps illustrated for the one-component fluid the dynamical structure factors are obtained. In the following are reported the general expressions for S_{nn} , S_{nx} and S_{xx} ;

$$S_{nn}(Q, \omega) = nk_B T_0 \chi_T \left[\frac{2A_1 X Q^2}{\omega^2 + X^2 Q^4} + \frac{2A_2 Y Q^2}{\omega^2 + Y^2 Q^4} + \frac{\Gamma Q^2}{(\omega + c_s Q)^2 + \Gamma^2 Q^4} + \frac{\Gamma Q^2}{(\omega - c_s Q)^2 + \Gamma^2 Q^4} + A_3 \frac{Q}{c_s} \left(\frac{\omega + c_s Q}{(\omega + c_s Q)^2 + \Gamma^2 Q^4} - \frac{\omega - c_s Q}{(\omega - c_s Q)^2 + \Gamma^2 Q^4} \right) \right] \quad (1.93)$$

$$S_{nx}(Q, \omega) = nk_B T_0 \left[\frac{2A_4 X Q^2}{\omega^2 + X^2 Q^4} + \frac{2A_5 Y Q^4}{\omega^2 + Y^2 Q^4} + A_6 \frac{Q}{c_s} \left(\frac{\omega + c_s Q}{(\omega + c_s Q)^2 + \Gamma^2 Q^4} - \frac{\omega - c_s Q}{(\omega - c_s Q)^2 + \Gamma^2 Q^4} \right) \right] \quad (1.94)$$

$$S_{xx}(Q, \omega) = \frac{nk_B T_0}{Z} \left[\frac{2A_7 X Q^2}{\omega^2 + X^2 Q^4} + \frac{2A_8 Y Q^2}{\omega^2 + Y^2 Q^4} \right]. \quad (1.95)$$

The coefficients $A_1 - A_6$ depend on thermodynamic parameters. The coefficient X and Y are related to both the thermal diffusivity and interdiffusion coefficients:

$$X = \frac{1}{2} [(D_T + D_{12}) + [(D_T + D_{12})^2 - 4D_T D_{12}]^{1/2}], \quad (1.96)$$

$$Y = \frac{1}{2} [(D_T + D_{12}) - [(D_T + D_{12})^2 - 4D_T D_{12}]^{1/2}] \quad (1.97)$$

The dynamic structure factor S_{nn} is the sum of two Lorentzian centered at zero, whose width is given by XQ^2 and YQ^2 respectively and it is then related in a non simply way to D_T and D_{12} . Other two Lorentzians, centered at $\pm c_s Q$ and having a width given by γQ^2 , represent the LA modes. The last two terms take into account of the asymmetric contribution to the Brillouin doublet, in analogy with one-component fluid. The dynamic structure factor S_{xx} is, conversely, described by only two Lorentzians centered in zero and with width XQ^2 and YQ^2 respectively, i.e. propagating modes do not contribute to it. Finally, the dynamic structure factor S_{nx} feels the contribution of the two diffusive mode contributing to the central peak of S_{nn} and S_{xx} and of the asymmetric term also present in $S_{nn}(Q, \omega)$.

1.2.2.2 "Hydrodynamic" description of fast and slow sound modes?

The emergence of the fast and slow sound modes at sufficiently large wavevectors is usually described as a fingerprint of the non-validity of the hydrodynamic equations at such wavevectors. A kinetic nature of such modes is, in fact, evoked. The Onsager relations rules, if applied to the hydrodynamic set of equations reported in subsec. 1.2.2.1, on the other hand, set the existence of at most two propagating modes in the hydrodynamic regime. The limit of validity of hydrodynamics in binary mixtures is set by the conditions previously described: 1) $Q \ll \lambda^{-1}$ and, 2) $\omega \ll \min(\omega_M, \omega_u, \omega_\Delta)$. In disparate mass systems (i.e. mixtures where $R \gg 1$) the condition $\omega_T < \omega_u < \omega_M$ is usually fulfilled. If ω_T is sufficiently small it can happen that the first condition is fulfilled, but the latter not. This implies that macroscopic parameters are Q -independent around the Q -range where classical hydrodynamics ceases to be valid, because condition 2) is violated. Consequently, one may describe to a certain extent the dispersion relation in this regime in terms of macroscopic parameters. This approach has been used by Goldman and Sirovich [7] in the case of gaseous disparate mass binary mixtures probed in

such frequency regime, also called “two temperature regime”. At such frequencies, in fact, the temperatures and momenta characterizing the particle subsystems of the two specie components, i.e. (T_1, T_2) and $(\mathbf{v}_1, \mathbf{v}_2)$, can be different. The starting point of this frame are the coupled Boltzmann equations for the phase-space distributions, $f_{1,2}(\mathbf{q}, \mathbf{p}, t)$. Following a Chapman-Enskog type procedure [9], it is obtained a set of “hydrodynamic-like equations” that attempts to account for the initial deviations from classical hydrodynamics resulting from momentum and temperature relaxations. Specifically, to the classical hydrodynamical set of variables (ρ, \mathbf{J}, s, c) are added the variables diffusion flux, \mathbf{J}^c and temperature separation, $\Delta \equiv T_2 - T_1$. The corresponding continuity equations are:

$$\frac{\partial}{\partial t} \mathbf{J}^c(\mathbf{r}, t) = \omega_u \left[\mathbf{J}^c(\mathbf{r}, t) - \rho_0 D_{12} \left(\nabla c + \frac{k_T}{T_0} \nabla T + \frac{k_P}{P_0} \nabla P \right) \right] \quad (1.98)$$

$$\frac{\partial}{\partial t} \Delta - \frac{1}{c_V \rho_0} \nabla^2 \left(\frac{\lambda_1}{x_1} T_1 - \frac{\lambda_2}{x_2} T_2 \right) + \frac{\gamma - 1}{\rho_0 \alpha} \nabla \cdot \mathbf{J}^c(\mathbf{r}, t) = -\omega_\Delta \Delta, \quad (1.99)$$

where λ_1 and λ_2 are the coefficient of thermal conductivity of specie 1 and 2 in the mixture ². It is to observe that 1.98 reduces to the conventional expression 1.78 if $\omega_u \rightarrow \infty$, i.e. if $\tau_u = 1/\omega_u \rightarrow 0$. The expression 1.78 states that the current \mathbf{J}^c responds instantaneously to the application of gradient in c , T or P , whereas in the two temperature regime, where expression 1.98 holds, the current \mathbf{J}^c responds to gradients only after a relaxation time τ_u has elapsed. Similarly, when $\omega_\Delta \rightarrow \infty$, i.e. $\tau_\Delta = 1/\omega_\Delta \rightarrow 0$, eq. 1.99 simply states that $\Delta = 0$. The dispersion equations following from this modified hydrodynamic equations has been solved numerically for mixtures of Helium and Xenon at standard temperature and pressure [8]. It result that, for suitable values of compositions and above a critical frequency, ω_c ,

²It is usually assumed that λ_2 (with $R \gg 1$) is coincident with the conventional thermal conductivity for the pure specie, whereas λ_1 contains terms related to the cross contributions. For example, within a kinetic treatment where it is supposed that the interaction potential is described by a Maxwell-type intermolecular repulsive force, $\frac{k_{ij}}{r^5}$, it is: $\lambda_1 = \frac{5k_B P_1}{2M_1(2B_{11}\rho_1 + A\rho_2)}$, with P_1 the partial pressure of specie 1. B_{11} and A are collision parameters referred to self collisions and cross collisions, respectively.

the systems can sustain two propagating mode of different phase velocities and similar absorption coefficients. The existence of fast sound mode in Helium and a simultaneous slow sound mode in Xenon emerges also by analyzing the partial dynamic structure factors predicted by two temperature hydrodynamics [38]. A propagating modes with characteristic frequency, ω_1 , is, in fact, observed in S^{HeHe} and a propagating mode with slower characteristic frequency, ω_2 , is present in S^{XeXe} .

A similar approach to that of the “two temperature” hydrodynamic has been proposed also for a generic fluid, taking into account only of the specie components momenta relaxation [13]. The “hydrodynamical-like” variables set is, then, $(\rho, \mathbf{J}, s, c^m, \mathbf{J}^c)$. The continuity equation 1.98 is replaced by:

$$\frac{\partial}{\partial t} \mathbf{J}^c(\mathbf{r}, t) = \xi \left[\mathbf{J}^c(\mathbf{r}, t) + \rho_0 D_{12} \left(\nabla c^m + \frac{k_T}{T_0} \nabla T + \frac{k_P}{P_0} \nabla P \right) \right], \quad (1.100)$$

where ω_u is, then, replaced by the friction coefficient ξ , which is related to D_{12} by:

$$\xi = c(1 - c) \left(\frac{\partial \mu}{\partial c} \right)_{T,P} D_{12}^{-1}. \quad (1.101)$$

In the Chapman-Enskog approach ω_u is estimated to be:

$$\omega_u = \frac{M_1 x_1 + M_2 x_2}{M_1 M_2} \frac{k_B T}{D_{12}}. \quad (1.102)$$

It is to observe that in the case of a nearly ideal mixture, where

$$\left(\frac{\partial \mu}{\partial c} \right)_{T,P} = k_B T \frac{M_2}{M_1 (M_1 x_1 + M_2 x_2)} \frac{1}{c(1 - c)}, \quad (1.103)$$

ξ is related to ω_u by the relation

$$\xi = ((M_1 x_1 + M_2 x_2)/M_2)^2 \omega_u. \quad (1.104)$$

In this case the value of the momentum relaxation frequency is directly linked only to the interdiffusion coefficient. In a real mixture, as posed by 1.101, the momentum relaxation frequency depend also on the parameter $\left(\frac{\partial \mu}{\partial c} \right)_{T,P}$, that should be

positive if the condition of material stability is fulfilled by the mixture. If the system shows a demixing tendency, instead, $(\frac{\partial\mu}{\partial c})_{T,P} \rightarrow 0$. Consequently, $\xi \rightarrow 0$ and the momentum relaxation time becomes larger so 'extending' the towards lower frequency the region of validity of the equation 1.100. The dispersion relation following from eqs. 1.73-1.76 and 1.100 reveals the existence of five modes. Neglecting, to benefit of simplicity, the heat and momentum dissipation as well as the the effect of thermal diffusion, i.e. $D_T = \eta_L = k_T = 0$, the dispersion relation is solved analytically. It is found the existence of two couples of propagating modes that exhibit a linear dispersion in the large- Q limit. Their sound velocities, that in this simplified case can be calculated explicitly [13], are faster and slower than c_s , respectively. Explicitly:

$$c_{fast,slow}^2 = \frac{c_s^2}{2} \left[1 + c(1-c) \frac{(\partial\mu/\partial c)_{T,P}}{c_s^2} \Xi \pm \sqrt{\left(1 + c(1-c) \frac{\mu}{c_s^2} \Xi\right)^2 - 4c(1-c) \frac{\mu}{c_s^2}} \right], \quad (1.105)$$

with

$$\Xi = 1 + \frac{c_s^2}{\mu} \left((k_P + k_T)^2 + \frac{1}{\gamma - 1} k_T^2 \right). \quad (1.106)$$

It is possible, moreover, to give the number of molecules taking part in the fast (slow) sound propagation by calculating the eigenvector associated with the fast (slow) sound mode. This calculation emphasizes that, in such a frame, the lighter and heavier molecules do not oscillate separately but some molecules of different species interacts one to each other.

1.2.2.3 Ionic systems

In a ionic binary mixture δc is replaced by the charge density fluctuation, δq , which is related to partial density fluctuation as follows:

$$\delta q \equiv \rho_0^{-1} e [z_1(1-c)\delta\rho_1 + cz_2\delta\rho_2] = ez\delta c^m, \quad (1.107)$$

where e is the electron charge and $ez_1 = -ez_2 = ez$ is the charge of each component, which values are supposed to be equal. This assumption is valid, for example, in the case of a completely dissociated molten salt. The corresponding conservation equation is:

$$\frac{\partial}{\partial t}q(\mathbf{r}, t) + \nabla \cdot \mathbf{J}^z(\mathbf{r}, t) = 0. \quad (1.108)$$

The conservation equations 1.73 and 1.74 with the respective fluxes are unchanged with respect to neutral mixtures and one-component systems, as previously emphasized. The heat and diffusion flux is given by:

$$\mathbf{J}^q(\mathbf{r}, t) = \lambda \nabla T(\mathbf{r}, t) - A \mathbf{J}^z(\mathbf{r}, t), \quad (1.109)$$

with

$$A = \frac{\alpha}{\sigma}, \quad (1.110)$$

being α the thermoelectric coefficient and σ the electric conductivity. This expression is completely equivalent to the one for a neutral systems, once α/σ is replaced by the appropriate transport coefficient and \mathbf{J}^z is replaced by \mathbf{J}^c . The crucial difference between the charged fluid and the neutral fluid is, instead, the expression for the current \mathbf{J}^z (to be compared with \mathbf{J}^c , see eq. 1.78), i.e.:

$$\mathbf{J}^z = \sigma[\mathbf{E}(\mathbf{r}, t) - \frac{1}{e}\nabla\mu(\mathbf{r}, t)] - \frac{\alpha}{T_0}\nabla T(\mathbf{r}, t), \quad (1.111)$$

where the electrical field, $\mathbf{E}(\mathbf{r}, t)$, is related to the total charge density by Poisson's equation:

$$\nabla \cdot \mathbf{E}(\mathbf{r}, t) = \frac{4\pi}{\epsilon}q(\mathbf{r}, t), \quad (1.112)$$

being ϵ the dielectric constant. Moreover, the variation in the electrochemical potential, μ , can be written as:

$$\delta\mu = \left(\frac{\partial\mu}{\partial\rho}\right)_{T,q} \delta\rho(r, t) + \left(\frac{\partial\mu}{\partial q}\right)_{T,\rho} \delta q + \left(\frac{\partial\mu}{\partial T}\right)_{T,\rho} \delta T, \quad (1.113)$$

so that eq. 1.108 becomes:

$$\frac{\partial}{\partial t}q(\mathbf{r}, t) = \sigma \left[-\frac{4\pi}{\epsilon} + \frac{1}{e} \left(\frac{\partial \mu}{\partial q} \right)_{T,\rho} \nabla^2 \right] q(\mathbf{r}, t) + \Lambda \sigma \nabla^2 T(\mathbf{r}, t) + \nu \sigma \nabla^2 \rho(\mathbf{r}, t). \quad (1.114)$$

Here

$$\Lambda = \frac{\alpha}{\sigma T_0} + \frac{1}{e} \left(\frac{\partial \mu}{\partial T} \right)_{T,q} \quad (1.115)$$

$$\nu = \frac{1}{\rho_0} \left(\frac{\partial P}{\partial q} \right)_{T,\rho}, \quad (1.116)$$

where the first describes thermoelectric effects and the second the electrostrictive effect. The last two term in 1.114 are equivalent to the last two obtained for a neutral system if eq. 1.78 is inserted in the conservation equation 1.76. The term $-4\pi\sigma q(\mathbf{r}, t)/\epsilon$ in 1.114 is, instead, peculiar of Coulomb fluids. It introduces a further Q -dependence of δq , as can be easier view by Laplace-Fourier transforming 1.114, i.e.:

$$zq(\mathbf{Q}, z) = \left[-\frac{4\pi\sigma}{\epsilon} - Q^2 \frac{\sigma}{e} \left(\frac{\partial \mu}{\partial q} \right)_{T,\rho} \right] q(\mathbf{Q}, z) - \Lambda \sigma Q^2 T(\mathbf{Q}, z) - \nu \sigma Q^2 \rho(\mathbf{Q}, z). \quad (1.117)$$

In the limit $Q \rightarrow 0$, the term $-4\pi\sigma q(\mathbf{r}, t)/\epsilon$ is dominant in eq. 1.117, whereas in the limit of large Q , where $\frac{\sigma}{e} \left(\frac{\partial \mu}{\partial q} \right)_{T,\rho} Q^2 \gg \frac{4\pi\sigma}{\epsilon}$ it is negligible and 1.117 reduces to the equivalent for neutral systems, since the interdiffusion coefficient in a ionic mixture is defined as $D_{12} = \frac{\sigma}{\rho_0 \epsilon}$. The treatment for neutral systems previously illustrated is then applicable to the ionic mixtures in such Q region. This equivalence can be related to the screening effects in a ionic mixture. If one considers the presence of an external, static charge density, $q_e(\mathbf{r})$, the Poisson equation reads:

$$\nabla \cdot \mathbf{E}(\mathbf{r}) = \frac{4\pi}{\epsilon} [q(\mathbf{r}) + q_e(\mathbf{r})]. \quad (1.118)$$

Making use of the relation $\nabla^2 \rho(\mathbf{r}) = -\rho(\mathbf{r})^2 \nu k_T \nabla^2 q(\mathbf{r})$, and of eq. 1.118 and eq. 1.117 one obtains:

$$\sigma \left[-\frac{4\pi}{\epsilon} + \frac{1}{e} \left(\frac{\partial \mu}{\partial q} \right)_{T,\rho} Q^2 - \nu \rho_0^2 k_T Q^2 \right] q(\mathbf{Q}) - \frac{4\pi\sigma}{\epsilon} q_s(\mathbf{Q}) = 0. \quad (1.119)$$

It is solved for:

$$q(\mathbf{Q}) = - \left[1 + \frac{Q^2}{Q_s^2} \right] q_e(\mathbf{Q}), \quad (1.120)$$

where

$$Q_s = \frac{4\pi e}{\epsilon} \left[\left(\frac{\partial \mu}{\partial q} \right)_{T,\rho} - e\rho^2 \nu^2 k_T \right]^{-\frac{1}{2}} \quad (1.121)$$

is the inverse of the screening length, λ_s . The condition under which the Q^2 terms are dominant in 1.119, i.e. where the ionic mixture can be treated as equivalent to a neutral one, is $\frac{4\pi}{\epsilon} \ll \frac{1}{e} \left(\frac{\partial \mu}{\partial q} \right)_{T,\rho} Q^2 - \nu \rho_0^2 k_T Q^2$, i.e. $Q \gg Q_s$. This is equivalent to the condition of perfect screening, i.e. where $q_e(\mathbf{Q}) = 0$. In the case of non-static conditions a simplified relation which permit to identify a wavevectors region where the behavior of the ionic mixture is isomorphous to that of a neutral one can be found in the hypothesis that the relaxation terms proportional to Q^2 in the hydrodynamics equations are small compared to $c_s Q$. In the variables set (ρ, q, T, u) the hydrodynamic matrix is:

$$\begin{pmatrix} z & 0 & 0 & \rho_0 \\ \sigma \gamma Q^2 & z + \frac{4\pi\sigma(\mathbf{Q})}{\epsilon} & \sigma \Lambda Q^2 & 0 \\ \frac{\gamma \sigma \nu \Lambda T Q^2}{\rho_0 c_P} & \frac{4\pi \gamma \Lambda T \sigma(\mathbf{Q})}{\epsilon \rho_0 c_P} & \frac{z + \gamma(\lambda + \sigma \Lambda^2 T) Q^2}{\rho_0 c_P} & \frac{\gamma - 1}{\alpha} \\ \frac{-Q^2}{\rho_0^2 k_T} & -\nu Q^2 & -\frac{\alpha Q^2}{\rho_0 k_T} & z + \eta_L Q^2 \end{pmatrix}, \quad (1.122)$$

with

$$\sigma(\mathbf{Q}) = \sigma \left[1 + \frac{\epsilon}{4\pi e} \left(\frac{\partial \mu}{\partial q} \right)_{T,\rho} Q^2 \right]. \quad (1.123)$$

The dispersion relation can be written as:

$$\left(z + \frac{4\pi\sigma}{\epsilon} + \tilde{z}_1 Q^2 \right) (z + \tilde{z}_2 Q^2) (z - ic_s Q + \Gamma Q^2) (z + ic_s Q + \Gamma Q^2). \quad (1.124)$$

The coefficients of the Q^2 relaxation terms can be determined by comparison with 1.122 within the hypothesis they are small to respect to $c_s Q$. Three different regimes emerges from this kind of analysis:

- *Kubo regime* ($4\pi\sigma/\epsilon \gg c_s Q$) In this regime the charge fluctuation mode is uncoupled from the mass and temperature fluctuation modes. These last are, in fact, analogous to these of a one component fluid, being:

$$z_1 = \sigma \left[\frac{4\pi}{Q_s^2} + \frac{T\Lambda_P^2}{\rho_0 c_P} + \gamma k_T \rho_0^2 \tilde{\nu}^2 \right] \quad (1.125)$$

$$z_2 = D_T \quad (1.126)$$

$$\Gamma = \frac{1}{2} [\eta_L + (\gamma - 1)D_T], \quad (1.127)$$

where

$$\Lambda_P = \frac{\alpha}{\sigma T} + \frac{1}{e} \left(\frac{\partial \mu}{\partial T} \right)_{P,q} \quad (1.128)$$

$$\tilde{\nu} = \nu + \frac{\Lambda_P T \alpha}{\rho_0^2 c_P k_T} \quad (1.129)$$

In this regime the Kubo relations for the transport coefficients hold ³.

- *Two-component regime* ($4\pi\sigma/\epsilon \ll c_s Q$) In this regime, all the relaxation frequency are small compared with the sound wave frequency. The behavior of the ionic fluid becomes similar to that of a two-component neutral fluid, with electrical conduction playing the role of interdiffusion, being

$$z_1 = \sigma \left[\frac{4\pi}{Q_s^2} + \frac{T\Lambda_P^2}{\rho_0 c_P} \right] \quad (1.130)$$

$$z_2 = D_T \quad (1.131)$$

$$\Gamma = \frac{1}{2} \left[\eta_L + (\gamma - 1)D_T + \frac{(c_s Q)^2}{(c_s Q)^2 + (4\pi\sigma/\epsilon)^2} \gamma k_T \rho_0^2 \tilde{\nu}^2 \sigma \right] \quad (1.132)$$

³The Kubo relations are

$$\begin{aligned} \lim_{\omega \rightarrow 0} \omega^4 [\lim_{Q \rightarrow 0} Q^{-4} S_{\rho\rho}(Q, \omega)] &= 2k_B T \eta_L \\ \lim_{\omega \rightarrow 0} \omega^4 [\lim_{Q \rightarrow 0} Q^{-4} S_{TT}(Q, \omega)] &= 2k_B \left(\frac{T}{\rho c_V} \right)^2 \lambda. \end{aligned}$$

1. Collective modes and fluid dynamics

- *Intermediate regime* ($4\pi\sigma/\epsilon \sim c_s Q$) here interpolation formulas between the two previous limiting cases can be found, e.g.:

$$z_1 = \sigma \left[\frac{4\pi}{Q_s^2} + \frac{T\Lambda_P^2}{\rho_0 c_P} + \frac{(c_s Q)^2}{(c_s Q)^2 + (4\pi\sigma/\epsilon)^2} \gamma k_T \rho_0^2 \tilde{\nu}^2 \right] \quad (1.133)$$

$$\Gamma = \frac{1}{2} \left[\eta_L + (\gamma - 1) D_T + \frac{(c_s Q)^2}{(c_s Q)^2 + (4\pi\sigma/\epsilon)^2} \gamma k_T \rho_0^2 \tilde{\nu}^2 \sigma \right] \quad (1.134)$$

With typical values for molten salts, i.e. $4\pi\sigma/\epsilon \sim 5\text{meV}$ and $c_s \sim 0.5\text{meV/nm}^{-1}$, one finds the transition at $Q^* \sim 10\text{nm}^{-1}$, corresponding to a transition wavelength of the order of a few interatomic distances, where classical hydrodynamics is already ruled out. The hydrodynamic behavior of such systems is thus usually governed by eqs. 1.125-1.127. It may be, however, possible to observe the transition from one regime to the other in ionic system of low σ/ϵ and high $\tilde{\nu}$. Moreover, in the two-component regime for a ionic mixture it is in principle possible to apply the treatment described in 1.2.2.2. Generalizing the expression 1.101:

$$\xi_i = c(1-c) \left(\frac{\partial \mu}{\partial q} \right)_{T,P} \sigma^{-1} (e^2 z \rho_0). \quad (1.135)$$

If $Q^* = \frac{4\pi\sigma}{\epsilon c_s}$: $\omega(Q^*) = c_s Q^* = \frac{4\pi\sigma}{\epsilon} \gg \xi_i$ the continuity equation 1.100 can be applied.

Once the solutions of the hydrodynamic matrix are known, the dynamic structure factors S_{ij} , where $i, j = \rho, q, T, w$ can be calculated. It is obtained:

$$\begin{aligned} S_{ij}(Q, \omega) = & f_{ij}(Q) \left[\frac{2A_{ij}(Q)(4\pi\sigma/\epsilon)}{\omega^2 + (4\pi\sigma/\epsilon + z_1 Q^2)^2} + \frac{2B_{ij} z_2 Q^2}{\omega^2 + (z_2 Q^2)^2} + \right. \\ & C_{ij}(Q) \left(\frac{\Gamma Q^2}{(\omega + c_s Q)^2 + (\Gamma Q^2)^2} + \frac{\Gamma Q^2}{(\omega - c_s Q)^2 + (\Gamma Q^2)^2} \right) + \\ & \left. (c_s Q)^{-1} D_{ij}(Q) \left(\frac{\omega + c_s Q}{(\omega + c_s Q)^2 + (\Gamma Q^2)^2} + \frac{\omega - c_s Q}{(\omega - c_s Q)^2 + (\Gamma Q^2)^2} \right) \right] \end{aligned} \quad (1.136)$$

The values of the coefficients $f_{ij}(Q)$ are related to the static correlation functions $S_{ij}(Q)$, whereas the coefficients $A_{ij}, B_{ij}, C_{ij}, D_{ij}$ depend on which regime we are.

Approximate expressions for these coefficients can be derived and, in all regimes, it was found that C_{qq} and D_{qq} are negligible. Within this treatment we can not associate propagating modes to charge fluctuations correlations in this regime.

1.3 Mesoscopic region: the memory function approach

The main idea of memory function framework is to describe the dynamics of many body interacting system, using a limited number of dynamical variables. The first step is thus to rewrite the equations of the N -body dynamics in terms of these variables in a formally exact way.

Given the set of $\nu < N$ dynamical variables, $A_\nu(t)$ and being H the Hamiltonian which describes the N -body system in the phase space $(\mathbf{r}_i, \mathbf{p}_i)$, the equation of motion of $A_\nu(t)$ is ruled by the Liouville operator, iL [4, 39]:

$$\frac{dA_\nu(t)}{dt} = [dA_\nu(t), H] = iLA_\nu(t), \quad (1.137)$$

where $[..., ...]$ are the Poisson brackets. Equation 1.137 can be formally solved yielding:

$$A_\nu(t) = e^{iLt} A_\nu(0) \quad (1.138)$$

The solution is thus given in terms of the propagator e^{iLt} . Eq. 1.138 is too complicated to be applied in practice. The problem is, then, rephrased in a different way, as described in the following.

A projector operator, \wp , can be defined as:

$$\wp \equiv (\mathbf{A}(0), \dots) \cdot (\mathbf{A}(0), \mathbf{A}(0))^{-1} \mathbf{A}(0) \quad (1.139)$$

where \mathbf{A} is a n -dimensional vector whose components are the A_ν and $(..., ...)$ denotes a scalar product. If \wp is applied to an arbitrary dynamical variable, the "portion" of such variable that lies in the subspace defined by the set (A_ν) can

be extracted. After simple mathematical manipulation, it is possible to derive the Generalized Langevin Equation of motion [4, 39]:

$$\frac{d\mathbf{A}(t)}{dt} = i\Omega \cdot \mathbf{A}(t) - \int_0^t K(\tau) \cdot \mathbf{A}(t - \tau) d\tau + \mathbf{f}(t), \quad (1.140)$$

where:

- $K(t) = (\mathbf{f}, \mathbf{f}(t)) \cdot (\mathbf{A}(0), \mathbf{A}(0))^{-1}$ is a $n \times n$ matrix, referred to as memory matrix, or memory function if the set A_ν reduces to one variable.
- $\mathbf{f}(t) = e^{i(1-\varphi)Lt} i(1-\varphi)L\mathbf{A}(0)$ is a fluctuating force. It has the property to be orthogonal to $\mathbf{A}(0)$, i.e. $(\mathbf{A}(0), \mathbf{f}(t)) = 0$.
- $i\Omega = (\mathbf{A}(0), iL\mathbf{A}(0)) \cdot (\mathbf{A}(0), \mathbf{A}(0))^{-1}$ is an $n \times n$ antisymmetric matrix, referred to as proper frequency matrix. It can be valuated in terms of equilibrium (statical) properties of the system ⁴.

The equation of motion for the correlation matrix $C(t) = \langle \mathbf{A}(t)\mathbf{A}(0) \rangle$ is obtained from 1.140. Exploiting the orthogonality of $\mathbf{A}(0)$ and $\mathbf{f}(t)$ one obtains:

$$\frac{dC(t)}{dt} = i\Omega \cdot C(t) - \int_0^t K(\tau) \cdot C(t - \tau) d\tau \quad (1.141)$$

Equations 1.140 and 1.141 are the so-called memory equations or generalized Langevin equations. Since Ω can be calculated from statical properties of the system, the dynamical problem is now transposed from $C(t)$ to $K(t)$.

From the given mathematical structure of eq. 1.141, and from the fact that $K(\tau)$ itself is the time correlation function of $f(t)$, it is possible to obtain a recursive formula for $C(t)$, the so-called continued fraction representation [4, 39]. In fact, defining the projector operator:

$$\wp_1 \equiv \frac{(f(0), \dots)}{(f(0), f(0))} f(0), \quad (1.142)$$

⁴From eq. 1.137 $iL\mathbf{A}(0) = [\frac{d\mathbf{A}(t)}{dt}]_{t=0}$. The elements of the matrix Ω can be, then, defined such as $i\Omega_{ij} = [\partial/\partial t(A_i(0), iLA_j(0)) \cdot (A_i(0), A_j(0))^{-1}]_{t=0}$. It follows that if $(A_i(0), A_j(t))$ is even under time inversion, $\Omega_{ij} = 0$. This is, e.g., the case of $A_i(t) \equiv A_j(t)$ and of $A_{i,j}(t) \equiv n_{i,j}(r, t)$, where the last quantities are partial densities in a mixture, or linear combination of them.

a generalized Liouville equation for $f(t)$ can be written:

$$\frac{df(t)}{dt} = - \int_0^t K_1(\tau) f(t - \tau) d\tau + f_1(t). \quad (1.143)$$

$f_1(t)$ is a fluctuating force, orthogonal both to $A(t)$ and $f(t)$, while $K_1(t) = (f_1(0), f_1(t))/(f(0), f(0))$ is the so-called 2th order memory function. In analogy to 1.141, a memory equation for the memory function itself is obtained:

$$\frac{dK(t)}{dt} = i\Omega_1 \cdot K(t) - \int_0^t K_1(\tau) \cdot K(t - \tau) d\tau \quad (1.144)$$

In the Laplace space, the eqs. 1.141 and 1.144 reads:

$$C(z) = C(0)[zI + i\Omega + K(z)]^{-1}, \quad (1.145)$$

$$K(z) = \frac{K(0)}{[zI + i\Omega_1 + K_1(z)]}. \quad (1.146)$$

where I is the identity matrix. Iterating the procedure, an infinite set of equations such as 1.145 and 1.146 are obtained. Combining all of them, the continued fraction expansion is derived:

$$\frac{C(z)}{C(0)} = \left[z + \frac{\Delta_1}{z + \frac{\Delta_2}{z + \frac{\Delta_3}{z + \dots}}} \right]^{-1}, \quad (1.147)$$

where the terms Δ_i are the $t = 0$ values of the i^{th} order memory function.

1.3.1 One-component systems: the case of density fluctuations

An expression for $F(\mathbf{Q}, t)$ in the Laplace space can be easily obtained using eq. 1.147 for the Van-Hove pair correlation function:

$$\frac{\langle \delta\rho(\mathbf{Q}, 0)^* \delta\rho(\mathbf{Q}, z) \rangle}{F(\mathbf{Q}, 0)} = \frac{\tilde{F}(\mathbf{Q}, z)}{F(\mathbf{Q}, 0)} = \left[z + \frac{\Delta_1}{z + \frac{\Delta_2}{z + \frac{\Delta_3}{z + \dots}}} \right]^{-1} \quad (1.148)$$

where $F(Q, 0)$ and the Δ_i are now expressed in terms of spectral momenta of density fluctuations, i.e. the sum rules of $S(Q, \omega)$, reported in eqs. 1.41. The

$S(Q, \omega)$ can be derived by eq. 1.148, i.e.:

$$S(Q, \omega) = \frac{1}{2\pi} \int_{-\infty}^{\infty} dt e^{i\omega t} F(Q, t) = \frac{1}{\pi} \Re(\tilde{F}(Q, z = -i\omega)), \quad (1.149)$$

where \Re stand for the real part and $\tilde{F}(Q, z = -i\omega)$ is the Laplace transform of $F(Q, t)$. If the continuum fraction representation is limited to the second order, eq. 1.148 becomes:

$$\frac{\tilde{F}(\mathbf{Q}, z)}{F(\mathbf{Q}, 0)} = [z + \frac{c_0^2(Q)Q^2}{z + m_L(Q, z)}]^{-1}, \quad (1.150)$$

where $m_L(Q, z)$ is the second order memory function and $c_0(Q) = (k_B T Q^2 / M S(Q))^{1/2}$ is the zero frequency sound velocity. It can be identified with the isothermal sound velocity c_T :

$$c_0(Q) = c_T(Q) = c_s(Q) / \sqrt{\gamma}. \quad (1.151)$$

By comparison with eq. 1.66, after some algebra, the classical hydrodynamic expression for $\tilde{F}(Q, z)$ can be derived:

$$[\frac{\tilde{F}(Q, z)}{S(Q)}]_{hydro} = [z + \frac{(c_T Q)^2}{z + 2\Gamma Q^2 + \frac{(\gamma-1)(c_T Q)^2}{z + D_T Q^2}}]^{-1} \quad (1.152)$$

Comparing eqs. 1.150 and 1.152, it turns out that the expression for the memory function in the time domain is:

$$m_{L,hydro}(Q, t) = (\gamma - 1)(c_T Q)^2 e^{-\gamma D_T Q^2 t} + 2\Gamma Q^2 \delta(t). \quad (1.153)$$

Eq. 1.153 contains two terms which define its time decay from the initial, $t = 0$, value down to zero: the first one was a finite decay time, $\tau_T = 1/\gamma D_T Q^2$, referred as thermal relaxation time, and the second one describes an instantaneous time decay, i.e. $\propto \delta(t)$. In the hydrodynamic regime, τ_T is much longer than the period of inelastic excitations, $\Omega_L^{-1}(Q)$, the latter being $\propto Q^{-1}$ while the former $\propto Q^{-2}$. As a consequence the condition $\omega\tau_T \gg 1$ is always satisfied. In such a limit $m_{L,hydro}(Q, z = i\omega) \cong \Gamma Q^2 + \frac{i}{z} [c_s^2(Q) - c_T^2(Q)]$ and $S(Q, \omega)$ obtained through 1.150 reduces to the one reported in eq. 1.68. In the opposite limit, $\omega\tau_T \ll 1$,

$m_{L,hydro}(Q, z = i\omega) \cong (\gamma - 1)\tau_T(c_T Q)^2 + \Gamma Q^2 + \frac{i}{z}[c_s^2(Q) - c_T^2(Q)]$. The corresponding $S(Q, \omega)$ consists of a Brillouin doublet with maxima at $\pm c_T(Q)Q$ and a damping given by $(\gamma - 1)\tau_T(c_T Q)^2 + \Gamma Q^2$.

The illustrated phenomenology is an example of how relaxation processes (in this case the thermal relaxation), introduced through the memory function formalism, influence the lineshape of $S(Q, \omega)$. In a general point of view, an acoustic wave travelling with momentum (Q) and frequency (Ω_L) can be view as a time-dependent perturbation. It creates compression-rarefaction zones (CRZ), which are periodic in time ($T = 1/\Omega_L$) and space ($\Lambda = 1/Q$). The wave locally compresses the system, and the energy associated to such compression locally brings the system out of the equilibrium. Then the system relaxes into a new equilibrium position after a characteristic time (τ), dissipating the excess of energy. If $T \gg \tau$ the system has enough time to relax into its equilibrium position before the successive perturbation. This situation is referred to as fully relaxed limit. On the other hand, when $T \ll \tau$ the successive perturbation occurs before the system can relax. This situation is referred to as fully unrelaxed limit. The intermediate situation, $\tau \sim T$, defines the crossover between the two regimes. Beside the characteristic timescale, a characteristic strength, Δ^2 , can be associated with a relaxation process. In the memory function formalism, Δ^2 represents the $t = 0$ value of the considered relaxation in the memory function. The information one can obtain from $S(Q, \omega)$, then depends on the considered regime:

- Fully relaxed regime ($\omega\tau \ll 1$): the time-decay of $m_L(Q, t)$ is so short compared to the frequency window that it can be approximated by a $\delta(t)$ -function: i.e. $m(Q, t) \rightarrow 2A(Q)\delta(t)$, with $A(Q) = \int_0^{+\infty} m_L(Q, t)dt$. The information one can derived from $S(Q, \omega)$ are the values of $A(Q)$ and of c_T .
- Fully unrelaxed regime ($\omega\tau \gg 1$): the physical process responsible for the relaxation occurs on such a long time-scale that the energy carried by acoustic

waves cannot be dissipated in this channel. The information one can derive from $S(Q, \omega)$, once the value of c_T is known, is the relaxation strength, Δ^2 , which is responsible for the sound wave velocity increase from c_T to $\sqrt{c_T^2 + \Delta^2}$.

- In the crossover regime ($\omega\tau \sim 1$) $S(Q, \omega)$ is sensitive to both relaxation time and strength.

Dissipation phenomena that can be associated with a relaxation process are numerous in fluids: e.g. thermal diffusivity, viscous flows, inter-particles collisions, intramolecular vibrations or rotations [40,41]. A common approach in the study of fluid systems is to introduce a characteristic structural time, τ_α , for intermolecular interactions, such as the characteristic life-time of intermolecular bonds or the time between intermolecular collisions. In most cases, such a characteristic time scale is in the order of *ps*. When the system is probed on a timescale much shorter than τ_α it appears as "frozen", since the particles have neither the time to move significantly nor to make/break bonds. The response of the system is then expected to be similar to the one of an amorphous solid. The structural relaxation phenomenology can be introduced into the memory function formalism using the so-called Debye ansatz, which consists in replacing the instantaneous term ($2\Gamma Q^2 \delta(t)$) in eq. 1.153 by an exponential time decay with time constant τ_α and strength Δ_α^2 :

$$m_L(Q, t) = (\gamma - 1)(c_T Q)^2 e^{-\gamma D_T Q^2 t} + \Delta_\alpha^2 e^{-t/\tau_\alpha}. \quad (1.154)$$

In order to quantitatively retrieve the hydrodynamic limit in the low- (Q, ω) range, the following assumption has to be made:

$$\Delta_\alpha^2 \tau_\alpha = \Gamma Q^2. \quad (1.155)$$

The effect of the structural relaxation on the dispersive behavior of longitudinal modes is the following. For frequencies $\Omega_L(Q) \ll \tau_\alpha^{-1}$ (i.e. $\ll THz$) the fully

relaxed limit is reached. In this region the sound velocity, $c_L = \Omega_L(Q)/Q^5$, is the adiabatic one and the mode damping is given by eq. 1.155. This fully relaxed limit is also called viscous regime, because the system behaves like a viscous fluid that obeys the hydrodynamic laws. On increasing Q , $\Omega_L(Q)$ linearly increases, up to becomes comparable to τ_α^{-1} . In this region the sound velocity increases and the damping decreases. Further increasing Q , $\Omega_L(Q)$ becomes much larger than τ_α^{-1} . In this fully unrelaxed limit, also called elastic regime, the sound velocity does not further increase, but remains constant. This high frequency sound velocity is usually called c_∞ . The relation between c_∞ , c_s and Δ_α^2 is:

$$c_\infty^2 - c_s^2 = \Delta_\alpha^2/Q^2 \quad (1.156)$$

In conclusion, a dispersion of the sound velocity, from a low frequency limit (c_s) to an high frequency one (c_∞), is observed as a function of $\Omega_L(Q)\tau_\alpha$ (positive sound dispersion). The Q crossover is in the order of $1/c_s\tau_\alpha$. This phenomenology is also referred to as viscoelasticity. If The effects of thermal relaxation are neglected by imposing, e.g., $\gamma = 1$, the spectrum given by eqs. 1.149, 1.150 and 1.154 can be obtained by truncating the continued fraction expression to the third order:

$$\tilde{F}(Q, z) = F(Q, t = 0) \left(z + \frac{M(Q, t = 0)}{z + \frac{N(Q, t = 0)}{z + K(Q, t)}} \right)^{-1}, \quad (1.157)$$

where $M(Q, t = 0)$ and $N(Q, t = 0)$ are the first and second order memory function calculated at $t = 0$, respectively, and by supposing that third order memory function is a Dirac δ function, i.e. $K(Q, t) = K(Q)\delta(t)$. This implies, through Laplace transform, $\tilde{K}(Q, z) = K(Q)$. $M(Q, t = 0)$ and $N(Q, t = 0)$ are determined in terms of the n^{th} frequency moments of $S(Q, \omega)$ (see eqs. 1.41):

$$\begin{aligned} M(Q, t = 0) &= \langle \omega^2(Q) \rangle \langle \omega^0(Q) \rangle^{-1} \\ N(Q, t = 0) &= \langle \omega^4(Q) \rangle \langle \omega^2(Q) \rangle^{-1} - \langle \omega^2(Q) \rangle \langle \omega^0(Q) \rangle^{-1}. \end{aligned} \quad (1.158)$$

⁵ $\Omega_L(Q)$ can be defined as the maximum of $J_L(Q, \omega)$.

Substituting eqs. 1.158, 1.41 in eq. 1.157 and explicating, $S(Q, \omega)$ can be expressed as:

$$S(Q, \omega) = \frac{1}{\pi} \frac{S(Q)\omega_0^2(Q) \left(1 - \frac{\omega_0^2(Q)}{\omega_\infty^2(Q)}\right) \tau_c(Q)}{\omega_0(Q)^2 \left[\omega \tau_c(Q) \left(\frac{\omega^2(Q)}{\omega_\infty^2(Q)} - 1\right)\right]^2 + \left(\frac{\omega^2(Q)}{\omega_0^2(Q)} - 1\right)}, \quad (1.159)$$

with

$$\begin{aligned} \omega_\infty^2(Q) &= \langle \omega^4(Q) \rangle \langle \omega^2(Q) \rangle^{-1} = N(Q, t=0) + M(Q, t=0) \\ \omega_0(Q)^2 &= \langle \omega^2(Q) \rangle \langle \omega^0(Q) \rangle^{-1} = M(Q, t=0) = \frac{k_B T}{MS(Q)} \\ \tau_c &= K^{-1}(Q) \frac{\omega_\infty^2}{\omega_0^2}. \end{aligned} \quad (1.160)$$

The quantities $\omega_\infty(Q)$ and $\omega_0(Q)$ are related to the infinite and zero frequency extended velocities, c_∞ and c_0 , by the relations $\omega_{\infty(0)} = c_{\infty(0)}Q$. The compliance relaxation time, $\tau_c(Q)$, can instead be regarded as a Q -dependent Maxwell relaxation time.

It is also possible to give an approximate expression of $K^{-1}(Q)$ in terms of $\omega_\infty(Q)$ and $\omega_0(Q)$ by imposing that in the $Q \rightarrow \infty$ limit the correct short time behavior is obtained [42]. Since $M(Q, t=0)$, $N(Q, t=0)$ and $K(Q, t=0)$ are time correlations function, one can derive the following expressions:

$$\begin{aligned} \tilde{N}(Q, z) &= (z + K(Q))^{-1} N(Q, 0) \\ \tilde{M}(Q, z) &= (z + \tilde{N}(Q, z))^{-1} M(Q, 0), \end{aligned} \quad (1.161)$$

from which it follows:

$$K(Q) = \tilde{M}(Q, z=0) N(Q, 0) M(Q, 0)^{-1}. \quad (1.162)$$

The short time behavior of $M(Q, t)$ is obtained by its small time Fourier expansion:

$$M(Q, t) = \left(1 - \frac{t^2}{2} N(Q, 0) + \dots\right) M(Q, 0). \quad (1.163)$$

From 1.163 it is obtained $\tilde{M}(Q, 0) \approx \xi M(Q, 0) \sqrt{N(Q, 0)}$, where ξ is a constant factor taking into account the higher order neglected in 1.163. For $Q \rightarrow \infty$ $S(Q, \omega) = S_i(Q, \omega)$, where $S_i(Q, \omega)$ can be exactly calculate using the free-gas result; therefore:

$$S(Q, 0) = \left(\frac{1}{2\pi Q^2} \frac{M}{k_B T} \right)^{1/2}. \quad (1.164)$$

The above free-gas limit is obtained if $\xi = 2/\pi$ and

$$K(Q)^{-1} = \frac{\sqrt{\pi}}{2\sqrt{N(Q, 0)}}. \quad (1.165)$$

Finally, from 1.160, 1.158 and 1.165:

$$\tau_c(Q) = \frac{\sqrt{\pi}}{2} \frac{\omega_\infty}{\omega_0^2} \frac{1}{\sqrt{1 - \frac{\omega_0^2}{\omega_\infty^2}}}. \quad (1.166)$$

The above equation is also known as Lovesey relation. The following observations are worth. The truncation to the 3^{rd} order of the continued fraction using a $\delta(t)$ -function for $K(Q, t)$ is equivalent to the 2^{nd} order truncation using an exponential time decay for $M(Q, t)$ only if the following assumption are made:

- the decay induced by thermal fluctuations is negligible;
- all the active dynamic channels can be described by a single timescale.

1.3.2 Generalization to binary mixtures

The generalization of the memory function to binary systems is quite straightforward. As evident from the previous treatment, in fact, the memory function formalism holds for a generic set of ν dynamical variables. The physical problem is, therefore, deviate on the choice of the suitable set of variables describing the collective dynamics in the systems. In the case of binary mixtures, rather than the total density, the partial densities referred to single specie components (FZ

representation) has to be taken into account ⁶. The memory function for density fluctuation is then substituted by a memory matrix that has as basis the two partial densities fluctuations. In this case $S(Q, \omega)$ assumes the matricial form:

$$\mathbf{S} = \begin{pmatrix} S^{11} & S^{12} \\ S^{21} & S^{22} \end{pmatrix}, \quad (1.167)$$

where $S^{\alpha\beta}$ ($\alpha, \beta = 1, 2$) are defined in sec. 1.1. Consequently the relations 1.157-1.160 remain formally the same if all the quantities in the equations are replaced by matrices, the quantity z is multiplied for the identity matrix \mathbf{I} , the products are replaced by matrix product and the exponent -1 is considered as the matrix inversion. The matrix $\mathbf{S}(Q, \omega)$ has to be hermitian so that 1.149 becomes:

$$\mathbf{S}(Q, \omega) = \frac{1}{2\pi} [\tilde{\mathbf{F}}^+(Q, z = -i\omega) + \tilde{\mathbf{F}}(Q, z = -i\omega)], \quad (1.168)$$

where $\tilde{\mathbf{F}}^+$ is the adjoint of $\tilde{\mathbf{F}}$. The hermitian property of $\mathbf{S}(Q, \omega)$ implies that $S^{\alpha\beta}$ are real and $S^{12}(Q, \omega) = S^{21}(Q, \omega)$.

In order to provide an explicit expression for the matrix elements of $\mathbf{K}(Q)$ the same arguments reported in 1.161-1.165 for a single-component system can be followed, taking care to use proper matricial expressions. Explicit calculations can be found in [20] and they are reported here for sake of completeness:

$$\begin{aligned} K_{11} &= \frac{2}{\sqrt{\pi}} \frac{N_{12}(Q)N_{21}(Q)\lambda_1^{1/2}(Q) + \beta^2(Q)\lambda_2^{1/2}(Q)}{N_{12}(Q)N_{21}(Q) + \beta^2(Q)} \\ K_{12} &= \frac{2}{\sqrt{\pi}} \frac{N_{12}(Q)\beta(Q)[\lambda_1^{1/2}(Q) - \lambda_2^{1/2}(Q)]}{N_{12}(Q)N_{21}(Q) + \beta^2(Q)} \\ K_{21} &= \frac{2}{\sqrt{\pi}} \frac{N_{21}(Q)\beta(Q)[\lambda_1^{1/2}(Q) - \lambda_2^{1/2}(Q)]}{N_{12}(Q)N_{21}(Q) + \beta^2(Q)} \\ K_{22} &= \frac{2}{\sqrt{\pi}} \frac{N_{12}(Q)N_{21}(Q)\lambda_2^{1/2}(Q) + \beta^2(Q)\lambda_1^{1/2}(Q)}{N_{12}(Q)N_{21}(Q) + \beta^2(Q)} \end{aligned}$$

⁶Instead of the partial densities the total density and the mass-concentration variables, that are obtained from the first two through a basis changing, can be used. For more details see also 1.1.

where $N_{\alpha\beta}(Q)$ are the matrix elements of $\mathbf{N}(Q, t = 0)$ and

$$\begin{aligned}\lambda_1(Q) &= \frac{1}{2} [N_{11}(Q) + N_{22}(Q)] + \left[\left(\frac{N_{11} - N_{22}}{2} \right)^2 + N_{12}N_{21} \right]^{1/2} \\ \lambda_2(Q) &= \frac{1}{2} [N_{11}(Q) + N_{22}(Q)] - \left[\left(\frac{N_{11} - N_{22}}{2} \right)^2 + N_{12}N_{21} \right]^{1/2},\end{aligned}$$

with

$$\beta(Q) = \lambda_1(Q) - N_{11}(Q). \quad (1.169)$$

It is then possible to define the matrices of the compliance relaxation times as:

$$\mathbf{T}_c(Q) = \mathbf{K}^{-1} [1 + \mathbf{N}(Q, t = 0) \mathbf{M}^{-1}(Q, t = 0)]. \quad (1.170)$$

The choice of the FZ representation is based on the observation that in the limit of very large wavenumber it is expected that the partial density fluctuations, $\delta n_{1(2)}(Q, t)$, are independent dynamical variables (i.e. $S^{\alpha\beta}(Q, \omega) = 0$ for $\alpha \neq \beta$) by virtue of the incoherent character of the scattering at such Q 's. It has been shown [43] that a suitable choice of the dynamical variable can lead to a diagonalization of the second order memory function at $t = 0$, $\mathbf{N}(Q, t = 0)$. These variables can be obtained as a linear combination of $\delta n_{1(2)}(Q, t)$:

$$\begin{aligned}\delta A_1(Q, t) &= M_1^{1/2} \sin \theta(Q) \delta n_1(Q, t) + M_2^{1/2} \cos \theta(Q) \delta n_2(Q, t) \\ \delta A_2(Q, t) &= M_1^{1/2} \cos \theta(Q) \delta n_1(Q, t) - M_2^{1/2} \sin \theta(Q) \delta n_2(Q, t),\end{aligned} \quad (1.171)$$

where $M_{1(2)}$ are the masses of the two specie components. The coefficient $\theta(Q)$ is fixed by imposing the condition $N_{A_1 A_2}(Q, t = 0) = N_{A_2 A_1}(Q, t = 0) = 0$. In $Q \rightarrow 0$ limit such condition is satisfied for $\sin \theta(Q) = M_1 / (M_1 + M_2)$, whereas in the limit $Q \rightarrow \infty$ for $\sin \theta(Q) = 0$. Such solutions correspond, respectively, to $\delta A_{1(2)} = \delta n(\delta c)$ (i.e the Bathia-Tornton (BT) representation) and $\delta A_{1(2)} = \delta n_{1(2)}$ (FZ representation). However, only when the cross term of $S(Q)$ vanishes (this condition is achieved, for example, at very high Q), $\mathbf{M}(Q, t = 0)$ is diagonal. In

this case the relations 1.161-1.165 hold for the single matrix elements and the Lovesey's relation (eq.1.166) for the compliance relaxation time can be applied, separately, to a single dynamical variable. In other terms, only in this case two independent viscoelastic functions, each one related to a given variable, can be used to model $S(Q, \omega)$.

1.3.3 Optic-like modes and viscoelastic model in binary ionic systems

As shown in 1.2.2.3 under the condition $4\pi\sigma/\epsilon \gg c_s Q$ (Kubo regime) the charge fluctuation mode is uncoupled from the mass and temperature fluctuation modes. Within the hypothesis that such a regime cover a Q range enough large, i.e. up to the mesoscopic region, it is possible to describe S_{qq} in the memory function framework treating the charge and total density fluctuations independently, i.e. without introducing a matrix memory function as in 1.3.2. The intermediate scattering function in the Laplace space for the charge fluctuations can be formally written as in 1.148, where $F(\mathbf{Q}, 0)$ and Δ_i are now expressed in terms of spectral momenta of charge fluctuations, i.e. the sum rules of $S_{qq}(Q, \omega)$. Limiting the continued fraction representation to the second order, as in 1.150, one obtains:

$$\frac{\tilde{F}_{qq}(\mathbf{Q}, z)}{F_{qq}(\mathbf{Q}, 0)} = \left[z + \frac{\Delta_1}{z + n_L(Q, z)} \right]^{-1}. \quad (1.172)$$

In the low Q limit $\Delta_1 \rightarrow \Omega_P^2$ [25], where Ω_P is the plasma frequency. Assuming that the second order memory function $n_L(Q, t)$ decays exponentially with a relaxation time equal to τ_L ⁷, 1.172 becomes [25]:

$$\frac{\tilde{F}_{qq}(\mathbf{Q}, z)}{F_{qq}(\mathbf{Q}, 0)} = \left[z + \frac{\Omega_P^2}{z + \frac{\Delta_L}{z+1/\tau_L}} \right]^{-1}. \quad (1.173)$$

The essential difference between the last expression and the equivalent for density fluctuations (eq.1.150), is that the Q dependent term, $c_0^2 Q^2$, is now substituted by

⁷This is equivalent to viscoelastic approximation introduced in 1.3.1.

the constant term, Ω_P^2 . This lead to two important consequences:

- $S_{qq}(Q, \omega)$ obtained from 1.173 has two different regimes depending on the frequency range: for $\omega\tau_L \ll 1$ the hydrodynamic expression 1.136 is recovered and no charge fluctuations propagating modes can be observed, while for $\omega\tau_L \gg 1$ a pair of propagating modes with characteristic frequency $\omega = \pm\omega_L$ can be identified, and they correspond to propagating charge fluctuations;
- ω_L does not linearly disperse in Q , but has a value comparable with the Ω_P , modified by the short-range interactions between ions. The charge fluctuations mode is referred to as optic-like mode because $\omega_L \neq 0$ for $Q \rightarrow 0$.

1.4 Single particle limit

In the high- Q limit the scattering is incoherent, that is it mainly occurs from a single particle. Providing that suitable hypothesis hold, the inelastic cross-section becomes a direct probe of the distribution of atomic momenta of the target system. The key approximation is that at sufficiently short time, the instantaneous vector position can be replaced by:

$$\hat{\mathbf{R}}_j(t) \simeq \hat{\mathbf{R}}_j(0) + \frac{t}{M_j} \hat{\mathbf{P}}_j, \quad (1.174)$$

where $\hat{\mathbf{P}}_j$ is the momentum operator and M_j the mass of the j^{th} particle. Eq. 1.174 says that over short enough times the particles travels freely. Writing the number density operator as in 1.4 and substituting it in 1.9 the expression 1.14 of the dynamic structure factor becomes:

$$S(\mathbf{Q}, \omega) = \frac{1}{2\pi\hbar N} \int_{-\infty}^{\infty} dt e^{-i\omega t} \sum_{j,j'} \langle e^{-i\mathbf{Q}\cdot\hat{\mathbf{R}}_j(0)} e^{i\mathbf{Q}\cdot\hat{\mathbf{R}}_{j'}(t)} \rangle \quad (1.175)$$

Inserting 1.174 in 1.175 and using standard commutation relations between momentum and position, it follows that

$$\langle e^{-i\mathbf{Q}\cdot\hat{\mathbf{R}}_j(0)} e^{i\mathbf{Q}\cdot\hat{\mathbf{R}}_{j'}(t)} \rangle = e^{\frac{i\hbar t Q^2}{2M_j}} \langle e^{i\mathbf{Q}\cdot(\hat{\mathbf{R}}_{j'} - \hat{\mathbf{R}}_j) + \frac{i\hbar t}{M_{j'}} \mathbf{Q}\cdot\hat{\mathbf{P}}_j} \rangle. \quad (1.176)$$

In the high- Q limit only terms with $j = j'$ are retained, so that

$$\langle e^{-i\mathbf{Q}\cdot\hat{\mathbf{R}}_j(0)} e^{i\mathbf{Q}\cdot\hat{\mathbf{R}}_j(t)} \rangle \cong e^{\frac{i\hbar t Q^2}{2M_j}} \langle e^{\frac{i\hbar t}{M_j} \mathbf{Q}\cdot\hat{\mathbf{P}}_j} \rangle. \quad (1.177)$$

Eq. 1.177 shows that the scattering is entirely incoherent and gives an approximate expression of the correlation function $\langle e^{-i\mathbf{Q}\cdot\hat{\mathbf{R}}_j(0)} e^{i\mathbf{Q}\cdot\hat{\mathbf{R}}_j(t)} \rangle$. Substituting it in 2.16, one finds:

$$S_i(\mathbf{Q}, \omega) = \frac{1}{2\pi\hbar N} \int_{-\infty}^{\infty} dt e^{-i\omega t} \sum_j \langle e^{\frac{i\hbar t}{M_j} \mathbf{Q}\cdot\hat{\mathbf{P}}_j} \rangle e^{\frac{i\hbar t Q^2}{2M_j}}. \quad (1.178)$$

The correlation function in 1.178 is evaluated by using the one-particle reduced density matrix:

$$\langle e^{\frac{i\hbar t}{M_j} \mathbf{Q}\cdot\hat{\mathbf{P}}_j} \rangle = \int d\mathbf{P} n(\mathbf{P}) e^{\frac{i\hbar t}{M} \mathbf{Q}\cdot\mathbf{P}_j}, \quad (1.179)$$

where $n(\mathbf{P})$ is the single particle momentum distribution, i.e. the diagonal element of the one-particle reduced density matrix. In the so-called impulse approximation (IA), based on eq. 1.174, the dynamic structure factor is finally:

$$S_{IA}(\mathbf{Q}, \omega) = \int d\mathbf{P} n(\mathbf{P}) \delta(\hbar\omega - \hbar\omega_r - \mathbf{P} \cdot \hbar\mathbf{Q}), \quad (1.180)$$

where $\hbar\omega_r$ is the recoil energy:

$$\hbar\omega_r = \frac{\hbar^2 Q^2}{2M}. \quad (1.181)$$

The δ function in eq. 1.180 is the mathematical statement that kinetic energy and momentum are conserved in the probe-particle collision. This is formally true as far as the probe-target interactions are negligible. In this case $\hbar\omega_r$ is the kinetic energy of the struck particle. The effect of the recoil term in $S_{IA}(\mathbf{Q}, \omega)$ is an

energy shift of $-\hbar\omega_r$ of the whole spectrum. Since ω_r depends on M , different mass particles in the sample can be distinguished in the observed spectrum.

In general there is no rigorous method to determine the values of Q above which one can apply the IA. Roughly speaking, the IA starts to be valid when the atomic nearest-neighbor distance is substantially greater than $\frac{2\pi}{Q}$, so that the interference of the scattering amplitudes from different atoms averages to zero. The second hypothesis that has to hold, i.e. the short-time hypothesis embodied in eq. 1.174, gives more detailed indication in concerning the validity of the IA. In the following a brief discussion of this point will be done and some corrections to extend the treatment at lower time scales will be introduced. Firstly, a decay time of the correlation function, reported in eq. 1.177, can be defined as:

$$\tau = \frac{M}{Q\Delta P}, \quad (1.182)$$

where ΔP is the width of the momentum distribution of the struck particle. This decay time is due to phase cancellation generated by the velocity spread of the particles. When there are no deviations from a free particle motion over a time extend of τ , the IA holds even if the target particles is surrounded by other particles. Deviations from free motion can be due to interactions with these neighbors. These cause finite forces inducing a particles displacement with respect to a straight trajectory. It can be shown that this corrective term is proportional to t^2 , while the displacement associated to the particle momentum is proportional to t . Consequently, as Q increases, the characteristic time scale of the system, i.e. τ , decreases and the IA becomes asymptotically exact. Quantifying the previous considerations, a criterion for the validity of the impulse approximation is:

$$\omega(\mathbf{Q})\tau \ll 1, \quad (1.183)$$

being $\omega(\mathbf{Q})$ the oscillation frequency for the particle confined in the potential of nearest neighbors. If the criterion is satisfied, the particle traverses an enough

small part of its orbit that the motion can be treated as free. Since the value of $\omega(\mathbf{Q})$ is bounded, the impulse approximation will always be satisfied for sufficiently large Q -values.

If the scattering particle is inhibited by intermolecular forces from recoiling freely, at a finite value of Q , effects arising from final state interactions have to be taken into account. They produce a narrowing of the energy distribution of the scattered particles. The finite- Q deviations from the IA are then generally referred to as final state effects. For a classical system in thermodynamic equilibrium, the momentum distribution is Maxwellian:

$$n(\mathbf{P}) = \left(\frac{2\pi k_B T}{M} \right)^{-\frac{3}{2}} e^{-\frac{P^2}{2Mk_B T}}, \quad (1.184)$$

where k_B is the Boltzmann constant and T the equilibrium temperature of the system. Substituting 1.184 in 1.180:

$$S_{IA}(Q, \omega) = \frac{1}{Q \left(\frac{2\pi k_B T}{m} \right)^{1/2}} e^{-\frac{(\omega - \omega_r)^2}{2Q^2 k_B T/M}}. \quad (1.185)$$

A convenient starting point for the discussion of final-state interactions is the Gram-Charlier expansion:

$$S_{IA}(Q, \omega) = \frac{1}{Q \left(\frac{2\pi k_B T}{m} \right)^{1/2}} e^{-\frac{(\omega - \omega_r)^2}{2Q^2 k_B T/M}} \cdot \sum_{n=0}^{\infty} \epsilon_n(Q) \hat{H}_n \left[\frac{(\omega - \omega_r)}{Q(2k_B T/M)^{1/2}} \right], \quad (1.186)$$

in which $\hat{H}_n(x)$ denotes the Hermite polynomials. The first five coefficients are:

$$\begin{aligned} \epsilon_0(Q) &= 1, \quad \epsilon_1(Q) = \epsilon_2(Q) = 0 \\ \epsilon_3(Q) &= \frac{\hbar \langle \nabla^2 V(\mathbf{r}) \rangle}{36M^2 (k_B T/2M)^{3/2} Q} \\ \epsilon_4(Q) &= \left(\frac{1}{6} \frac{\langle P_Q^4 \rangle}{\langle P_Q^2 \rangle^2} - \frac{1}{2} \right) + \frac{\langle \mathbf{F}^2 \rangle}{18(k_B T)^2}. \end{aligned} \quad (1.187)$$

Here $\langle P_Q \rangle$ is the moment $n(P)$ projected on the direction of \mathbf{Q} , $V(\mathbf{r})$ is the pair potential and $\mathbf{F} = \nabla V$ is the total force on the scattering atom. To obtain an

asymptotic expansion it's needed to express $\epsilon_n(Q)$ in inverse powers of Q and then regroup the terms in 1.186:

$$S_{IA}(Q, \omega) = \frac{1}{Q \left(\frac{2\pi k_B T}{m}\right)^{1/2}} e^{-\frac{(\omega - \omega_r)^2}{2Q^2 k_B T/M}} \cdot \sum_{m=0}^{\infty} \frac{1}{Q^m} \hat{G}_m \left[\frac{(\omega - \omega_r)}{Q(2k_B T/M)^{1/2}} \right]. \quad (1.188)$$

The $m = 0$ term in 1.188 gives $S_{IA}(Q, \omega)$, while the remaining terms give the corrections due to final-state interactions as an asymptotic series in inverse powers of Q . In summary, for sufficiently large values of Q the scattering function can be approximated by a single peak, which can be characterized by the frequency of the maximum Ω_0 and the full width at half maximum $\Delta\Omega$. These quantities can be written as [18, 24]:

$$\begin{aligned} \Omega_0 &= \omega_r(1 - \Phi(Q)) \\ \Delta\Omega &= 4(\ln 2)^{1/2} \left(\frac{k_B T}{2M}\right)^{1/2} (1 - \Gamma(Q)), \end{aligned} \quad (1.189)$$

where $\Phi(Q)$ and $\Gamma(Q)$ are the corrections to the IA due to final-state interactions. To evaluate these quantity explicitly for a particular system of interest an appropriate model for the interaction potential has to be introduced. Expression of $\Phi(Q)$ and $\Gamma(Q)$ for Lennard-Jones fluids can be found, e.g., in [18, 24].

Inelastic Scattering from fluids

The dynamics of a system, if related to atomic density fluctuations, can be studied by means of inelastic scattering experiments. They allow a direct determination of the dynamic structure factor $S(Q, \omega)$.

In the low Q and ω dynamic region, $S(Q, \omega)$ can be measured by photon correlation spectroscopy or ultrasonics techniques, which explore the frequency region between 1 MHz and 0.1 GHz . Brillouin light scattering is used to explore the so called hypersonic frequencies which extend from 5 to 20 GHz . Neutron and X-Ray scattering, conversely, probe a frequency range from 10^2 to 10^4 GHz . For a given dynamical process, a characteristic time, or equivalently length scale where the system relaxes to equilibrium, can be defined. For monoatomic gases this time is associated to the reciprocal collision time τ_c (in order of $psec$) between particles. The inverse of τ_c defines the crossover between the hydrodynamic region, where all the dynamical processes are relaxed (i.e. the system is in a state of local thermodynamic equilibrium), and the mesoscopic region, where the dynamical processes are unrelaxed and local (molecular) interactions became important. On the other hand, for more complex systems, as binary mixtures described in the previous chapter, it's appropriate to introduce different characteristic time scales. In this case the choice of the suitable experimental probe is crucial when a particular

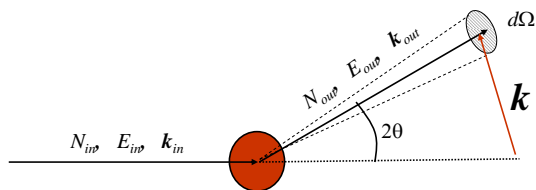


Figure 2.1: Kinematics of a scattering experiment.

dynamical process has to be analyzed.

2.1 Cross section for a scattering process

A general scattering process (fig. 2.1) is the collision of a particle (probe) with initial energy ω_i and momentum \mathbf{k}_i with a target. After the collision the particle is scattered into a different state (ω_f , \mathbf{k}_f) and detected by appropriate instruments. The wave function of the incoming and detected particles is described as a plane wave because both the source and scattered particles are assumed to be far enough from the target sample. Here, and in the following, the suffix i and f refer to the incident and scattered particles, respectively. According to energy and momentum conservation laws, the momentum and energy transferred to the target are:

$$\hbar\omega \doteq \hbar(\omega_f - \omega_i) \quad (2.1)$$

$$\hbar\mathbf{Q} \doteq \hbar(\mathbf{k}_f - \mathbf{k}_i). \quad (2.2)$$

The number of particles scattered from the sample per unit time into the element of solid angle $d\Omega = \sin(\theta)d\theta d\phi$ is:

$$N_s \propto N_i \frac{\partial^2 \sigma}{\partial \Omega \partial \omega_f} \Delta \Omega \Delta \omega_f, \quad (2.3)$$

where N_i is the number of incident particles per unit time per unit area and $\frac{\partial^2 \sigma}{\partial \Omega \partial \omega_f}$ is the double differential cross section. It is related to the probability of transition

per unit time of the particle probe from the state $|i\rangle$ to the state $|f\rangle$, W_{if} :

$$\frac{\partial^2 \sigma}{\partial \Omega \partial \omega_f} = \frac{1}{N_i} W_{if} \frac{\partial^2 n}{\partial \Omega \partial \omega_f} \quad (2.4)$$

where $\frac{\partial^2 n}{\partial \Omega \partial \omega_f}$ is the density of final scattering states. In the framework of first order perturbation theory, the probability W_{if} is given, according to the Fermi's Golden rule, by

$$W_{if} = \frac{2\pi}{\hbar} \sum_{|F\rangle|I\rangle} P_I |\langle I | \langle i | \hat{V} | f \rangle | F \rangle|^2 \delta(\hbar\omega - (E_F - E_I)) \quad (2.5)$$

being $|I\rangle$ ($|F\rangle$) the initial (final) states of the target, P_I is the equilibrium population of the initial states and \hat{V} is the interaction potential between the probe particles and the target system¹. In this condition the perturbation of the incident wave due to the scattering is small; in this way the scattered wave is proportional to the Fourier transform of the scattering potential. Assuming $|i\rangle$ and $|f\rangle$ as plane wave states and exploiting the conservation law 2.2, the double differential cross section is expressed by:

$$\frac{\partial^2 \sigma}{\partial \Omega \partial \omega_f} = \frac{1}{N_i} \frac{\partial^2 n}{\partial \Omega \partial \omega_f} \frac{2\pi}{\hbar} \sum_{|F\rangle|I\rangle} P_I |\langle I | \int d\mathbf{r} e^{-i\mathbf{Q}\cdot\mathbf{r}} \hat{V}(\mathbf{r}) | F \rangle|^2 \delta(\hbar\omega - (E_F - E_I)). \quad (2.6)$$

The interaction potential between the particles probe and the target is now assumed to be of the general form:

$$\hat{V}(\mathbf{r}) = \sum_j V_j(\mathbf{r} - \mathbf{R}_j), \quad (2.7)$$

where \mathbf{R}_j is the position vector of the j^{th} scattering center inside the target. The double differential cross section 2.6 is then:

$$\frac{\partial^2 \sigma}{\partial \Omega \partial \omega_f} = \frac{1}{N_i} \frac{\partial^2 n}{\partial \Omega \partial \omega_f} \frac{2\pi}{\hbar} \sum_{|F\rangle|I\rangle} P_I |\langle I | \sum_j \hat{V}_j(\mathbf{Q}) e^{i\mathbf{Q}\cdot\mathbf{R}_j} | F \rangle|^2 \delta(\hbar\omega - (E_F - E_I)). \quad (2.8)$$

¹In this equation the first Born approximation is also implicitly assumed. It's hold within the condition of weak interaction between probe and sample.

2. Inelastic Scattering from fluids

Writing the δ -function in the form:

$$\delta(\hbar\omega - (E_F - E_I)) = \frac{1}{2\pi\hbar} \int_{-\infty}^{\infty} dt e^{-\frac{it(\hbar\omega - (E_F - E_I))}{\hbar}} \quad (2.9)$$

and performing the sum over the final state in 2.8 by closure, the whole expression in the sum can be written as:

$$\frac{1}{2\pi\hbar} \int_{-\infty}^{\infty} dt e^{-i\omega t} \sum_{|I\rangle} P_I \sum_{j,j'} \langle I | \hat{V}_j^+(\mathbf{Q}) e^{i\mathbf{Q}\cdot\hat{\mathbf{R}}_j(0)} \hat{V}_{j'}(\mathbf{Q}) e^{i\mathbf{Q}\cdot\hat{\mathbf{R}}_{j'}(t)} | F \rangle. \quad (2.10)$$

Here \hat{V}^+ is the conjugate of \hat{V} and the operator $\hat{\mathbf{R}}_j(t)$ is defined in the Heisenberg representation by

$$e^{i\mathbf{Q}\cdot\hat{\mathbf{R}}_j(t)} = e^{\frac{it\hat{H}}{\hbar}} e^{i\mathbf{Q}\cdot\hat{\mathbf{R}}_j} e^{-\frac{it\hat{H}}{\hbar}} \quad (2.11)$$

being \hat{H} the Hamiltonian that describes the target system. The averaging over $|I\rangle$ involves both an average over different particles in the sample (it will be indicated by $\overline{\cdots}$), e.g. in the case of neutron scattering nuclear spin orientations or isotope distributions, and a thermal averaging. Finally:

$$\frac{\partial^2 \sigma}{\partial \Omega \partial \omega_f} = \frac{1}{N_i} \frac{\partial^2 n}{\partial \Omega \partial \omega_f} \frac{2\pi}{\hbar} \int_{-\infty}^{\infty} dt e^{-i\omega t} \sum_{j,j'} \overline{\hat{V}_j^+(\mathbf{Q}) \hat{V}_{j'}(\mathbf{Q})} \langle e^{-i\mathbf{Q}\cdot\hat{\mathbf{R}}_j(0)} e^{i\mathbf{Q}\cdot\hat{\mathbf{R}}_{j'}(t)} \rangle. \quad (2.12)$$

If the interaction potential \hat{V}_j is independent of j , 2.12 reduces to:

$$\frac{\partial^2 \sigma}{\partial \Omega \partial \omega_f} = \frac{1}{N_i} \frac{\partial^2 n}{\partial \Omega \partial \omega_f} |\overline{\hat{V}(\mathbf{Q})}|^2 (2\pi)^2 N S(\mathbf{Q}, \omega) \quad (2.13)$$

where

$$S(\mathbf{Q}, \omega) = \frac{1}{2\pi\hbar N} \int_{-\infty}^{\infty} dt e^{-i\omega t} \sum_{j,j'} \langle e^{-i\mathbf{Q}\cdot\hat{\mathbf{R}}_j(0)} e^{i\mathbf{Q}\cdot\hat{\mathbf{R}}_{j'}(t)} \rangle \quad (2.14)$$

and N is the number of scattering particles in the target. If this latter coincides with the particles carrying the microscopic mass in the target (e.g. the nuclei of atoms constituting the target), $S(\mathbf{Q}, \omega)$ corresponds to the dynamical structure factor: this contains all the informations on the density-fluctuations in the sample.

In the case of samples containing only one type of atoms (i.e. \hat{V}_j independent from j), eq. 2.13 emphasizes how the dynamical structure factor, describing the intrinsic properties of the investigated system, is separated from the terms describing the interaction between probe and target. As it will be shown in the following (see sec. 2.2), this peculiarity is lost in the case of samples containing two or more type of atoms.

It is useful to explicitly separate in 2.13 the contribution arising from the so-called coherent and incoherent scattering, because they carry different physical information. In 2.12 one writes:

$$\overline{\hat{V}_j^+(\mathbf{Q})\hat{V}_{j'}(\mathbf{Q})} = \overline{|\hat{V}_j(\mathbf{Q})|^2} + \delta_{j,j'}(\overline{|\hat{V}_j(\mathbf{Q})|^2} - \overline{|\hat{V}_j(\mathbf{Q})|^2}), \quad (2.15)$$

where the term $\overline{|\hat{V}_j(\mathbf{Q})|^2}$ is obtained for $j \neq j'$ and $\overline{|\hat{V}_j(\mathbf{Q})|^2}$ for $j = j'$. Coherent scattering preserves the relative phases of the wavelengths scattered from different location (j) in the sample. Considering that only the mean scattering potential can give interference effects, the coherent scattering cross-section is proportional to $\overline{|\hat{V}_j(\mathbf{Q})|^2}$. Incoherent scattering does not preserve a phase relationship between the incident and scattered wavelengths, i.e there is not interference and the scattering is completely isotropic. The deviations from the mean potential, being randomly distributed, cannot give interference effects. They therefore contribute to the incoherent scattering proportional to the mean square deviation, i.e. to $\overline{|\hat{V}_j(\mathbf{Q})|^2} - \overline{|\hat{V}_j(\mathbf{Q})|^2}$. From 2.14, putting $j = j'$ it remains defined the self dynamic structure factor:

$$S_i(\mathbf{Q}, \omega) = \frac{1}{2\pi\hbar N} \int_{-\infty}^{\infty} dt e^{-i\omega t} \sum_j \langle e^{-i\mathbf{Q}\cdot\hat{\mathbf{R}}_j(0)} e^{i\mathbf{Q}\cdot\hat{\mathbf{R}}_j(t)} \rangle. \quad (2.16)$$

It describe the dynamics of single-particles in the target sample. As follows from 2.15 and 2.13 the incoherent scattering is proportional to it.

2.1.1 Inelastic Neutron Scattering

If the particles probe are neutrons the following relations have to be considered:

$$\hbar\omega_{i(f)} = \frac{\hbar^2 k_{i(f)}^2}{2m} \quad (2.17)$$

$$p_{i(f)} = \hbar k_{i(f)}, \quad (2.18)$$

where $p_i(f)$ is the initial (final) momentum and m is the neutron mass. From these relations, N_i and $\frac{\partial^2 n}{\partial\Omega\partial\omega_f}$ are calculated, so that

$$\frac{\partial^2 \sigma}{\partial\Omega\partial\omega_f} = N \frac{k_f}{k_i} \left(\frac{m}{2\pi\hbar^2}\right)^2 \overline{|\hat{V}(\mathbf{Q})|^2} S(\mathbf{Q}, \omega) \quad (2.19)$$

The neutron interaction with the scattering system is the sum of two parts:

- the interaction of the neutron with the nuclei of the target via purely nuclear forces;
- the interaction between the magnetic momentum of the neutron and the magnetic momentum of the electrons of the target.

Neglecting the second contribution (i.e. assuming that the incident neutrons are unpolarized), the interaction potential is typically expressed in the form 2.7, where the generic term is

$$\hat{V}_j(\mathbf{r} - \mathbf{R}_j) = \frac{2\pi\hbar^2}{m} b_j \delta(\mathbf{r} - \mathbf{R}_j). \quad (2.20)$$

The quantity b_j is the scattering length of the j^{th} nucleus and it is related to the total cross-section by the relation:

$$\sigma_j = 4\pi |b_j|^2. \quad (2.21)$$

From 2.19 and 2.20, indeed:

$$\frac{\partial^2 \sigma}{\partial\Omega\partial\omega_f} = N \frac{k_f}{k_i} \overline{|b|^2} S(\mathbf{Q}, \omega). \quad (2.22)$$

It worths to observe that the neutrons directly interact with the nuclei of the particles, i.e. the condition within which the 2.14 can be identified with the dynamic structure factor of density fluctuations is automatically verified.

2.1.2 Inelastic X-Ray Scattering

The energy and momentum of photons are respectively described by the following relations:

$$\hbar\omega_{i(f)} = \hbar ck_{i(f)} \quad (2.23)$$

$$p_{i(f)} = \hbar k_{i(f)}, \quad (2.24)$$

where c is the speed of light. Eq. 2.13 becomes:

$$\frac{\partial^2 \sigma}{\partial \Omega \partial \omega_f} = \frac{\mathbf{k}_f^2}{2\pi \hbar c^2} |\widehat{V}(\mathbf{Q})|^2 NS(\mathbf{Q}, \omega) \quad (2.25)$$

Neglecting the interaction of the photons with the nuclei, the probe-target interaction is described, in the weak relativistic limit, by the photon-electron interaction \widehat{V}_{int} . It consists of four different terms [44]:

$$\begin{aligned} \widehat{V}_{int} = & \frac{e^2}{2mc^2} \sum_j \widehat{\mathbf{A}}(\mathbf{R}_j, t) \cdot \widehat{\mathbf{A}}^+(\mathbf{R}_j, t) + \frac{e}{2mc} \sum_j \widehat{\mathbf{A}}(\mathbf{R}_j, t) \cdot \mathbf{p}_j(\mathbf{R}_j, t) \\ & - \frac{e}{mc} \sum_j \mathbf{S}_j \cdot \nabla \times \widehat{\mathbf{A}}(\mathbf{R}_j, t) - \frac{e^2}{2m^4 c^4} \sum_j \mathbf{S}_j \cdot \left(\frac{d\widehat{\mathbf{A}}}{dt}(\mathbf{R}_j, t) \times \widehat{\mathbf{A}}(\mathbf{R}_j, t) \right) \end{aligned} \quad (2.26)$$

The sum is extended to all the electrons of system whose charge and mass is e and m , respectively. Electron spins are indicated as \mathbf{S}_j . $\widehat{\mathbf{A}}(\mathbf{R}_j, t)$ is the vector potential of the photon electromagnetic field. The first term in eq. 2.26 describe the diamagnetic coupling between the electron current and the photon electric field, it's usually referred as Thomson term. The second term accounts for paramagnetic coupling responsible for absorption/emission of a photon by the electron field. The last two terms describe the coupling of the electron spins to the photon magnetic field and the spin-orbit interaction. For photon energies in the order of 20 keV (i.e. $\ll mc^2$, the rest mass of the electron), the magnetic terms are smaller than the first two terms of about a factor 10^{-2} , and will therefore be neglected. Furthermore, for photon energies far from electronic transition energy,

2. Inelastic Scattering from fluids

the second term is not resonant with electronic level and can be neglected. The potential interaction 2.26 simplifies to:

$$\hat{V} = \frac{e^2}{2mc^2} \sum_j \hat{\mathbf{A}}(\mathbf{R}_j, t) \cdot \hat{\mathbf{A}}^+(\mathbf{R}_j, t) \quad (2.27)$$

Considering the quantum electrodynamic representation [45] and assuming the Lorentz's gauge $\nabla \cdot \mathbf{A}(\mathbf{R}_j, t) = 0$, the vector potential in 2.27 can be expressed as

$$\hat{\mathbf{A}}(\mathbf{R}_j, t) = \left(\frac{4\pi c^2}{V}\right)^{(1/2)} \sum_j [\hat{a}_\lambda \varepsilon_\lambda e^{iQ_\lambda \cdot \mathbf{R}_j} + \hat{a}_\lambda^+ \varepsilon_\lambda e^{-iQ_\lambda \cdot \mathbf{R}_j}]. \quad (2.28)$$

Here \hat{a}_λ^+ (\hat{a}_λ) are the λ^{th} component of the creation (annihilation) photon operator and ε_λ is the polarization of the electromagnetic field. The double differential cross-section for IXS can be formally written from 2.27 and 2.28 as:

$$\frac{\partial^2 \sigma}{\partial \Omega \partial \omega_f} = Nr_0^2 \left(\frac{k_f}{k_i}\right) (\hat{\varepsilon}_f \cdot \hat{\varepsilon}_i) S(\mathbf{Q}, \omega). \quad (2.29)$$

This expression, however, has not the same physical meaning of 2.22. $S(Q, \omega)$ in 2.29 is, indeed, defined by the electronic coordinates so that it cannot be directly related to density fluctuations. Coming back to the definition of 2.14, one observes that

$$\langle e^{-i\mathbf{Q} \cdot \mathbf{R}_j(0)} e^{i\mathbf{Q} \cdot \mathbf{R}_{j'}(t)} \rangle = \sum_{|I\rangle} \langle I | e^{-i\mathbf{Q} \cdot \mathbf{R}_j(0)} e^{i\mathbf{Q} \cdot \mathbf{R}_{j'}(t)} | I \rangle, \quad (2.30)$$

where here $|I\rangle$ is an atomic quantum state. Within the validity of adiabatic approximation, it can be factorized into its electronic, $|I_e\rangle$, and nuclear, $|I_n\rangle$, part. Consequently:

$$\sum_{|I\rangle} \langle I | e^{-i\mathbf{Q} \cdot \mathbf{R}_j(0)} e^{i\mathbf{Q} \cdot \mathbf{R}_{j'}(t)} | I \rangle = f_j(\mathbf{Q}) f_j^*(\mathbf{Q}) \sum_{|I_n\rangle} \langle I_n | e^{-i\mathbf{Q} \cdot \tilde{\mathbf{R}}_j(0)} e^{i\mathbf{Q} \cdot \tilde{\mathbf{R}}_{j'}(t)} | I_n \rangle, \quad (2.31)$$

where

$$f_j(\mathbf{Q}) = \sum_{|I_e\rangle} P(E_I^e) \langle I_e | e^{i\mathbf{Q} \cdot \mathbf{u}_j} | I_e \rangle \quad (2.32)$$

If $|I_e\rangle$ coincides with the electronic ground state², 2.32 is the atomic form factor of the j^{th} atom. In 2.31 $\tilde{\mathbf{R}}_j$ is the nuclear coordinate, whereas in 2.32 \mathbf{u}_j is the coordinate of the j^{th} electron to respect the j^{th} atom, so that $\mathbf{R}_j = \tilde{\mathbf{R}}_j + \mathbf{u}_j$. From 2.31:

$$\frac{\partial^2 \sigma}{\partial \Omega \partial \omega_f} = N r_0^2 \left(\frac{k_f}{k_i} \right) (\hat{\varepsilon}_f \cdot \hat{\varepsilon}_i) \overline{|f(\mathbf{Q})|^2} S(\mathbf{Q}, \omega). \quad (2.33)$$

In the previous expression $S(\mathbf{Q}, \omega)$ is, now, the dynamic structure factor related to density fluctuations, i.e. the same quantity appearing in 2.22. The adiabatic approximation holds for exchanged energies smaller than the electron excitation energies. In this case the contribution to the total scattering coming from the valence electrons close to the Fermi level is small compared to the contribution coming from the core electrons. The difference between the initial and final state is, therefore, due to the excitations of the ion.

Summarizing, the following hypotheses have to be satisfied to ensure that the IXS spectrum provides a direct determination of the dynamical structure factor:

- the scattering process is dominated by the Thomson term;
- the center of mass of the electron cloud follows without delay the nuclear motion, i.e. the adiabatic approximation is valid;
- there are no electronic excitations in the considered energy transfer range.

2.1.3 INS vs IXS

In relation to the target system, it has been previously emphasized how INS and IXS carry the same physical informations. An analysis of the peculiar differences between them (related to the different nature of probe and probe-target interaction) points out the link between the experimental technique and the specific case that one want to study.

²it's assumed that the scattering event does not change the electronic wavefunctions

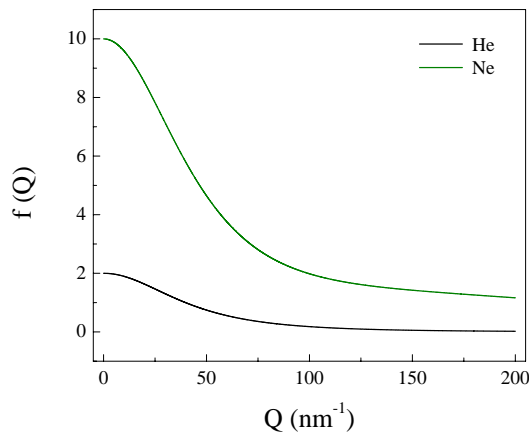


Figure 2.2: Form factor for Helium and Neon.

In the expression of the inelastic scattering cross section (eq. 2.13) the characteristics of the probe-target interaction are contained in the weight term $|\widehat{V}(\mathbf{Q})|^2$, i.e. $|b|^2$ or $|f(\mathbf{Q})|^2$ for Neutrons or X-Ray, respectively. The Q dependence of the X-Ray scattering weight, conversely to the Neutrons one, is explicitly shown. The atomic form factor $f(\mathbf{Q})$, indeed, decreases almost exponentially as Q increases. Its behavior is, in fact, determinate by the space Fourier transform of the various radial atomic wavefunctions of the electrons of the given atom, which are Legendre polynomials in the atomic limit. In fig. 2.2 is reported the atomic form factor of Helium and Neon, as obtained from [46]. Consequently, the IXS cross section strongly reduces at high Q . Due to the fact that neutrons interact with nuclei, no Q dependence of $|b|$ is expected up to $|Q|$ values of the order of the inverse of the nuclear size, i.e. up to Q values at least a factor 10^3 larger than in the X-Ray case. At $Q = 0$ the amplitude of $f(\mathbf{Q})$ is proportional to the number of electrons, Z . On the other hand, b depends on Z , A (the mass number) and \mathbf{J} (the total magnetic moment). It follows that the measured IXS signal always decreases low-

ering the atomic mass, whereas not a similar simple dependence can be found for the INS signal. Moreover, as consequence of the previously described dependence of the scattering strength, the INS signal (conversely to the IXS one) can be very different for different isotopes of the same material.

The strength ratio of incoherent to coherent contribution in the scattering cross section depends on the fluctuations of $\hat{V}_j(\mathbf{Q})$ to respect its atom independent average. In the INS case, remembering the quantities that define b_j , such fluctuations are generated not only by the presence of different isotopes, but also by different orientations between the neutron and nuclear spin, as happens in monoisotopic systems. This “sensitivity”, that is lack for IXS, leads to an high average deviation of b_j , i.e. to a significative incoherent contribution. For IXS (where $|f(\mathbf{Q})|$ essentially depends only by Z) such a contribution is negligible.

A substantial difference from a neutron probe and a photon one is enclosed in the relations 2.17 and 2.23: only neutrons are massive particles. Moreover, the characteristic energies of thermal neutrons ($E_n \sim 10 \div 100 \text{ meV}$) are very far from these of X-Ray ($E_x \sim 1 \text{ keV}$) and comparable with the energy of typical inelastic excitations. These peculiarities strongly influence the dynamical range accessible by INS or IXS. This latter is defined as the set of (Q, ω) values for which the scattering process is allowed. It can be derived using the general conservation laws (eqs. 2.2) and 2.17 or 2.23. For INS and IXS it’s, respectively, found:

$$\frac{Q^2}{k_i^2} = 2 - \frac{2m(\hbar\omega)}{\hbar^2 k_i^2} + 2 \cos(2\theta) \sqrt{1 - \frac{2m(\hbar\omega)}{\hbar^2 k_i^2}} \quad (2.34)$$

$$Q = k_i \left[\left(\frac{\mathbf{k}_f}{k_f} \right) \frac{(\omega + \omega_i)}{\omega_i} - \left(\frac{\mathbf{k}_i}{k_i} \right) \right], \quad (2.35)$$

where 2θ is the scattering angle defined in fig.2.1. In the limit $\omega \ll \omega_i$ 2.35 becomes:

$$Q = 2k_i \sin(2\theta/2), \quad (2.36)$$

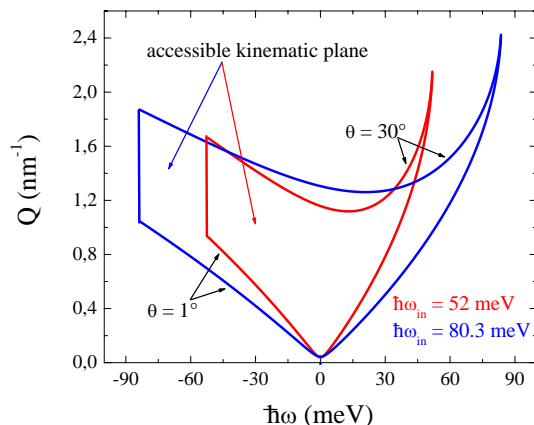


Figure 2.3: Dynamical range for neutrons at typical initial energies.

i.e. for IXS Q is entirely determined by the scattering angle: there are not kinematic limitation to the exchanged energy that can be detected for a given modulus of the exchanged momentum. For INS, as it is evident in 2.34, the momentum transfer is also determined by the energy transfer. In fig. 2.3 eq. 2.34 is plotted in the (Q, ω) plane at different values of the scattering angle. As it appears, there are kinematic regions not accessible for any scattering angle. In these regions there are, for example, the dispersion relation of acoustic excitations that propagate with a sound speed larger than the one of the incident neutrons, typically higher than ~ 1100 m/s for thermal neutrons. The limitation imposed by dynamical range are particularly restraining for amorphous materials. In crystals, in fact, the kinematic limitation can be overcome studying the collective excitations in Brillouin zones higher than the first. This is not possible, obviously, for disordered systems, due to the lack of translational invariance. The only way to study low-energy excitations, in this case, is to enlarge the dynamical range increasing the energy of the incident neutrons (at the expense of the energy resolution). On the other side, the study of low-energy excitations is strongly influenced by the shape of the energy

resolution, as well as its absolute value. For INS this shape is a Gaussian, while for IXS it is close to a Lorentzian. The high tails of the Lorentzian shape represent a strong disadvantage for resolving the fine details of the dynamic structure factor. In particular, for low energy features the contrast is lower than the most favorable Gaussian shape of the INS resolution function. The last observation concerns the flux of neutrons/phonons needed to perform an INS/IXS experiment. Because $E_n \sim \omega \sim meV$ a moderate energy resolution ($\Delta E/E \sim 10^{-2}$) is sufficient to determine the dynamical structure factor in the meV range, where these excitations fall. Conversely, $E_x \gg \omega$ and a much higher energy resolution ($\Delta E/E \sim 10^{-7}$) is needed in order to resolve the same excitations. This leads to a substantial reduction of the photon flux.

In INS/IXS experiments, in order to derive the actual count rate, the total scattering volume has to be considered. Taking into account absorption processes, the flux of scattered particles per unit solid angle and energy interval is:

$$N = N_0 \frac{\partial^2 \sigma}{\partial \Omega \partial \omega} n L e^{-\mu L}, \quad (2.37)$$

where μ is the total absorption coefficient and L the sample length. The largest value for N is obtained for $L = 1/\mu$. For this reason, the sample length has to be chosen in order to satisfied this condition. For IXS (considering energies $\sim 20 KeV$ and $Z > 3$), μ is mainly due to photoelectric absorbtion process. This imply $\mu(IXS) \propto Z^4$ when the incident energy is far from absorbtion thresholds. The scattering cross section increases as Z^2 (see subsec. 2.1.2). Fixed $L = 1/\mu$, the flux N is proportional to $1/\mu$. With these considerations, from 2.37 it's possible to deduce that $N \propto 1/Z^2$. So, the scattering volume of high Z materials is strongly reduced. Also for INS it's possible to define the best sample length, with the same considerations mode for IXS. But this is not enough. In fact, the absorption is dominated by the scattering processes. The inelastic signal, therefore, has always a large contribution from multiple scattering. In order to reduce the background

generated from these multiple scattering events, the thickness of the sample has to be reduced. However, in particular increasing the neutrons incident energy, such a contribution cannot be neglected and suitable calculations are needed to isolate it from the more interesting parts of the signal, related to single scattering process.

2.2 Inelastic scattering from a binary mixture

The generalization of the foregoing formalism to binary systems is straightforward. If 1 and 2 indicate the two specie components of a binary mixture, the total cross section for a scattering process (2.12) is

$$\frac{\partial^2 \sigma}{\partial \Omega \partial \omega_f} = \frac{1}{N_i} \frac{\partial^2 n}{\partial \Omega \partial \omega_f} \frac{2\pi}{\hbar} \int_{-\infty}^{\infty} dt e^{-i\omega t} \sum_{\alpha, \beta=1,2} \sum_{j, j'} \overline{\hat{V}_{j(\alpha)} + (\mathbf{Q}) \hat{V}_{j'(\beta)}(\mathbf{Q})} \langle e^{-i\mathbf{Q} \cdot \hat{\mathbf{R}}_{j\alpha}(0)} e^{i\mathbf{Q} \cdot \hat{\mathbf{R}}_{j'\beta}(t)} \rangle. \quad (2.38)$$

If, for a given specie α , the interaction potential $\hat{V}_{j(\alpha)}$ is independent of j , it reduces to

$$\frac{\partial^2 \sigma}{\partial \Omega \partial \omega_f} = \frac{1}{N_i} \frac{\partial^2 n}{\partial \Omega \partial \omega_f} (2\pi)^2 N \sum_{\alpha, \beta=1,2} (x_\alpha x_\beta)^{1/2} \overline{\hat{V}^{\alpha\beta}(\mathbf{Q})}^2 S^{\alpha\beta}. \quad (2.39)$$

Because the weight term $|\hat{V}^{\alpha\beta}(\mathbf{Q})|^2$ is inside the summation in 2.39, it's not possible, in a single measurement, to separate the terms describing the probe-target interaction from these related to the intrinsic properties of the system (i.e. the partial dynamic structure factors). If, by performing three different experiments ((a), (b), (c)), it's possible to change the weight terms $|\hat{V}^{\alpha\beta}(\mathbf{Q})|^2$, the partial dynamic structure factors can be extrapolated solving the system:

$$\begin{pmatrix} \frac{\partial^2 \sigma}{\partial \Omega \partial \omega_f}^{(a)} \\ \frac{\partial^2 \sigma}{\partial \Omega \partial \omega_f}^{(b)} \\ \frac{\partial^2 \sigma}{\partial \Omega \partial \omega_f}^{(c)} \end{pmatrix} \propto \begin{pmatrix} \frac{\partial^2 n}{\partial \Omega \partial \omega_f}^{(a)} |\hat{V}^{11}|^2^{(a)} & 2 \frac{\partial^2 n}{\partial \Omega \partial \omega_f}^{(a)} |\hat{V}^{12}|^2^{(a)} & \frac{\partial^2 n}{\partial \Omega \partial \omega_f}^{(a)} |\hat{V}^{22}|^2^{(a)} \\ \frac{\partial^2 n}{\partial \Omega \partial \omega_f}^{(b)} |\hat{V}^{11}|^2^{(b)} & 2 \frac{\partial^2 n}{\partial \Omega \partial \omega_f}^{(b)} |\hat{V}^{12}|^2^{(b)} & \frac{\partial^2 n}{\partial \Omega \partial \omega_f}^{(b)} |\hat{V}^{22}|^2^{(b)} \\ \frac{\partial^2 n}{\partial \Omega \partial \omega_f}^{(c)} |\hat{V}^{11}|^2^{(c)} & 2 \frac{\partial^2 n}{\partial \Omega \partial \omega_f}^{(c)} |\hat{V}^{12}|^2^{(c)} & \frac{\partial^2 n}{\partial \Omega \partial \omega_f}^{(c)} |\hat{V}^{22}|^2^{(c)} \end{pmatrix} \begin{pmatrix} S^{11} \\ S^{12} \\ S^{22} \end{pmatrix}. \quad (2.40)$$

This kind of experiments are usually performed by isotopic substitution of the two mixture components.

It is evident from 1.22 that the total scattering can be equivalently represented by a linear combination of the partial dynamic structure factors $S^{\gamma\delta}$, $\gamma = n$, $\delta = c$, considering that the weight terms have to be suitably changed.

2.3 IXS spectrometer: beamline ID-28 at ESRF

The IXS beamline ID-28 at the European Synchrotron Radiation Facility (ESRF) in Grenoble [47] is briefly described in the following.

The instrument is based on the principle of triple axis spectrometry. The first axis is defined by the monochromator crystal whose function is to monochromatise the beam using a Bragg reflection. The second axis corresponds to the scattering sample. It determines the scattering angle and, consequently, the momentum transfer Q (see sec. 2.1). The third axis is defined by the analyzer crystal. It determines the energy of the scattered photons exploiting, as the first axis, the principle of the Bragg reflection. As emphasized in subsec. 2.1.3 to perform an IXS experiment very high energy resolution and efficiency are required. These two conditions can be obtained with the use of high order reflections in perfect crystals and the use of a backscattering geometry to maximize the angular acceptance of the crystal reflection. As a consequence of the extreme backscattering geometry, the energy difference between analyzer and monochromator cannot be varied modifying the Bragg angle of one of the two crystals, as it is usually done in triple axis instruments. The energy scans are therefore performed by changing the relative temperature of the monochromator. This, in fact, allows to keep constant the geometrical contributions to the total instrumental resolving power.

The instrument layout is reported in fig. 2.4. The X-ray source consists of three undulators of 32 *mm* magnetic period. The utilized X-ray radiation energies

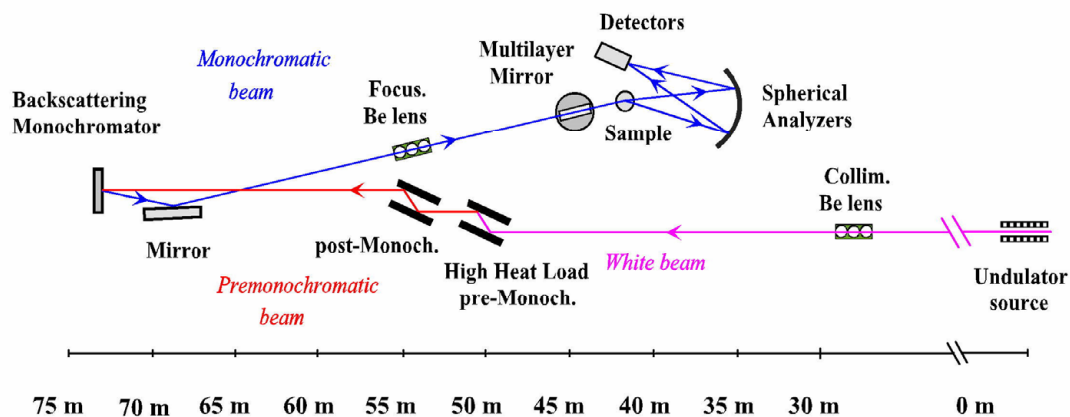


Figure 2.4: Schematic layout of ID-28 spectrometer.

correspond to the undulator emission of the 3rd and 5th harmonics. The X-ray beam has a $40 \times 15 \mu\text{Rad}$ (FWHM, horizontal \times vertical) angular divergence, a spectral bandwidth $\Delta E/E \sim 10^{-2}$, and an integrated power within this divergence of the order of 200 W.

The X-ray beam coming from the undulators is pre-monochromatized using a $\text{Si}(1,1,1)$ double crystal. The bandwidth is, in this way, reduced to $\Delta E/E \sim 2 \cdot 10^{-4}$. The principal scope of this state is to reduce the heat load impinging on the monochromator. The thermal deformation of the monochromator crystal generated by the heat load could, in fact, deteriorate the energy resolution below acceptable values.

The photons from the pre-monochromator impinge onto the high energy resolution monochromator. This is a silicon crystal oriented along the [111] direction and operating at a Bragg angle of 89.98° . The required energy resolution to study collective excitations in condensed matter physics by IXS is $\Delta E/E \sim 10^{-7} \div 10^{-8}$ (subsec. 2.1.3). As previously anticipated this requirement is satisfied by using high order reflections together with extreme backscattering geometry. The rea-

sons of these choices are briefly analyzed. Considering Bragg diffraction from a perfect crystal of lattice spacing a , the best energy resolution $(\Delta E/E)_{\mathbf{Q}_h}$ at a given diffraction order $\mathbf{Q}_h = \frac{2\pi}{a}(h, k, l)$ can be derived in the framework of the Dynamical Theory of X-ray diffraction [48]. This is found to be directly proportional to the atomic form factor calculated in \mathbf{Q}_h , $f(\mathbf{Q}_h)$. As general trend, $f(\mathbf{Q}_h)$ decreases with increasing \mathbf{Q}_h . This results can be more easily interpreted emphasizing how the atomic form factor is related to the penetration length, L_p , of the photons beam inside the crystal. In fact, $f(\mathbf{Q}_h)$ can be seen as the reflection coefficient of the electric field and L_p is limited by the fact that each plane involved in the reflection reduces the incident intensity on the following plane. This relation can be, as well, quantified by using the conventional dynamical theory founding that $L_p \propto f(\mathbf{Q}_h)$. The number of planes involved in a reflection, which play the role of the lines in a bi-dimensional grating, are then inversely proportional to $f(\mathbf{Q}_h)$. In the same way as for gratings used to monochromatise visible light (for which the resolving power is proportional to the number of lines of the grating), increasing resolving power is obtained with increasing reflection order. The penetration length of the beam inside the crystal can, moreover, be reduced by the photoelectric absorption. At sufficiently large \mathbf{Q}_h such an absorption can reduce the photons penetration length inside the crystal to value lower than L_p , i.e. it starts to be larger than the scattering length needed to monochromatise the photon beam to the theoretical value $(\Delta E/E)_{\mathbf{Q}_h}$. There is, therefore, for the desired value of $(\Delta E/E)_{\mathbf{Q}_h}$ a maximum possible diffraction order, $\mathbf{Q}_h(max)$. In the case of silicon it is found that $\mathbf{Q}_h(max) = 300 \text{ nm}^{-1}$ [49]. The diffraction order that fulfilled all the previous requirement correspond, for silicon, to the reflections (h, h, h) with $h = 7, 8, 9, 10, 11, 12, 13$ [50]. The intrinsic energy resolution ΔE at the given diffraction order can be deteriorated by geometrical effects related to the finite angular divergence of the incident beam. In the present case such a

divergence is estimated to be of the order $10 - 100 \mu\text{Rad}$. The effective energy resolution related to it, $(\Delta E/E)_g$, can be obtained by differentiating the Bragg law to respect the angle of incidence. Consequently, $(\Delta E/E)_g$ depends on the Bragg angle, whereas the intrinsic resolution $(\Delta E/E)_{\mathbf{Q}_h}$ does not. It follows that not all the Bragg angles fulfill the condition $(\Delta E/E)_g < (\Delta E/E)_{\mathbf{Q}_h}$. In particular, for the needed value of $(\Delta E/E)_{\mathbf{Q}_h}$, only the extreme backscattering geometry ensures that.

A platinum coated toroidal mirror, located at 25 m from the sample, focuses the monochromatic beam in both the vertical and horizontal plane. It provides a focus at the sample position of $250 \times 80 \mu\text{m}^2$. More performing optics are available to focus the beam down to $30 \times 40 \mu\text{m}^2$.

The X-ray radiation scattered from the sample is analyzed in energy. The problems connected to the energy resolution are conceptually the same for the monochromator and the analyzer. The factors determining the angular acceptance for the analyzer are, however, very different to respect these for the monochromator. Only in the former case they are, in fact, dictated by the desired momentum resolution, ΔQ . Considering value of ΔQ in the range $0.1 - 0.5 \text{ nm}^{-1}$, the corresponding angular acceptance of the analyzer crystal must be $\sim 10 \text{ mrad}$, a value much larger than the spectral angular acceptance (so-called Darwin width) related to the intrinsic energy resolution. The only way to obtain such a large angular acceptance is the use of a focusing system which, nevertheless, has to preserve the perfect crystal properties necessary to obtain the desired energy resolution. This constrain excludes the possibility to consider elastically bent crystals. A solution to circumvent elastic deformations is to position small flat crystals, squares of side length c , on a focusing substrate of radius R , with $c \ll R$. Providing that this focusing element is a sphere in 1:1 Rowland geometry, the Bragg angle variation on anyone of these small crystals will be c/R . This ratio can be choose to be smaller

h	Energy [keV]	ΔE [meV]	Q_{max} [nm ⁻¹]	Q_{min} [nm ⁻¹]	ΔQ [nm ⁻¹]	Flux [photons/s/200mA]
7	13.840	7.6 ± 0.2	64	1	1.89	$1.5 \cdot 10^{11}$
8	15.817	5.5 ± 0.2	74	1	2.16	$9.0 \cdot 10^{10}$
9	17.794	3.0 ± 0.2	83	1	2.43	$2.7 \cdot 10^{10}$
11	21.747	1.5 ± 0.1	101	1	3.00	$6.6 \cdot 10^9$
12	23.725	1.3 ± 0.1	111	1	3.24	$5.9 \cdot 10^9$
13	25.704	1.0 ± 0.1	120	1	3.50	$1.5 \cdot 10^9$

Table 2.1: Main characteristics of the ID-28 spectrometer, for the different $Si(h, h, h)$ reflections. Energy indicates the incident photon energy, ΔE is the total energy resolution, Q_{min} and Q_{max} indicate the minimum and maximum momentum transfers and ΔQ indicates the Q-spacing between adjacent analyzers. The photon flux values are measured at the sample position.

then the Darwin width so that its effect on the energy resolution is negligible. The analyzer consists of 12000 silicon perfect single crystals with $c = 0.6 \text{ mm}$ and a thickness of 3 mm . The radius, of the substrate is equal to the spectrometer arm ($R \sim 7 \text{ m}$) [51, 52]. The spectrometer furthermore consists of entrance motorized slits in front of the analyzer crystal to set the desired momentum resolution and a detector. The detector is an ensemble of Peltier cooled silicon diodes of 1.5 mm thickness with an active area of $2 \times 12 \text{ mm}^2$, inclined at 20° in order to enhance the X-ray absorption. The scattering angle between the sample and the analyzer can be changed from 0° to 55° in order to change the momentum transfer Q (e.g. corresponding to a Q -range between 1 and 100 nm^{-1} in the $Si(11, 11, 11)$ configuration). On $ID - 28$, moreover, there are nine independent analyzers with a fixed angular offset among themselves of $\sim 0.75^\circ$, mounted on the 7 m long arm that can rotate around a vertical axis passing through the scattering sample. This allows to record 9 IXS spectra in one only shot, with a nearly constant offset between them. The main characteristics of the spectrometer are summarized in tab. 2.1.

As clear from the previous considerations, the monochromator or analyzer Bragg angle is determined by the desired energy resolution. It's not possible,

therefore, to perform energy scans by changing such an angle. To circumvent this difficulty, energy scans can be performed by varying the temperature of one of the two crystals, which results into a relative change of the lattice parameter, a . This variation is given by $\Delta a/a = \alpha \Delta T$, where α is the coefficient of thermal expansion, and ΔT is the temperature difference between the two crystals. In Silicon at 294 K, $\alpha = 2.56 \cdot 10^{-6} K^{-1}$. To obtain a resolving power $\Delta E/E \sim 10^{-7} - 10^{-8}$, the temperature of the two crystals has to be controlled with mK precision. This task is achieved by a carefully designed temperature bath, controlled by an active feedback system [50], which assure a temperature control of 0.2 mK at around 295 K. In order to convert the temperature scale into the energy scale, a precise expression for $\alpha(T)$ has to be given. Recent results show that:

$$\alpha(T) = \alpha_0 + \beta \Delta T \quad (2.41)$$

with

$$\alpha_0 = 2.581 \pm 0.002 \cdot 10^{-6} K^{-1}; \quad \beta = 0.016 \pm 0.004 \cdot 10^{-6} K^{-2}; \quad \Delta T = T - 22.5^\circ C.$$

From 2.41 it follows:

$$\Delta E/E = -\Delta d/d = \int_{T_0}^T \alpha_0 + \beta(T' - T_0) dT' = (\alpha_0 - \beta T_0) \Delta T + \frac{1}{2} \beta (T^2 - T_0^2). \quad (2.42)$$

2.4 INS spectrometer: BRISP at ILL

The neutron BRillouin scattering SPectrometer (BRISP) is built at the High Flux Reactor (HFR) of the Institut Laue Langevin (ILL) in Grenoble. It is a new type of Time-of-Flight (ToF) spectrometer adapted to well resolved neutron inelastic scattering at small angles in the thermal region. The aim of this instrument is to explore, by means of INS, the low momentum transfer in disordered matter with a sufficiently high counts rate. These region is, in fact, not accessible for conventional

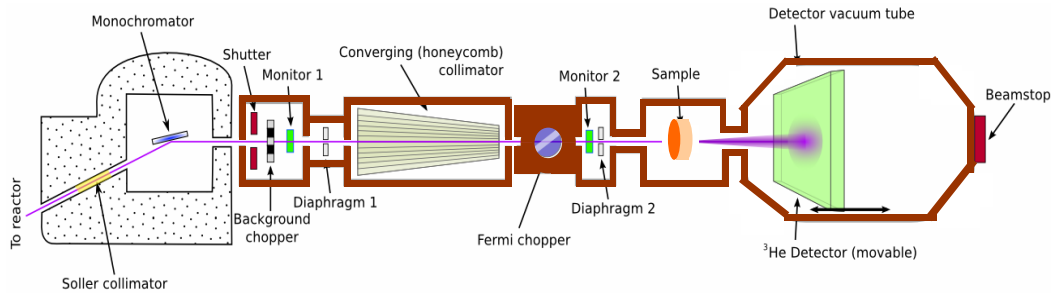


Figure 2.5: Schematic layout of BRISP spectrometer.

ToF spectrometers due to kinematic limitations (see subsec. 2.1.3) associated to the usually employed low energy of the incoming neutrons. On the other hand, IXS can be inhibited in the detection of the low-energy excitations present at low momentum transfer by the less favorable shape of the resolution function. The most straightforward way to explore such a region is, therefore, the use of INS triple axis spectrometers. However, the limit of these instruments is intrinsic in the way the cross section is measured. The point-by-point measurement is, indeed, very appropriate for a surgical cut of the reciprocal space but very time consuming for the study of an extended region in energy-momentum space, particularly in the case of disordered (isotropic) system where such a cut is usually redundant. The working principle of BRISP is based, essentially on

- a hybrid spectrometer configuration (a crystal-monochromator fixes the incident neutron energy and a Fermi chopper system defines the neutron final energy by ToF analysis),
- an optimized two-dimensional small-angle detector.

The layout of the instrument is shown in fig. 2.5. The thermal neutrons beam coming from HFR has an inclination of 35° . It provides a peak intensity of 4.5×10^9

$cm^{-2}s^{-1}$ over a circular area of 6 cm diameter at the exit of the in-pile collimator. The beam is then collimated by a standard Soller collimator (0.4° divergence).

The neutrons beam illuminates a $20 \times 8 \text{ cm}^2$ monochromator composed of 5×4 crystals, each having a surface of $4 \times 2 \text{ cm}^2$. As the monochromated beam has to be horizontal, considering the 35° inclination of the incoming beam on the monochromator, the reflection angle between the crystal planes and the neutron beam is fixed to $\theta_B = 17.5^\circ$. To enable a change of the incident neutron wavelength three different sets of crystals are available: pyrolytic graphite, exploiting either $(0, 0, 2)$ or $(0, 0, 4)$ reflections, and a *Cu* crystal in $(1, 1, 1)$ reflection. They produces, respectively, incident neutrons at the energies: 20.9 meV, 83.7 meV and 54.1 meV. Due to the fixed monochromator angle, an almost constant relative energy resolution $\Delta E/E \sim 0.025$ is provided in the restricted *Q*-region covered. After the reflection, the projection area of the neutron beam is $6 \times 6 \text{ cm}^2$. The monochromator has, moreover, an adjustable curvature in the plane perpendicular to the diffraction plane that, together with the secondary collimator, guarantees a well-focused neutron spot on the detector.

A disk chopper, placed immediately after the monochromator, with eight rectangular windows and rotating at a maximum frequency of 5000 rpm, produces broad neutron pulses. This device ensures a reduction of the background of the continuous beam and, by a proper phasing with the Fermi chopper, minimizes contamination by other-order reflections of the monochromator.

The neutrons beam passes, then, through a second collimator. The geometry and the imperfections of the monochromator lead to an angular divergence of the reflected neutron beam and a spread of the wavevector magnitude distribution. In fact, it follows from the Bragg's law that the selected wavenumber is $k_i = \pi/(d \sin \theta_B)$. Its uncertainty ($dk_i = k_i \cot \theta d\theta_B$) is, consequently, relatively large due to the large cotangent value at the selected θ_B , fixed by the previously

described geometrical condition. The role of such a second collimator is to minimize these effects and to focalize the neutron beam on the detector. It is based on the focusing multi-beam concept [53] and equipped with a specially developed honeycomb design [54]. This is a two-dimensional converging device that splits the monochromatic beam into several collimated (0.4° divergence) partial beams of decreasing hexagonal cross section and converging at the detector position. This solution has the important advantage of simultaneous convergence and collimation in both the vertical and the horizontal scattering plane, as required for a two-dimensional detector. In order to adapt the beam convergence to different positions of the detector, three honeycomb collimators are available, optimized for a sample-to-detector distance of 2, 4 and 6 *m*.

A fast rotating (maximum angular velocity 15.000 *rpm*) Fermi chopper is, then, used to produce the short neutron pulses needed to provide the time-reference for the ToF analysis.

The high-vacuum sample chamber (50 cm diameter) is separated by 1 *mm* aluminum windows from the rest of the vacuum line. The scattered neutrons are, finally, collected by means of a wide-area highly pixelled ^3He two-dimensional detector. The detector is composed of an array of 96 ^3He tubes 1 *m* long and with 0.5 *m* of inner diameter, with a ^3He pressure of 15 *bar*. It is mounted on a translation stage inside a long vacuum chamber (2.5 *m* diameter, 8 *m* length), for collection at any desired position between 1.5 and 6 *m* from the sample. The spatial resolution achievable is 1.3 cm horizontally (due to tube distance) and 1.1 *cm* vertically. In small-angle instruments, the angular range, $\Delta\theta$, of the scattered neutrons is typically determined by the sample-to-detector distance, the size of the detector, and the size of the beam-stop, which protects the detector from damage by the direct beam. At a given detector distance, the beam-stop size determines the lowest scattering angle, while the detector size the highest one. By the BRISP

characteristics it's possible to estimate $\Delta\theta = [0.4^\circ - 7^\circ], [0.6^\circ - 12.5^\circ], [2^\circ - 20^\circ]$ at the sample-detector distances of 2, 4 and 6 m , respectively.

As for all direct geometry ToF spectrometers, each time channel of the detector at a given scattering angle θ can be associated with a value of the final neutron energy E_1 . Once known the distance between the Fermi chopper and the sample, L_0 , the distance between the sample and the detector, L_1 , the following expressions for the neutron time of flight, t_{OF} , and the neutrons incident energy, E_1 can be deduced:

$$t_{OF} = \frac{L_0}{v_0} + \frac{L_1}{v_1}$$

$$E_1 = \frac{1}{2}M_n v_1^2 = \frac{1}{2}M_n \left(\frac{L_1}{t_{OF} - L_0/v_0} \right)^2 = \frac{1}{2}M_n \left(\frac{L_1}{t_{OF} - \sqrt{M_n/(2E_0)}} \right)^2, \quad (2.43)$$

where v_0 and v_1 are the neutron velocities before and after the scattering event. Since E_0 is fixed, each value of the scattered energy E_1 corresponds to a defined energy transfer $\hbar\omega = E_0 - E_1$. The ToF analysis of the neutrons collected at a given scattering angle thus provides an entire spectrum $I_\theta(E)$ at once. The exchanged wavevector Q can be determined by the relation 2.34. The kinematic regions probed at two different incident energies of BRISP are reported in fig. 2.3. The Q resolution can be evaluated by considering the uncertainties in both incident and final neutron wavevectors, and in scattering angle. The combination of all the above uncertainties gives rise to an overall wavevector transfer resolution of about 0.2 and 0.5 nm^{-1} at the lowest and highest BRISP incident energy, respectively.

Tab. 2.2 summarizes the technical characteristics of BRISP.

2.5 Experimental setup

The experiments performed can be devised into two category: 1) IXS measurements on the neutral fluid mixture He/Ne at different thermodynamic condition

E_0 (MeV)	D_{sd} (m)	Energy Transfer E (MeV)	Angular and Q -range(\AA^{-1})		Resolution	
					$\Delta E/E_0$	ΔQ (\AA^{-1})
20.9	2	± 18	$1^\circ - 15^\circ$	0.05 - 0.8	3%	0.02
	4	± 14	$1^\circ - 15^\circ$	0.05 - 0.8	2.9%	
	6	± 12	$1^\circ - 9^\circ$	0.05 - 0.5	2.4%	
49.9	2	± 50	$1^\circ - 15^\circ$	0.09 - 1.3	3.8%	0.03
	4	± 45	$1^\circ - 15^\circ$	0.09 - 1.3	3%	
	6	± 35	$1^\circ - 9^\circ$	0.09 - 0.8	2.7%	
83.6	2	± 80	$1^\circ - 15^\circ$	0.1 - 1.7	4.5%	0.04
	4	± 70	$1^\circ - 15^\circ$	0.1 - 1.7	3.2%	
	6	± 60	$1^\circ - 9^\circ$	0.1 - 1.0	3.1%	

Table 2.2: Energy parameters and resolutions of BRISP spectrometer.

in the mesoscopic/single particle Q -region and, 2) INS measurements on molten salt RbF (at a temperature T just above the melting temperature) at the transition from hydrodynamic to mesoscopic region. The experimental demands are, in the two case, very different. In the first case a large volume pressure cell (LVC) is needed (see fig. 2.6), as motivated by the two following considerations:

- LCV is very versatile since, even if this cannot reach very high pressures, this can work in a very large temperature range and pressure (i.e. 270 – 800 K and 1 – 3000 bar). This characteristic is well suited for the experiment on He/Ne mixture, where the study has to be done at different thermodynamic points.
- LVC allows the optimization of the sample volume and the scattering angle. This permits to maximize the IXS signal and to optimize the maximum momentum transfer experimentally accessible, Q_{max} , which, for the present experiments, is limited by the maximum scattering angle defined by LVC. In the present case in the thermodynamic point ($T = 184 K$, $P = 408 bar$) it was possible to joint a Q_{max} value of $52 nm^{-1}$ for a maximum scattering angle, $\theta_{max} = 6.8^\circ$, as defined by the geometry of the LCV, and in the $Si(11, 11, 11)$ configuration of the IXS spectrometer. This angle is defined by the cell length (12 mm), the windows diameter (6 mm), the angular acceptance of the conical windows support (30°), the length of the circular

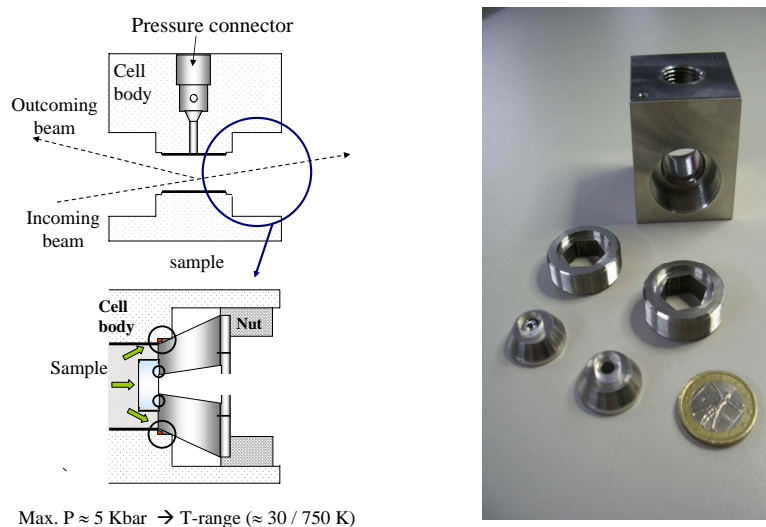


Figure 2.6: High-pressure cell used to study supercritical *He* and *He/Ne* mixtures.

nut ($\sim 1\text{cm}$) (for details see fig. 2.6) and, finally, by the IXS cross section of the sample which, through the volume scattering, defines the effective sample length at which the IXS signal is significantly different from zero.

In the second case a high-temperature, corrosion resistant cell is needed. These characteristics can be satisfied by the electron beam welded Nb cell depicted in fig. 2.7, and described in the following subsection.

2.5.1 The high-pressure cell

A schematic drawing of the high-pressure cell is reported in fig. 2.6. Its main characteristics are the long sample length (12 mm) and the angular acceptance of 30 degrees, which allows to reach high exchanged momenta. The cell can be connected to the external HP apparatus though a standard Nova Swiss HP connection. The two diamond windows, through which pass both the incident and the scattered

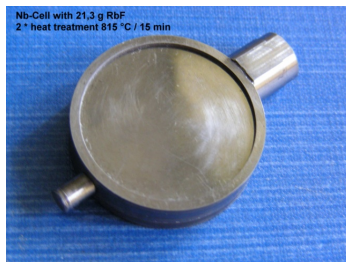


Figure 2.7: High-temperature and corrosion resistant Nb cell used to study molten RbF.

beam, are single crystal diamond disks of 6 mm of diameter and 1 mm thickness. Besides their resistance to mechanical solicitations, a decisive advantage using diamond windows is their negligible contribution to the scattered intensity. Diamonds are glued on the flat internal face of the two conical supports. A special attention has to be given in the choice of the appropriate glue and the gluing procedure. For the low temperature studies an epoxy resin (Epotech 301) was used as glue. Both the window and the glued surface have been previously mirror-polished, $< 5\ \mu\text{m}$ roughness (*rms*), with diamond powder. The diameter of the hole (2.3 mm) at the flat surface of the support, which allows the beam to pass through the chamber, was chosen as the best compromise between the angular opening and the unsupported area of the windows. The supports are screwed and tightened against the cell body by special circular nuts. Two brass or copper ring gaskets with triangular section are pushed, by the pressure medium itself, as an anvil into the inner space between the conical surface of the supports and the inner wall of the internal chamber. The HP tightness is accomplished by this double metal to metal contact (conical supports and internal chamber). A couple of viton O-rings were used together to seal the cell at low pressure. In fact, while at high pressures the compression medium pushed the metallic gasket ensuring the tightness, the O-rings are used as a spring, which pushes the gaskets from the back, allowing the

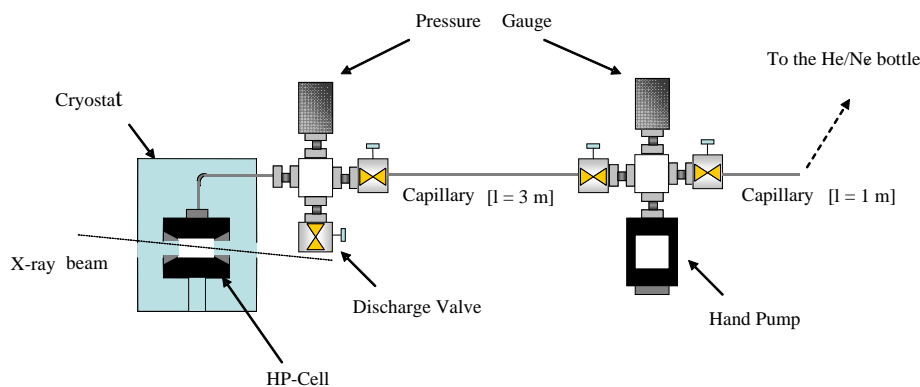


Figure 2.8: Schematic draw of the low temperature HP apparatus.

tightness also at low pressure.

2.5.2 Low temperature assembly for *He/Ne* mixture

For the study of *He/Ne* mixtures, the pressure cell was mounted in thermal contact with a cold finger of an *AL125* close-cycle helium cryostat. This system allows exploring a wide region of the $P - T$ plane: from $\sim 20 K$ up to room temperature, and from a few bar up to $\sim 3 Kbar$.

Thin indium foils were used for all thermal interfaces in order to maximize the thermal contact. The temperature of the cell was changed by using a heating resistor placed between the pressure cell and the cryostat cold finger. The temperature is monitored by two silicon diode thermometers mounted on the cell, with a precision of $\pm 0.5 K$. The pressure cell and the cryostat cold finger are kept under high vacuum ($\sim 10^{-8} mbar$). The assembly is schematically reported in fig. 2.8.

2.5.3 The high-temperature Nb cell

In fig. 2.7 a picture of the *Nb* cell exploited for the INS experiment on molten *RbF* is reported. It is a cylinder of $36 mm$ inner diameter, $39 mm$ external diameter

and 8 *mm* height. The neutron flux goes through the cylinder basis. Niobium is high-corrosion and high-temperature resistant (melting point 2750 *K*) material. Its characteristics are, then, ideal to overcome the challenge of experiment on molten salt. However, because its neutron scattering cross section is not negligible ($b_{Nb} = 6.255 \text{ barn}$) one has to care that 1) the thickness of cell walls illuminated from the neutron flux is enough small and, 2) the sample chosen has a small absorption cross section so that the contribution of the empty cell to the measured spectra is not too big. In the present experiment on molten *RbF* a wall thickness of 0.2 *mm* was chosen as best compromise between fulfilling conditions 1) and 2) and mechanical stability of the cell. The cell is electron-beam welded in vacuum after it was filled with *RbF* powder in controlled atmosphere. This procedure assures that any contamination is present inside the cell, considering that *RbF* is hygroscopic. They, in fact, could break down the corrosion resistance of the *Nb*. The electron beam welding, moreover, assures high temperature resistance, getting around the use of glue.

The Helium/Neon mixtures from the mesoscopic to the single particle regimes

In this chapter we will present and discuss the results obtained by Inelastic X-ray Scattering (IXS) spectroscopy on the prototype binary mixture $He_{0.8}Ne_{0.2}$. The chosen sample was investigated in wide range of momentum transfer (Q) values, including both the mesoscopic ($Q = 5 \div 30 \text{ nm}^{-1}$) and Impulsive Approximation ($Q = 30 \div 50 \text{ nm}^{-1}$) regimes.

3.1 The IXS experiment

The experiment was performed at the ID28 beamline of the European Synchrotron Radiation Facility (Grenoble, France). The spectrometer was operated at the Si(11,11,11) configuration, which correspond to an overall energy resolution of about 1.5 meV . In the subsequent section we will also describe the procedure used for determining the lineshape of the experimental energy resolution function. The actual configuration of ID28 IXS spectrometer allow simultaneously measuring the energy transfer (E) dependence of a set of 9 IXS spectra at different Q -values separated by a constant Q -offset of about 1.5 nm^{-1} . The chosen E -range was quite large ($\pm 50 \text{ meV}$), the E -sampling steps quite narrow ($\approx 0.3 \text{ meV}$) and

3. The Helium/Neon mixtures from the mesoscopic to the single particle regimes

the acquisition time for a each E -point quite long (a few minutes) in order to obtain high quality and high statistics data for performing the lineshape analysis described further below. The actual Q -values of IXS spectra were experimentally chosen by varying the angle of the spectrometer arm from, approximatively, 5 to 20 degrees. The momentum resolution (ΔQ) was set by the aperture of the analyzer slits, which determines the momentum resolution. For the low- Q measurements (mesoscopic regime) a ΔQ -value of 0.3 nm^{-1} was chosen, while for high- Q data we decided to completely open the analyzer slits, thus increasing the count rate by relaxing ΔQ down to 1 nm^{-1} . Indeed, a better Q resolution is not needed at high- Q , while we needed to compensate for the rather strong reduction in the intensity of scattered signal due to: (i) the high- Q decrease of form factor, $f(Q)$, (ii) the decrease of the polarization factor at large scattering angle (the synchrotron radiation is polarized in the scattering plane) and (iii) the decrease in the deep of field of the spectrometer at high angles. For further details on the employed IXS spectrometer see also sec. 2.3

The high purity $He_{0.8}Ne_{0.2}$ sample (Gas Liquide) was embedded in the high pressure hydrostatic cell described in subsec. 2.5.1. The cell was connected to an external high pressure generator through a capillary and monitored by a pressure gauge with a precision of $\pm 5 \text{ bar}$. No long time drift of chosen sample pressure was observed during the typical acquisition time ($12 \div 18$ hours) for a single set of 9 IXS spectra. IXS spectra of $He_{0.8}Ne_{0.2}$ were collected at three different temperatures (33, 82 and 184 K), corresponding to a sample number density of 34.4, 18.5 and 12.2 nm^{-3} , respectively. This range spans from liquid-like to gas-like densities. In order to probe such a temperature range we used a close-cycle He cryostat temperature and a resistive heater kept in thermal contact with the sample cell. The actual sample temperature was measured by two thermocouple and electronically controlled by a PID device; the overall temperature stability was

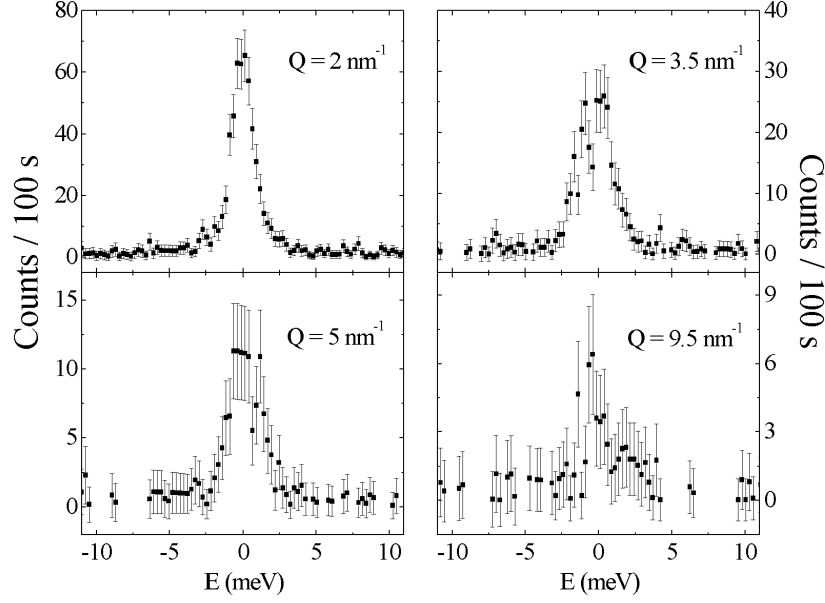


Figure 3.1: Empty cell spectra at the Q values indicated in the panels.

better than 0.2 K . All the experimental setup was in high vacuum ($\sim 10^{-8}\text{ mbar}$) in order to avoid thermal gradients and spurious scattering from air surrounding the cell. During the same experiment we also collected IXS spectra of pure He in correspondence of the two extreme temperatures (33 and 184 K) probed in the case of $He_{0.8}Ne_{0.2}$. In this case the He pressure was set in order to obtain the same He density as in the $He_{0.8}Ne_{0.2}$ mixture at the same temperature. In the case of He data at 33 K the exploited Q -range was limited to $5 \div 25\text{ nm}^{-1}$.

3.2 Ancillary measurements

Ancillary energy resolutions measurements of the nine analyzer system has been performed at low temperature (5 K) on a Plexiglas glass. For each experimental condition (i.e., for each exploited angle of the spectrometer arm and slit aperture), it is found that the energy resolution function, $R(\omega)$, was quite constant and with

a full-width-half-maximum of about 1.4-1.7 meV . Also a bump was found in the $R(\omega)$ of analyzer 3 and 4, located at 8 meV in the energy gain of the spectrum. However, the convolution procedure described further below, is able to account for the spurious effect. Example of $R(\omega)$ are reported in fig. 3.4, together with the experimental spectra. Experimental artifacts able to affect IXS data may also come from the optical windows of Nb cell, as well as from the windows of vacuum chamber. In order to avoid spurious scattering from vacuum chamber, two precautions were taken:

- The windows has been placed so far from the scattering center (i.e. the sample) that it is outside the depth of field of the spectrometer.
- Close to the vacuum chamber exit window has been placed an absorbing material (beam stop) in order to block the scattering from this window.

With the end to quantify the scattering from the HP cell windows, empty cell measurements were performed. Some of these scans are plotted in fig. 3.1. The measured signal is very low if compared with the signal from the sample, even at the higher Q . Furthermore, the intensity is overestimated if compared to the real empty cell contribution, because the data reported in the figure are not corrected for the absorption of the sample. Therefore, this eventual spurious effect is simply neglected.

3.3 Mesoscopic regime: data analysis

The raw data $I(Q, \omega)$ are related to $S^{ex}(Q, \omega)$:

$$I(Q, \omega) = I(Q)[n(\omega, T)S^{ex}(Q, \omega) \otimes R(Q, \omega)] + c(Q). \quad (3.1)$$

$R(Q, \omega)$ is the resolution function, the symbol \otimes stand for numerical convolution, $I(Q)$ is an overall intensity factor, $c(Q)$ is a background term that takes into

account of the electronic background of the detector and the environmental one.

$n(\omega, T)$ is the adimensional detailed balance factor:

$$n(\omega, T) = \frac{\hbar\omega/k_B T}{1 - e^{-\hbar\omega/k_B T}}, \quad (3.2)$$

where k_B is the Boltzmann's constant and T the system temperature. In a binary system, the experimentally measured $S(Q, \omega)$ is related to the partial dynamic structure factors through weighting coefficients, which depend on the experiment.

For example, in the FZ representation:

$$S^{ex}(Q, \omega) = I^{11}S^{11}(Q, \omega) + I^{12}S^{12}(Q, \omega) + I^{22}S^{22}(Q, \omega), \quad (3.3)$$

where the apices 1 and 2 refer to the two specie components and $I^{\alpha\beta}$ are the weighting coefficients.

The data analysis consists of a fitting procedure based on a standard minimization of the χ^2 , defined as:

$$\chi^2 = \sum_{i=1}^N \frac{(I(Q, \omega_i) - y_i)^2}{\sigma_i}, \quad (3.4)$$

with N the number of data points in the IXS spectra, y_i are the measured counts at the energy transfer $\hbar\omega_i$, σ_i is the relative standard deviation. A Poisson statistics is assumed, so that $\sigma_i = \sqrt{y_i}$. The minimization was performed with the software MATLAB, employing two routines: one exploiting the Nelder-Mead Simplex algorithm [55] and, subsequently, a second one based on a large-scale algorithm, which uses the method of preconditioned conjugate gradients (PCG) [56, 57]. The errors were estimated through the calculation of the covariance matrix.

In the following two sections the chosen fitting model used for $S(Q, \omega)$ in the case of pure *He* and *He/Ne* mixtures in the mesoscopic regime will be briefly discussed. As emphasized in chap. 1 in binary mixtures the hydrodynamic breaks off at frequencies usually lower than these ones of one-component fluids (i.e $\omega(Q)$):

3. The Helium/Neon mixtures from the mesoscopic to the single particle regimes

$Q \gg \lambda^{-1}$). As rough indication, one can consider that the mesoscopic regime for binary mixtures is reached for $Q \cdot \lambda \geq 1$, where λ is the mixture average mean free path defined as:

$$\lambda = \frac{1}{\pi\sqrt{2}\bar{\sigma}^2n}, \quad (3.5)$$

with $\bar{\sigma}^3 = \sigma_{He}^3 + \sigma_{Ne}^3$ and $\sigma_{He(Ne)}$ the $He(Ne)$ diameter.

3.3.0.1 Model function for He in the mesoscopic region

The function used to evaluate $S(Q, \omega)$ in the case of He in the mesoscopic region has been derived in the frame of memory function formalism (see sec. 1.3). In this frame $S(Q, \omega)$ can be related to memory function through the eqs. 1.149 and 1.157. Truncating the continued fraction at the 3^{rd} order and assuming that $K(Q, t) = K(Q)\delta(t)$, after some straightforward algebra, $S(Q, \omega)$ can be written in the form of eq. 1.159. This function was then inserted in eq. 4.1 in order to fit experimental data. It is now worth recalling the underlying hypothesis made for obtaining eq. 1.159. The first one was the assumption that the specific heat ratio, $\gamma(Q)$, is about 1. In this case the thermal relaxation can be neglected. In the case of Lennard-Jones fluids this is generally not true in the hydrodynamic region, but values of $\gamma(Q) \sim 1$ were found for Ne and He [58] in the Q range where the present experiments have been performed. The second hypothesis is that all dynamics inducing time decays of density fluctuation can be described by a time decay with a single timescale. The main argument supporting the choice of a single timescale is the finding, obtained by computer simulations on fluid Argon [59]. In that case the approximations made either using a single or a double timescale coincide for $Q > 5nm^{-1}$. Such single timescale approximations was already successfully used for analyzing IXS data on liquids and gases [23, 60]. The use of multiple timescale, moreover, would introduce new fitting parameters and, consequently, a strong correlation in the minimization routine.

The parameters $M(Q)$, $N(Q)$, $K(Q)$ have been kept free to vary in the fitting routines, together with the intensity factor $I(Q)$ and the background $c(Q)$. The temperature T was fixed to the measured value. The quantities $\omega_0(Q)$, $\omega_\infty(Q)$, $\tau_c(Q)$ have been then calculated through the relations 1.160. The parameter $K(Q)$ and the relative $\tau_c(Q)$ was also calculated from $N(Q)$ by means of 1.165 and 1.166. The agreement of the results obtained with the two procedure is fairly good. This provides an overall consistency check of data analysis. In fig.3.2 raw IXS data at selected Q values (black circles) are reported with the best fit lineshape (red line) and the pertinent instrumental resolution (thin black line). A very good agreement between raw data and best fit lineshape can be observed in the whole explored Q range.

3.3.0.2 Model function for He/Ne mixtures in the mesoscopic region

In the case of He/Ne mixtures a preliminary set of fit was performed on the IXS data collected from the $He_{0.8}Ne_{0.2}$ mixture at $T = 33 K$ and $T = 184 K$ selecting as model the one-component viscoelastic function. The fitting procedure is identical to that one employed in the case of pure He . A selection of raw IXS data with the relative best fit lineshape and instrumental resolution are shown in fig. 3.3. The agreement is quite good. The parameters $M(Q)$, $N(Q)$ and $K(Q)$ are extrapolated from the fitting procedure, whereas the quantities $\Omega_0(Q)$, $\Omega_\infty(Q)$, $\tau_c(Q)$ have been successively calculated, as for the monoatomic fluid. The value of the compliance relaxation time in all the investigated Q range is comparable with that of the pure He at the same mixture's temperature and equivalent He density. Conversely, the value of $\omega_0(Q)$ and $\omega_\infty(Q)$ are sensibly lower than what found in pure He . In particular for $T = 184 K$ the extrapolated value of $c_0(Q) = \omega_0(Q)/Q$ is comparable to the value of the adiabatic sound speed of Ne calculated from the Equation of State (EoS) at the same mixture's temperature and equivalent density. $\tau_c(Q)$, cal-

3. The Helium/Neon mixtures from the mesoscopic to the single particle regimes

culated from the Lovesey's relation shows a relevant mismatch with respect to the value obtained by the direct estimation of $K(Q)$ from the fitting. In the high Q region the discrepancy can be filled if τ_c is multiplied by a constant $c \sim 0.3$. This value can, in first approximation, be associated to the square root of the mass ratio between the mixture components, $(M_{He}/M_{Ne})^{1/2} = 0.43$, i.e approximately to the ratio between the maxwellization times of He and Ne . The previously reported observation point out how the mixture is not appropriately described, in the whole probed Q range, as an "average" fluid modelled by a single-component viscoelastic function, whereas it suggests a decoupling of collective dynamics between light and heavy particles. It has been decided, then, to use the generalization of memory function framework, which is extensively reviewed in sec. 1.3.

The IXS cross section can be expressed in the Faber-Ziman representation, as (see subsec. 2.1.2):

$$\frac{\partial^2 \sigma}{\partial \Omega \partial \omega_f} \overset{IXS}{=} r_0^2 N \frac{k_f}{k_i} \hat{\epsilon}_f \cdot \hat{\epsilon}_i \sum_{\alpha, \beta=1,2} (x_\alpha x_\beta)^{1/2} f^\alpha(Q) f^\beta(Q) S^{\alpha\beta}(Q, \omega). \quad (3.6)$$

All the quantities appearing in 3.6 are defined in subsec. 2.1.2. In particular $f^\alpha(Q)$ is the atomic form factor of specie α , whose magnitude, in first approximation, is proportional to the atomic number. It follows that $f^{Ne}/f^{He} \simeq 5$. In $\frac{\partial^2 \sigma}{\partial \Omega \partial \omega_f} \overset{IXS}{}$, therefore, the leading contribution arises from $S^{NeNe}(Q, \omega)$. Consequently, it is expected that the value of the parameters $M(Q)$ and $N(Q)$ obtained by the one-component viscoelastic fitting of He/Ne mixtures is similar to that relative to $S^{NeNe}(Q, \omega)$. This explains the results reported in fig. 3.3.

In the fitting procedure it has been chosen to use the FZ representation because 1) the obtained partial dynamic structure factors can be more easily interpreted in relation to the microscopic dynamics, 2) it is supposed that in the investigated Q -range the partial density fluctuations are quite independent dynamical variable. This last hypothesis can be "a posteriori" verified by comparing the value of

$N_{12}(Q, t = 0)$ obtained from the fitting.

In conclusion the expression for $S(Q, \omega)$ that have to be inserted in eq. 4.1 is:

$$S^{ex}(Q, \omega) = [f^{He}(Q)]^2 S^{HeHe}(Q, \omega) + [f^{He}(Q)f^{Ne}(Q)] S^{HeNe}(Q, \omega) + [f^{Ne}]^2 S^{NeNe}(Q, \omega), \quad (3.7)$$

where the atomic form factor, $f^{He(Ne)}$, were calculated for each Q following [46], and were kept fix during the minimization routine. The partial dynamic structure factors are the elements of the matrix

$$\begin{aligned} \mathbf{S}(Q, \omega) &= \begin{pmatrix} S^{HeHe}(Q, \omega) & S^{HeNe}(Q, \omega) \\ S^{HeNe}(Q, \omega) & S^{NeNe}(Q, \omega) \end{pmatrix} = \\ &= \frac{1}{2\pi} \left[\mathbf{F}(Q) \left(-i\omega\mathbf{I} + \frac{\mathbf{M}(Q)}{-i\omega\mathbf{I} + \frac{\mathbf{N}(Q)}{-i\omega\mathbf{I} + \mathbf{K}(Q)}} \right)^{-1} + a.c. \right]. \end{aligned} \quad (3.8)$$

From 1.44, 1.158 and by definition of static structure factor:

$$\begin{aligned} \mathbf{F}(Q) &= \begin{pmatrix} S^{HeHe}(Q) & S^{HeNe}(Q) \\ S^{HeNe}(Q) & S^{NeNe}(Q) \end{pmatrix}, \\ \mathbf{M}(Q) &= \begin{pmatrix} Q^2 k_B T / M_{He} & 0 \\ 0 & Q^2 k_B T / M_{He} \end{pmatrix} \mathbf{F}(Q)^{-1}, \\ \mathbf{N}(Q) &= \begin{pmatrix} N^{HeHe} & N^{HeNe}(Q) \\ N^{HeNe}(Q) \frac{M_{He}}{M_{Ne}} & N^{NeNe}(Q) \end{pmatrix}. \end{aligned} \quad (3.9)$$

The identity $N^{NeHe} = N^{HeNe}(M_{NeNe}/M_{HeHe})$ follows from symmetry requirements. The matrix $\mathbf{K}(Q)$ is calculated through the relations 1.169.

The parameters determined by the fitting procedure are, therefore, $S^{HeHe}(Q)$, $S^{HeNe}(Q)$, $S^{NeNe}(Q)$, $N^{HeHe}(Q)$, $N^{HeNe}(Q)$, $N^{NeNe}(Q)$, other then the background $c(Q)$ and the overall intensity factor, $I(Q)$. The temperature T was fixed to the measured value.

The raw IXS data with the relative best fit curves and instrumental resolutions are reported in figs. 3.4, 3.5, 3.6. The agreement between the model function and the experimental spectra is good for the whole analyzed Q range and for all the thermodynamic conditions. The logarithmic scale emphasizes the agreement also in the high frequency spectral tails. Such agreement is sometimes lost for Q values approaching the maximum of the dynamic structure factor. This disagreement could be associated to the approximation introduced both by using relations 1.169 and by truncating the memory function to the third order. As already mentioned, the resolution functions corresponding to the spectra at $Q = 7.9$ and 10.9 nm^{-1} present a bump around 8 meV . This also reflects in the line shape of the relative sample spectra. Nevertheless the convolution process can well take into account this feature. To our knowledge, the above described viscoelastic model is employed for the first time to analyze experimental data of binary systems.

A final observation concerns the choice of a single relaxation time scale also in the case of binary mixtures. The existence of more than one timescale for such systems has been postulated [36], even if no clear experimental observations have been reported. Nevertheless, this choice is based 1) on the need of a model simple enough to be used in a fitting procedure and, 2) on the hypothesis [36] that the relaxation time different from the Maxwellization are frozen at the Q 's probed by the experiment. The last hypothesis can be verified a "posteriori". As it will be shown in 3.4.5, this hypothesis doesn't hold at the lower probed Q 's.

3.4 Mesoscopic region: experimental results

In the following the results of the data analysis of the $He_{0.8}Ne_{0.2}$ mixture at the three probed thermodynamic conditions are reported. First, the obtained values of longitudinal current spectra are discussed; then the matrix elements at $t = 0$ of the zero ($\mathbf{F}(Q)$) and second ($\mathbf{N}(Q)$) order memory functions, as directly obtained

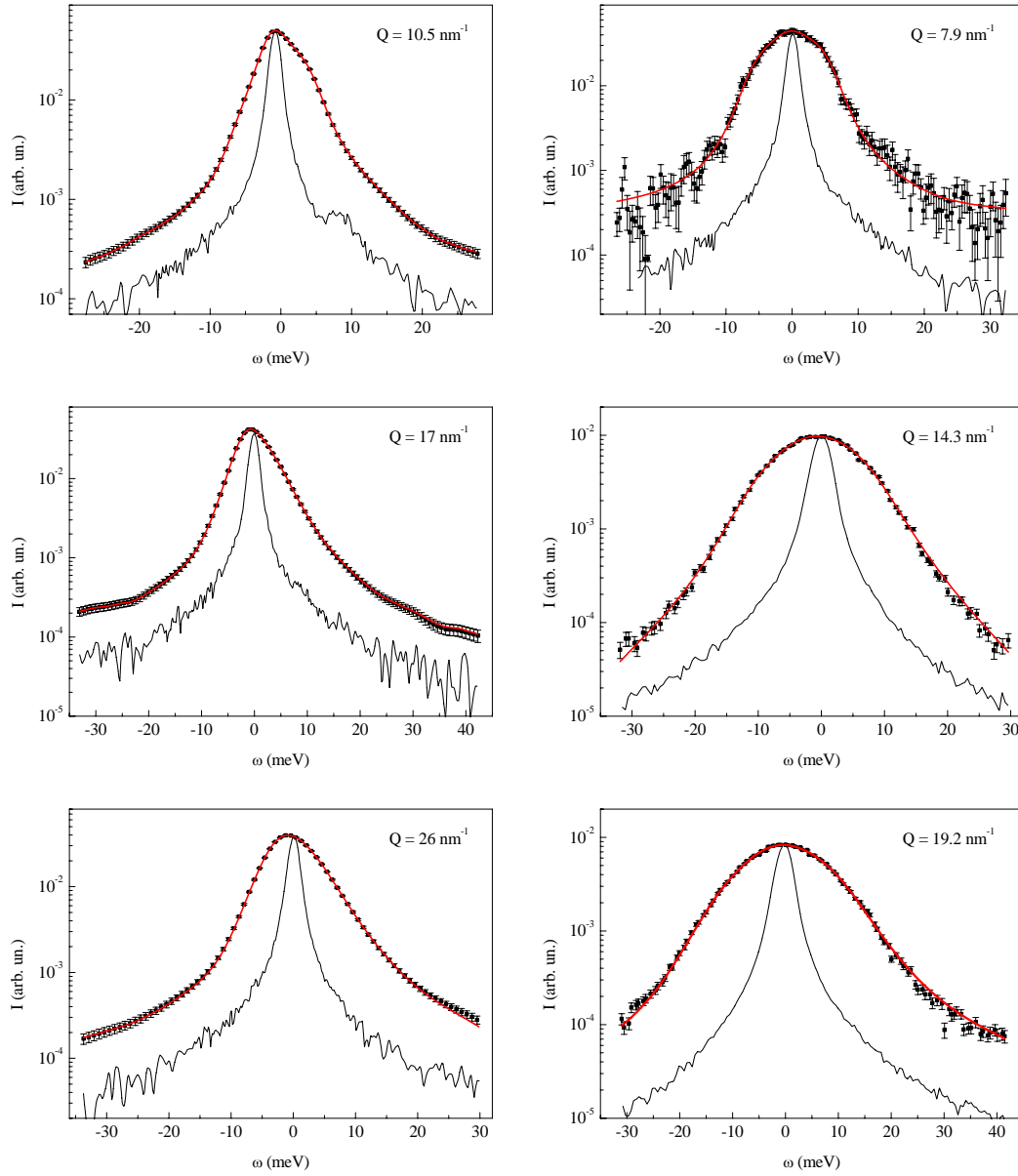


Figure 3.2: IXS spectra of *He* at $T = 33\text{ K}$, $n = 27.5\text{ nm}^{-3}$ (left panel) and $T = 184\text{ K}$, $n = 9.8\text{ nm}^{-3}$ (right panel). The corresponding best fit curve obtained as described in the text and the instrumental resolution function are represented by solid red line and dotted black line, respectively.

3. The Helium/Neon mixtures from the mesoscopic to the single particle regimes

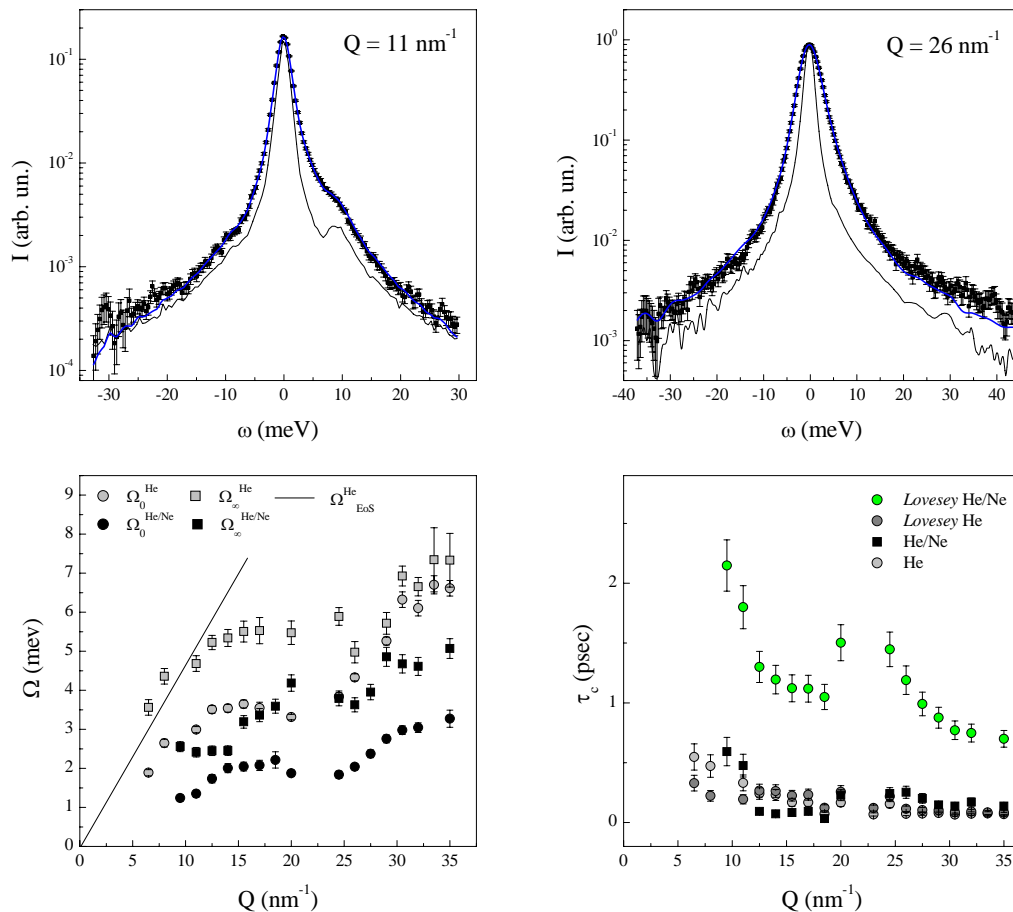


Figure 3.3: *Upper panels:* IXS spectra of $He_{0.8}Ne_{0.2}$ mixture at $T = 33 \text{ K}$ and $n = 34.4 \text{ nm}^{-3}$. The corresponding best fit curve as obtained by the viscoelastic model for one-component systems and the instrumental resolution curve are represented by solid blue line and dotted black line, respectively. *Lower panels:* $\Omega_0(Q)$, $\Omega_\infty(Q)$, $\tau_c(Q)$ of the $He_{0.8}Ne_{0.2}$ mixture compared with the corresponding quantities of He at the same mixture temperature and equivalent density. The full line is the expected dispersion of $\Omega_0(Q)$, as estimated by EoS. The values of τ_c obtained by using the Lovesey expression and directly obtained by the fit are compared.

by the fitting procedure, are shown. In subsec. 3.4.3 are reported also the third order memory function, $\mathbf{K}(Q)$, obtained by 1.169. Finally, the behavior of infinite and zero frequency sound velocities, ω_∞/Q and ω_0/Q , the compliance time, τ_c and longitudinal viscosity, η_L , derived by $M(0)$, $N(0)$ and $K(Q)$, are presented and discussed.

3.4.1 Longitudinal Current Spectra

The employed analysis allows to derive the calculated partial dynamic structure factors, S^{HeHe} , S^{HeNe} , and S^{NeNe} . moreover, exploiting 1.22-1.8, the density-density and concentration-concentration dynamic structure factors can be deduced:

$$\begin{aligned} S^{nn} &= c_{He}S^{HeHe} + 2\sqrt{c_{He}c_{Ne}}S^{HeNe} + c_{Ne}S^{NeNe} \\ S^{cc} &= c_{He}c_{Ne}[(c_{He} - c_{Ne})S_{HeNe} + \sqrt{c_{He}c_{Ne}}(S^{HeHe} - S^{NeNe})]. \end{aligned} \quad (3.10)$$

The relative longitudinal currents:

$$J(Q, \omega) = \omega^2 S(Q, \omega) \quad (3.11)$$

can be finally obtained. The multiplication by ω^2 depletes the spectral width of the central peak that, in $S(Q, \omega)$, sometime could mask the fingerprint of collective modes. The following general trend can be associated to the Q evolution of the longitudinal current spectra:

- the “low Q ”-range (i.e $Q \cdot \lambda \sim 1$) is reached only for the highest investigated density ($n = 34.4 \text{ nm}^{-3}$, $T = 33 \text{ K}$) at $Q < 11 \text{ nm}^{-1}$ (see top panel of fig. 3.4). In this case the J^{HeHe} , J^{NeNe} and J^{HeNe} have a peak at a common frequency, of about 44 meV . Such a peak is also reproduced in J^{nn} and J^{cc} . Since positive value of J^{HeNe} means in phase motion of He and Ne , such a feature can be associated to a longitudinal acoustic mode involving both species. An higher frequency peak is observable in J^{HeHe} . It can be associated to

3. The Helium/Neon mixtures from the mesoscopic to the single particle regimes

the high frequency shoulder exhibited by $J^{cc}(Q, \omega)$. Moreover, its characteristic frequency is in a range where $J^{HeNe} < 0$, which indicates out-of-phase motions of the two components. This behavior is characteristic of optical-like character of this high frequency modes. Finally, a very low frequency shoulder is present both in J^{HeHe} and J^{NeNe} . Its characteristic frequency is around $D_{12}Q^2$, where D_{12} is the interdiffusion coefficient estimated¹ in the Generalized Enskog theory [61]. Moreover, it corresponds to negative values of J^{HeNe} . These observations suggest to associate this mode to interspecies diffusion dynamics. In conclusion the “low- Q ” regime is characterized by the presence of a diffusive mode and two collective modes, one is of acoustic-like character and involves the in-phase motion of the two components, while the other is optic-like and involves vibrations of He particles.

- In the “intermediate” Q -range (i.e $1 < Q \cdot \lambda < 3$) the low frequency diffusive mode can be clearly observed and it dominates the J^{NeNe} and J^{nn} spectra. This mode has been already reported in this Q -range for He/Ne mixtures, and a similar behavior was found [16]. The high frequency peak in J^{HeHe} , oppositely to what observed in the low Q -range, not corresponds to $J^{HeNe} > 0$, thus indicating no longer out-of-phase motion of the two species particles. Furthermore, a peak at the same frequency is present in J^{nn} . It can be supposed then such a high-frequency collective mode is of acoustic-like

¹The interdiffusion coefficient is calculated as $D_{12} = \frac{D_{12}^0}{Y_{12}}$, where D_{12}^0 is the value estimated for the corresponding gaseous system and Y_{12} is a corrective term to take into account of the local interactions for denser fluid. It is $Y_{12} = 1 + \frac{2}{3}\pi n_1 \sigma_1^3 \left(\frac{\sigma_1 + 4\sigma_2}{4\sigma_1 + 4\sigma_2} \right) + \frac{2}{3}\pi n_2 \sigma_2^3 \left(\frac{4\sigma_1 + \sigma_2}{4\sigma_1 + 4\sigma_2} \right)$ and $D_{12}^0 = 0.002628 \frac{(T^3(M_1+M_2)/2M_1M_2)^{1/2}}{P\sigma_{12}^2\Omega_{12}^{(11)*}(T_{12}^*)}$, where $T_{12}^* = k_B T / \epsilon_{12}$ (being ϵ_{12} the coefficient of the Lennard-jones potential: $U_{ij} = 4\epsilon_{ij} \left(\left(\frac{\sigma_{ij}}{r} \right)^{12} - \left(\frac{\sigma_{ij}}{r} \right)^6 \right)$, $i, j = 1, 2$) and $\Omega_{12}^{(l r)*} = \frac{\sigma_{12}^2}{8} \left(\frac{2\pi k_B T_{12}^*}{M_1 M_2 / (M_1 + M_2)} \right)^{1/2} \left(2 - \frac{1+(-1)^l}{1+l} \right) (1+r)!$ is the Chapman-Cowling integral for the hard-sphere model. It is found $D_{12}^{(T=33 K, P=535 bar, n=34.4 nm^{-3})} = 0.0032 \frac{nm^2}{psec}$, $D_{12}^{(T=82 K, P=320 bar, n=18.45 nm^{-3})} = 0.026 \frac{nm^2}{psec}$, $D_{12}^{(T=184 K, P=408 bar, n=12.2 nm^{-3})} = 0.074 \frac{nm^2}{psec}$.

nature, and it is supported principally by the *He* particles.

- In the “high” Q -range (i.e. $Q \cdot \lambda > 3$) the total intensity of the J^{HeNe} is approaching zero. This behavior can be associated to a complete dynamics decoupling. In this condition, a single peak is observable in both in J^{HeHe} and J^{NeNe} , with two distinct frequencies. Furthermore, in the case of the less dense mixture ($n = 12.2 \text{ nm}^{-3}$, $T = 184 \text{ K}$) the peaks frequency are well approximated by the expression $(2k_B T Q^2 / M_{He(Ne)})^{0.5}$ (see fig. 3.9), i.e. by representing the *HeHe* and *NeNe* dynamic structure factors as a Gaussian function with variance $\sigma^2 = k_B T Q^2 / M_{He(Ne)}$. This behavior suggests that the single particle regime is approached.

3.4.2 Zero order memory function

Fig. 3.7 shows the matrix elements of $\mathbf{F}(Q) \equiv \mathbf{S}(Q)$. As check of consistency, the calculated values of $S(Q)$ [62] are plotted as well. The calculation uses the hypernetted chain (HNC) closure relations in the Ornstein-Zernike (OZ) equation [63], solved with the Gillan method [64] extended to binary systems. In the case of the mixture at $T = 33 \text{ K}$ and $n = 34.4 \text{ nm}^{-3}$, the computation is not convergent. In this case $S(Q)$ obtained by the fit is compared with computation results obtained for similar density ($n = 36 \text{ nm}^{-3}$) and higher temperature ($T = 60 \text{ K}$). The agreement is rather good in the case of S^{NeNe} and S^{HeNe} , whereas a systematic shift is observed for S^{HeHe} at all the probed thermodynamic conditions. The rising of S^{NeNe} at low Q is ascribed to a demixing tendency of the system in the probed thermodynamic conditions, already observed for *He/Ne* mixtures [65]. This behavior, anyway, seems not directly influence the results reported in the present work.

3. The Helium/Neon mixtures from the mesoscopic to the single particle regimes

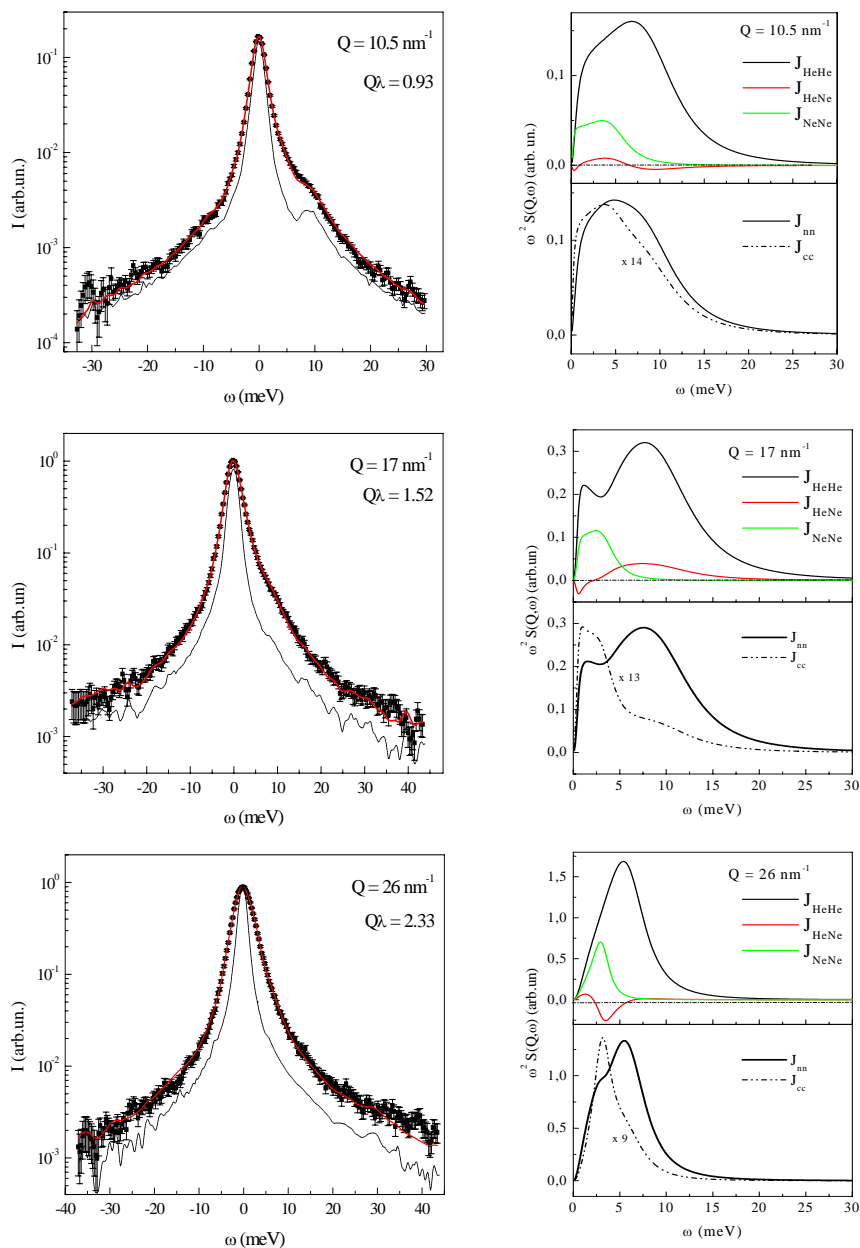


Figure 3.4: IXS spectra of $He_{0.8}Ne_{0.2}$ mixture at temperature $T = 33 \text{ K}$ and total density $n = 34.4 \text{ nm}^{-3}$ (left panel). The corresponding best fit curve as obtained by the viscoelastic model for binary systems (see subsec. 1.3.2) and the instrumental resolution curve are represented by solid red line and dotted black line, respectively. The longitudinal currents extrapolated by the fitting procedure, as well, are reported in the right panel. IXS spectra and longitudinal currents at wavevector in the “low” (top panel) “intermediate” (middle panel) and “high” range (bottom panel) are reported.

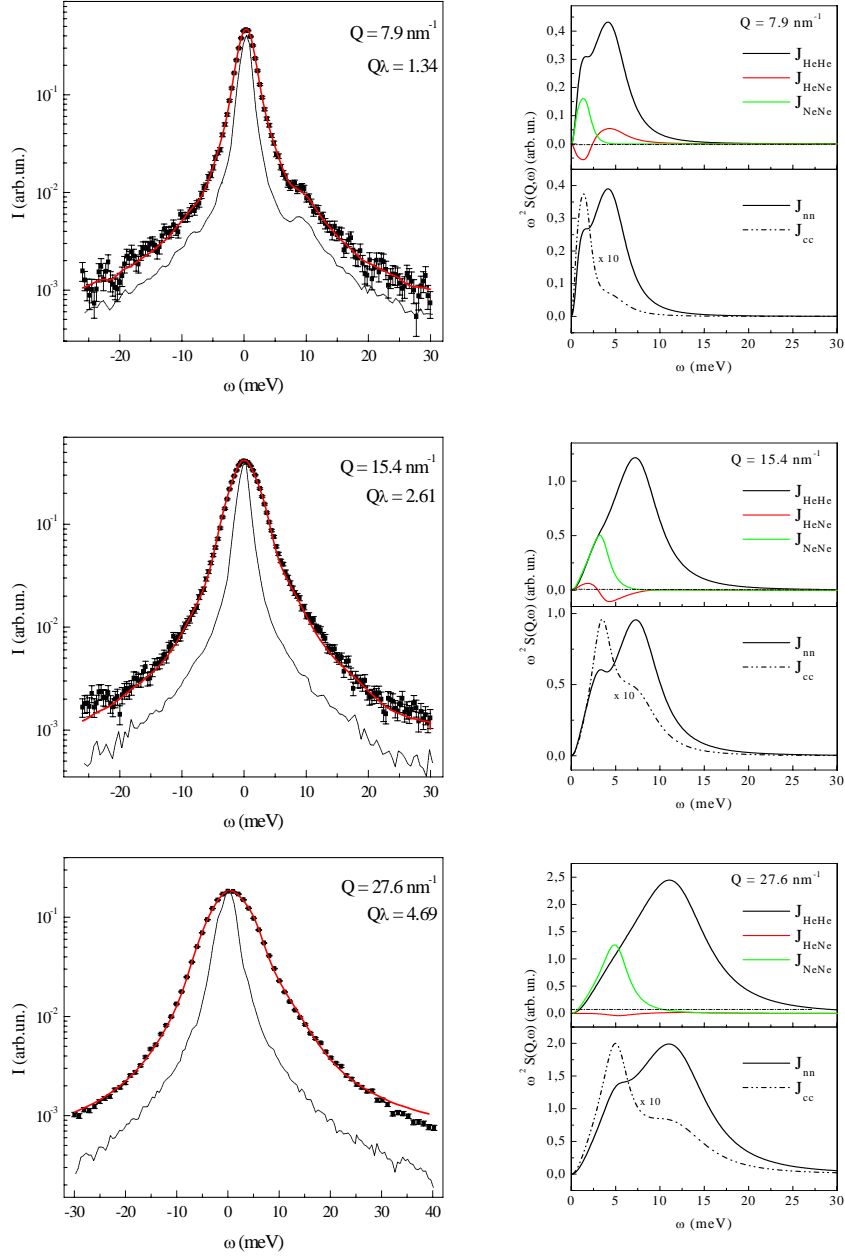


Figure 3.5: IXS spectra of $He_{0.8}Ne_{0.2}$ mixture at temperature $T = 82$ K and total density $n = 18.45$ nm^{-1} (left panel). The corresponding best fit curve as obtained by the viscoelastic model for binary systems (see subsec. 1.3.2) and the instrumental resolution curve are represented by solid red line and dotted black line, respectively. The longitudinal currents extrapolated by the fitting procedure, as well, are reported in the right panel. IXS spectra and longitudinal currents at wavevector in the “intermediate” (top and middle panel) and “high” range (bottom panel) are reported.

3. The Helium/Neon mixtures from the mesoscopic to the single particle regimes

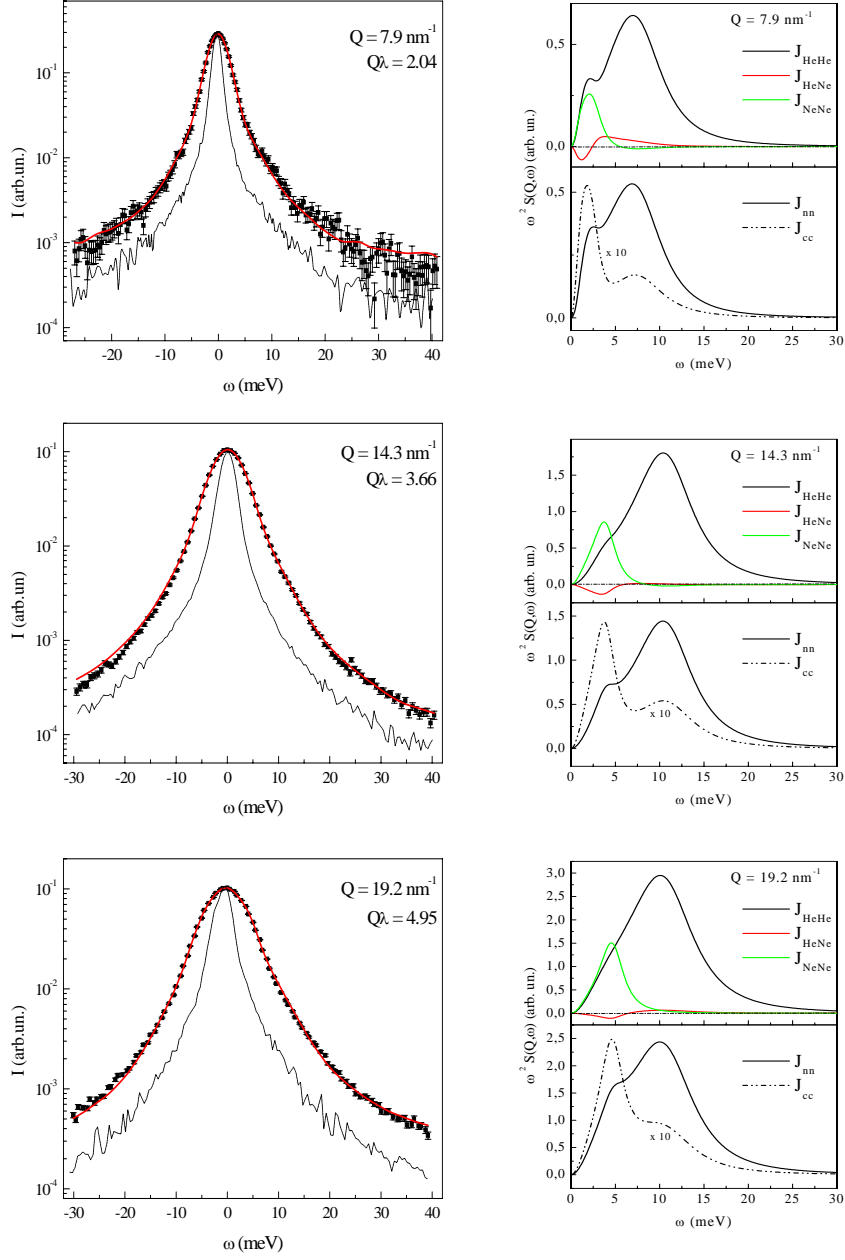


Figure 3.6: IXS spectra of $He_{0.8}Ne_{0.2}$ mixture at temperature $T = 184$ K and total density $n = 12.2 \text{ nm}^{-3}$ (left panel). The corresponding best fit curve as obtained by the viscoelastic model for binary systems (see subsec. 1.3.2) and the instrumental resolution curve are represented by solid red line and dotted black line, respectively. The longitudinal currents extrapolated by the fitting procedure, as well, are reported in the right panel. IXS spectra and longitudinal currents at wavevector in the “intermediate” (top and middle panel) and “high” range (bottom panel) are reported.

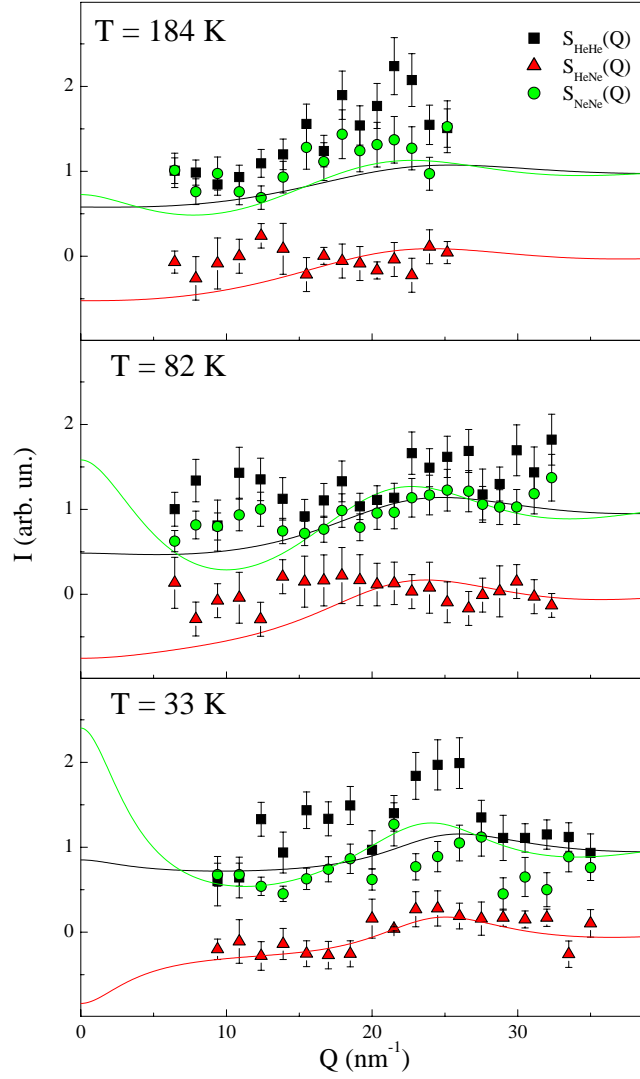


Figure 3.7: Partial static structure factors S^{HeHe} , S^{HeNe} and S^{NeNe} obtained as best fitting parameters for the three investigated thermodynamic conditions, indicated in the labels. The solid lines represent the same quantities estimated computer simulations (see text for more details).

3.4.3 Higher order memory function

The second order memory function matrix at $t = 0$, $\mathbf{N}(Q)$, is evaluated by the fitting procedure. Its elements are plotted in fig. 3.8, together with the elements of the matrix $\mathbf{K}(Q)$ obtained by eq. 1.169. The cross terms N_{HeNe} and N_{NeHe} (so as, consequently, K_{HeNe} and K_{NeHe}) are consistent with zero for the mixture at $T = 184 K$, and $n = 12.2 nm^{-3}$ for all the analyzed Q -range. At conditions $T = 82 K$ and $n = 18.45 nm^{-3}$ and at $T = 33 K$ and $n = 34.4 nm^{-3}$ these terms approach zero at Q values larger than the respective Q_{max} , i.e. the Q value roughly corresponding to the maxima of $S(Q)$ (see fig. 3.7). The vanish of cross-terms can be view as an a posteriori justification for the choice of the FZ representation. Moreover, in the same Q range $S^{HeNe}(Q)$ is, as well, consistent with zero. This two conditions assure that the matrix $\mathbf{S}(Q, \omega)$ is diagonal in the FZ representation, i.e. δn_{He} and δn_{Ne} are independent dynamical variables. In the case of the denser mixture, both $K^{HeHe}(Q)$ and $K^{NeNe}(Q)$ show a minimum around Q_{max} . This behavior can be interpreted as de Gennis narrowing phenomenon, usually observed in single fluids around Q_{max} . Here the lifetime of the density fluctuations is longer because of the strongest static correlation over distances close to the average interparticles separation.

3.4.4 Sound velocities

At each thermodynamic point investigated the parameters Ω_∞ and Ω_0 are obtained exploiting the equivalent matricial expression of 1.160. Fig. 3.9 reports the diagonal elements $\Omega_{\infty(0)}^{HeHe}$ and $\Omega_{\infty(0)}^{NeNe}$. The Q dispersion of such quantities are compared with the characteristic frequency of the He and Ne modes, determined by the maxima of the respective longitudinal current spectra, $\Omega_L^{He(Ne)}(Q) = \max[J^{HeHe(NeNe)}](Q)$. For the mixture at higher and lower analyzed temperature ($T = 33 K$ and $T = 184 K$) is reported the Ω_0 frequency of pure He measured at the same temperature

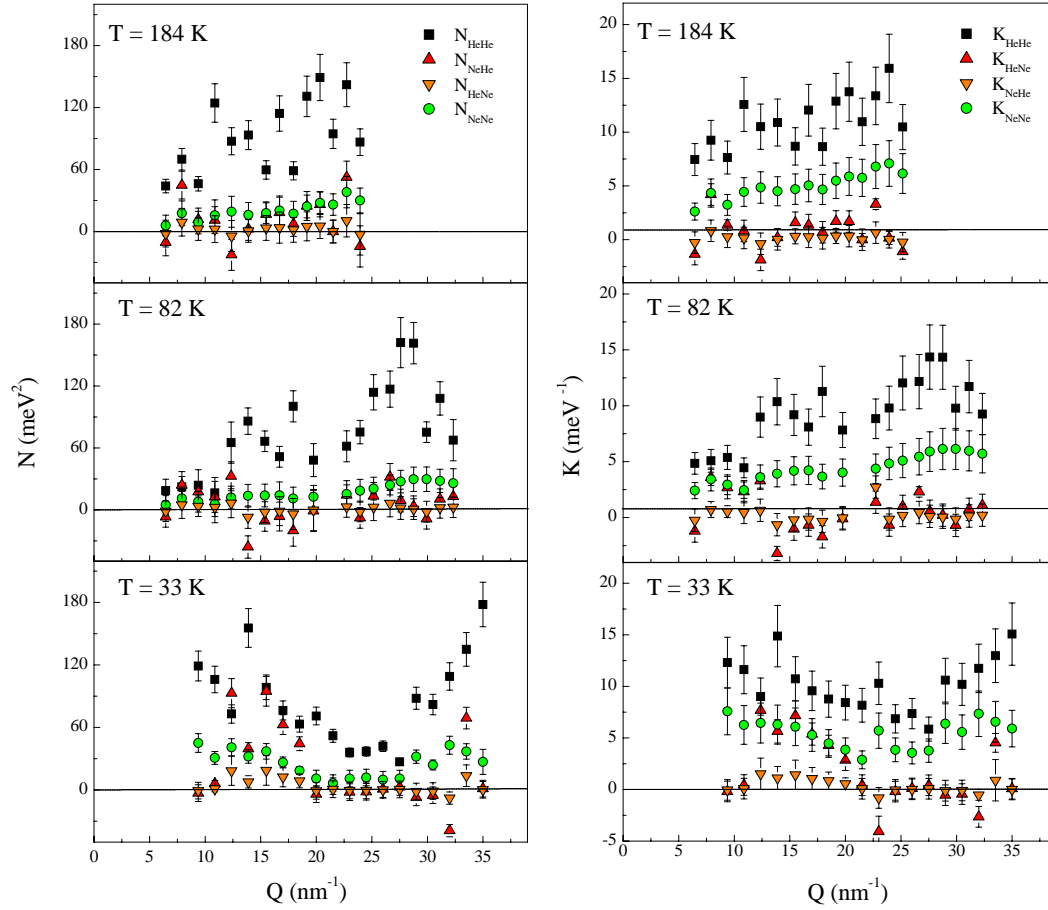


Figure 3.8: *Left panels:* matrix elements of $\mathbf{N}(Q)$ extrapolated by the fitting routine at the three investigated thermodynamic conditions, indicated in the individual panels. *Right panels:* corresponding matrix elements of $\mathbf{K}(Q)$, calculated from $\mathbf{N}(Q)$ through eq. 1.169.

3. The Helium/Neon mixtures from the mesoscopic to the single particle regimes

and equivalent mixture density (i.e. $n_{pure\ He} = x_{He}n$). $\Omega_0(Q)$ is extrapolated by a fitting procedure, using the viscoelastic model for one-component system. The first noticeable peculiarity is that $\Omega_0(0)$ and $\Omega_0(Q)$ of *He* and *Ne* are, for all the analyzed Q range, in two well separated regions. Moreover, Ω_0^{He} 's, have values comparable with the ones of pure *He*. This observation emphasizes what already suggested by the analysis of the cross term of the matrix $\mathbf{N}(Q)$, i.e. that the collective dynamics of the system in the exploited thermodynamic and Q ranges, are appropriately described by referring to the dynamics of the two specie separately. The sound velocities associated to the two mixtures components are different and can be related to the equivalent values in the pure species. The second observation concerns the comparison between Ω_∞ , Ω_0 and $max[J](Q)$. In the mixture at $T = 82\ K$ and $T = 184\ K$ the elastic regime is reached for both *He* and *Ne*, being $max[J](Q) \sim \Omega_\infty$. For the mixture at $T = 33\ K$ the *He* particles dynamics is, as well, in the elastic regime, whereas by a direct comparison of Ω_∞^{Ne} and $max[J^{Ne}](Q)$ it's possible to conclude that the crossover from the adiabatic to the elastic regime is approached at rather large Q 's, of about $Q \sim 20\ nm^{-1}$. For a single component fluid the crossover condition can be expressed as $\Omega_L(Q)\tau_s$, where τ_s is the stress relaxation time that can be identified, in the case of gaseous sample, with the Maxwellization time. In this case the crossover condition is satisfied for $Q_c \simeq \lambda^{-1}$, being λ the particles mean free path. In fig. 3.9 are reported the values of λ for the *He* and *Ne* particles, calculated following the relation (derived for a mixture of hard-sphere particles [66]):

$$\lambda_\alpha = \left(\pi \sum_{\beta=1,2} n_\alpha \sigma_{\alpha\beta}^2 \sqrt{1 + M_\alpha/M_\beta} \right)^{-1}, \quad (3.12)$$

where $\sigma_{\alpha\beta} = (\sigma_\alpha + \sigma_\beta)/2$ is the distance between the centers of the two spherical particles of diameters σ_α and σ_β at the instant of collision. Observing the values of $\lambda_{He(Ne)}^{-1}$, the previously described behavior is consistent with such a criterion.

As a further check of consistency $\Omega_\infty^{He(Ne)}$ has been calculated by using an approximation proposed by Copley and Lovesey [67] for a one-component fluid:

$$\Omega_\infty^2 = \frac{3Q^2 k_B T}{M} + \omega_E^2 \left(1 - \frac{3 \sin(Q \cdot \sigma)}{Q \cdot \sigma} - \frac{6 \cos(Q \cdot \sigma)}{(Q \cdot \sigma)^2} + \frac{6 \sin(Q \cdot \sigma)}{(Q \cdot \sigma)^3} \right), \quad (3.13)$$

where ω_E is the Einstein frequency. For a binary system it has been tentatively tried to use the same expression referring the mass M and the sphere diameter σ to each specie particles. The Einstein frequency has been expressed in the following form, which generalizes the definition given for one-component fluid to binary mixture [67]:

$$\omega_E^2(\alpha) = \frac{1}{3M_\alpha} \sum_{\beta=1,2} n_\beta \int d\mathbf{r} g_{\alpha\beta} \frac{\partial^2 \varphi_{\alpha\beta}}{\partial z^2}. \quad (3.14)$$

The pair correlation function appearing in 3.14 are calculated through a numerical solution of the OZ equations with HNC closure. As in the case of the $S(Q)$'s for the more dense mixture the fitting parameters are compared with theoretical estimations. The agreement is, in all the case, quite good. However, two discrepancies have to be noted: 1) for $T = 33 K$ the agreement at low Q is not good. This can be attributed to the use in the theoretical estimation of a pair correlation function calculated not exactly in the same thermodynamic conditions of the experiment. Another possible explanation could be found in the extension of eq. 3.13 to binary system, performed in this work. Indeed, interaction between the different specie were enclosed only in ω_E . In other words, it was implicitly assumed that the dynamics of the two mixture components is completely decoupled. This could not be completely true for such mixture at these Q -values, as also observed from the analysis of the cross term of $\mathbf{N}(Q)$; 2) at $T = 184 K$ it is observed at high- Q a systematic shift between experimental and estimated values of Ω_∞ . A possible explanation is that at such high- Q values the IA region is reached for this low density. As a further check in fig. 3.9 is plotted (solid red line) the maximum of the longitudinal current spectrum, $J_{HQ}^{He(Ne)}(Q) = \omega^2 S_{HQ}^{He(Ne)}(Q, \omega) \propto \omega^2 e^{-\frac{M_{He(Ne)} \omega^2}{2k_B T Q^2}}$,

3. The Helium/Neon mixtures from the mesoscopic to the single particle regimes

(i.e. $\max[J_{HQ}^{He(Ne)}](Q) = (2k_B T Q^2 / M_{He(Ne)})^{1/2}$) expected in the IA regime. As it emerges from the figure, both $\max[J^{He}](Q)$ and $\max[J^{Ne}](Q)$ approaches the corresponding IA value for $Q > 15 \text{ nm}^{-1}$. It's then reasonable to hypothesize that the crossover between the mesoscopic and the single particle regime is achieved at $Q \approx 20 \text{ nm}^{-1}$.

3.4.5 Relaxation times

In fig. 3.10 are reported the diagonal elements, $T_c^{HeHe} = \tau_c^{He}$ and $T_c^{NeNe} = \tau_c^{Ne}$, of the compliance relaxation time matrix defined in eq. 1.160. The Q dependence of τ_c can be described, for both the mixture components and at all the investigated thermodynamic points with a unique trend: a low- Q increase with respect to an asymptotic value reached at high Q . The characteristic length and time scale of this trend are, instead, dependent on the specie and thermodynamic condition. The aim of the following analysis is to give a first characterization of these time and length scales.

The asymptotic values of τ_c^{He} and τ_c^{Ne} have been extrapolated by an interpolation of their values with a constant function at the higher measured Q 's. The obtained parameters, $\tau_{c\infty}^{He}$ and $\tau_{c\infty}^{Ne}$, are reported in tab. 3.1 and compared with the mean free time between intermolecular collision of each specie. This last quantity is calculated as $\tau_{coll}^{He(Ne)} = \lambda_{He(Ne)} / \langle v_{He(Ne)} \rangle$, where $\langle v_{He(Ne)} \rangle = \sqrt{8k_B T / \pi M_{He(Ne)}}$ is the average velocity of a given molecule in a gas, according to the Maxwell-Boltzmann statistic. $\tau_{c\infty}^{He(Ne)}$ is well described by the estimated τ_{coll} for all the thermodynamic conditions, even if for $T = 33 \text{ K}$ the agreement between τ_{∞} and τ_{Max} is slightly less good. With the goal to define the time and length scales which characterize the low Q behavior, in fig. 3.11 is plotted the variable $\tau_c^{He(Ne)} - \tau_{c\infty}^{He(Ne)}$, assumed to be equal to τ_{coll} . The abscissa axis has then been normalized for the inverse of the single specie mean free path. At $T = 33 \text{ K}$ and $T = 184 \text{ K}$ is re-

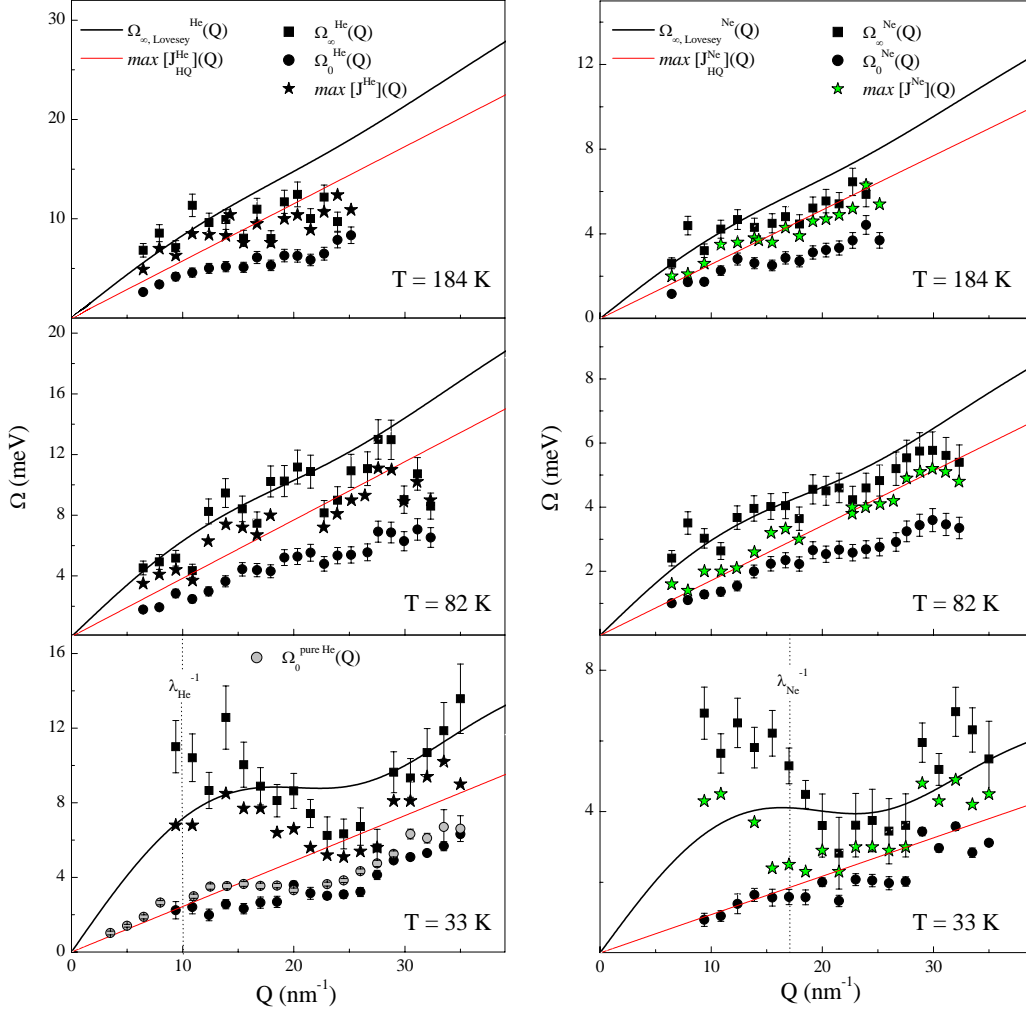


Figure 3.9: Q -dependence of Ω_0 and Ω_∞ for He (right panels) and Ne (left panels), as derived by the fitting procedure described in the text, compared with those of the maxima of $J^{HeHe}(Q, \omega)$ and $J^{NeNe}(Q, \omega)$. The thick black solid line is the estimation of ω_∞ done using eq. 3.13 extended to binary systems. The thin black dotted line is the maxima of longitudinal current spectra in the IA limit. The inverse of He and Ne mean free paths at $T = 33 K$ are reported in the appropriate panels. In all the other thermodynamic conditions the value of this quantity is lower than the lowest investigated Q , i.e. $\lambda_{He T=33K}^{-1} = 10.1 nm^{-1}$, $\lambda_{Ne T=82K}^{-1} = 9.3 nm^{-1}$, $\lambda_{He T=82K}^{-1} = 5.4 nm^{-1}$, $\lambda_{Ne T=184K}^{-1} = 6.1 nm^{-1}$, $\lambda_{He T=184K}^{-1} = 3.9 nm^{-1}$.

3. The Helium/Neon mixtures from the mesoscopic to the single particle regimes

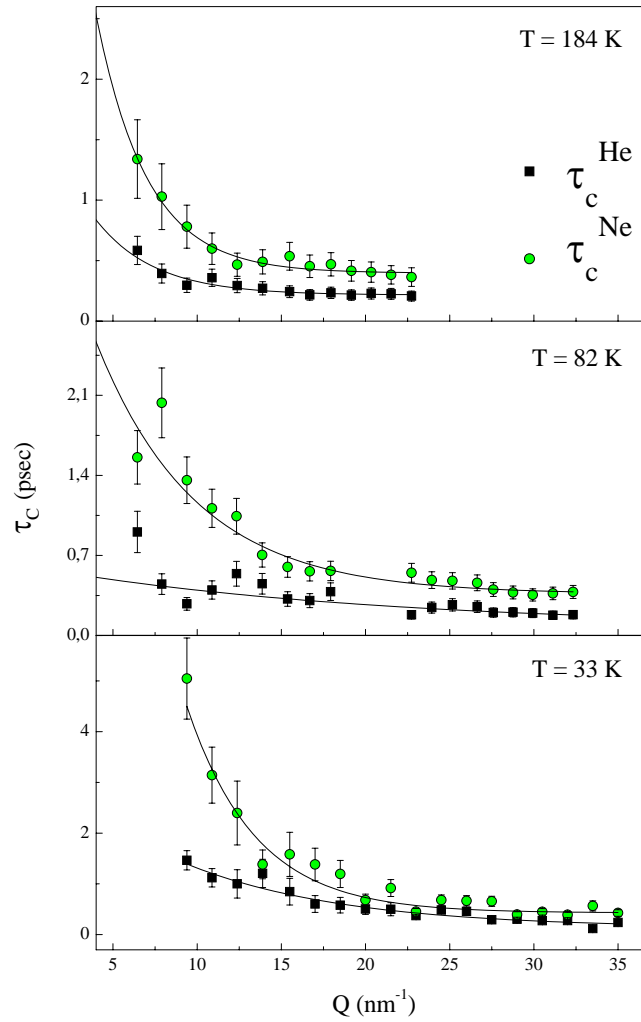


Figure 3.10: Diagonal elements τ_c^{He} and τ_c^{Ne} of the compliance relaxation time matrix at the investigated thermodynamic points. The solid lines are guides for eyes.

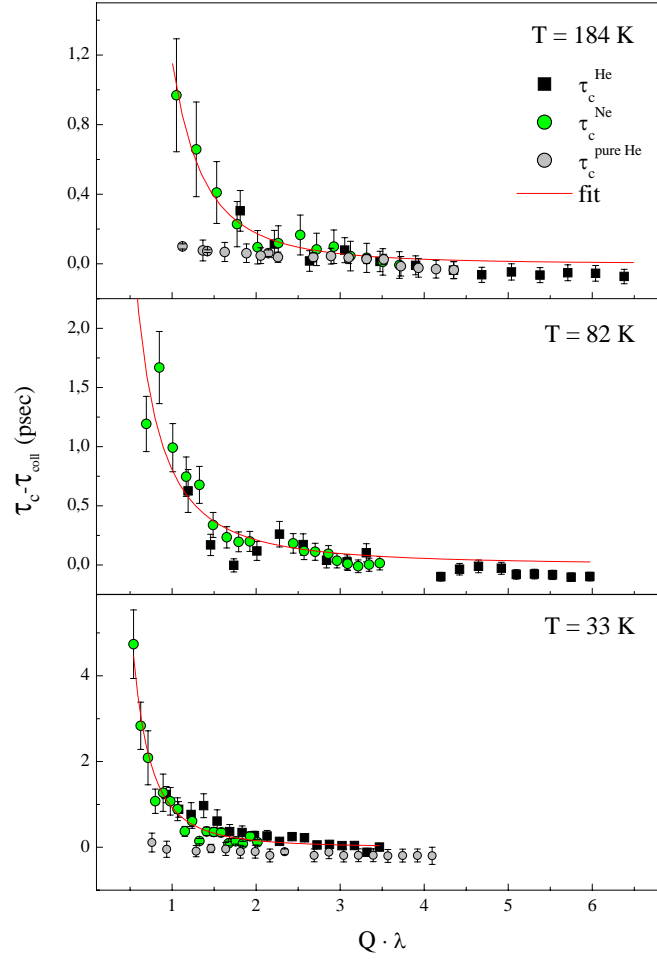


Figure 3.11: $\tau_c^{He} - \tau_{coll}^{He}$ and $\tau_c^{Ne} - \tau_{coll}^{Ne}$ as a function of $Q^* = Q \cdot \lambda_{He(Ne)}$ at the investigated thermodynamic points. One can appreciate how the *He* and *Ne* curves merge in an unique trend. Red solid lines are power law interpolations.

3. The Helium/Neon mixtures from the mesoscopic to the single particle regimes

ported also τ_c of pure *He* at the respective equivalent density and at the same temperature. The following consideration can be argued from fig. 3.11.

- The low Q trend of τ_c doesn't depend on the specie components, once the length scale has been normalized for the corresponding inverse of the mean free path.
- The increase of τ_c for $Q\lambda \sim 1$ can be recorded a characteristic of the mixture, since no similar trend is observed in pure *He*
- even though τ_c shows a weak dependency on density and temperature, in all the probed thermodynamic points the value of $\tau_c - \tau_{coll}$ at $Q\lambda \sim 1$ is around 1 *psec*.

The previous observations emphasize how length and time scale characteristic of the kinetic theory can be used to scale the τ_c trend at different temperatures and densities, even for mixtures of very different densities. Consequently, it can be argued that the relaxation time at the analyzed wavelengths is related to the equilibration process described by the Boltzmann equation, rather than to local structure effects. The observed differences of the low Q behavior between pure *He* and *He*_{0.8}*Ne*_{0.2} mixture can be, therefore, associated to the different timescales that characterize the return to equilibrium of the system. In a monoatomic fluid the mean time of flight, τ_{coll} , is the correct scale where perturbations relax to equilibrium. In other terms, in a first approximation the Maxwellization scale determines the equilibration processes. On the other hand, in a disparate-mass mixture the kinetic effects driving the equilibration of the whole system may be affected by the presence of two different atomic masses. This may introduces different equilibration scales. If the momentum relaxation time² of the lighter specie

²The momentum relaxation time of single specie can be identified with the self collision time, τ_α . It is the time over which a particle of kind α can travel before collision of particles of the same kind. It is defined as $\tau_{coll}^\alpha = \lambda_{\alpha\alpha}/\langle v_\alpha \rangle = (\pi n_\alpha \sigma_\alpha^2 \sqrt{2})^{-1} / (8k_B T / \pi M_\alpha)^{1/2}$.

is bigger than that of the heavier specie, the inefficient kinetic energy exchange between light and heavy particles, following by Newton laws, results in a relaxation time of the kinetic energy difference (i.e. temperature difference), between the two subsystems, τ_Δ , bigger than the Maxwellization time, τ_M . The return to equilibrium of the whole system is, therefore, characterized by two time scales: 1) at $t \sim \tau_M$ the momentum distribution of each subsystem are Maxwellian distribution functions characterized by two different “microscopic” temperature, 2) at $t \sim \tau_\Delta$ the two specie equilibrate at the same macroscopic temperature. In this frame, the behavior of τ_c can heuristically be interpreted in the following way: the time decay of the correlation between partial density fluctuations of a given specie is not correctly described by a single time scale (i.e. the memory function is not correctly described by the single exponential decay). Indeed, two timescale τ_M and τ_Δ , are needed to describe the equilibration of the two subsystems associated with the two mixture components and the equilibration of the whole system, respectively. However, the state of local equilibrium characterized by the two “microscopic” temperatures is not discernible from absolute equilibrium if correlations between spontaneous fluctuations are probed at shorter distances (i.e. for $Q \cdot \lambda_\alpha \geq 1$). This because the inefficient kinetic exchanges between the two species implies that several subsequent collisions (and thus long time/length scales) are needed for the equilibration of the whole system. Then, two time scales, different for the two subsystems and identified with τ_{coll}^α , can describe the decay of the single specie correlation functions at such lengthscales.

A more quantitative comparison with the frame described above, which is usually referred to as “two temperature theory” for disparate gas mixtures, is done in the following. The Maxwellization scale can be estimated using an hard-sphere model as the ratio between pressure and viscosity of the mixture. It is, moreover,

3. The Helium/Neon mixtures from the mesoscopic to the single particle regimes

related to the previously introduced $\tau_{coll}^{He(Ne)}$ by the relation [68]:

$$\tau_{Max} \simeq \frac{\tau_{coll}^{He} \tau_{coll}^{Ne}}{x_{He} \tau_{Ne} + x_{Ne} \tau_{He}}. \quad (3.15)$$

The relaxation time for temperature equilibration instead is given by [68]:

$$\tau_{\Delta} = \frac{2k_B T}{(M_{He} + M_{Ne}) D_{12}}. \quad (3.16)$$

The ratio $n_S = \tau_{Max}/\tau_{\Delta}$ is a characteristic mixture number, independent on temperature and pressure, referred to as the Modified Schmidt number [68]. The values of τ_{Δ} for each thermodynamic point are reported in tab. 3.1. The criterion for the existence of a two-temperature regime is then simply $n_S < 1$, i.e. $\tau_{\Delta} > \tau_{Max}$. For the $He_{0.8}Ne_{0.2}$ mixture it has been calculated $n_S = 0.49$ ³. Finally, to benefits of more quantitative insight, each pair of τ_c^{He} and τ_c^{Ne} data sets corresponding to a given thermodynamic point has been fitted by a power law:

$$\tau_c^{He(Ne)} - \tau_{coll}^{\alpha} = \frac{\tau_0}{(Q \cdot \lambda^{\alpha})^l}. \quad (3.17)$$

The values of τ_0 and l extrapolated are reported in tab. 3.1. Observing the values of fitting parameters reported in tab. 3.1 it results that the parameter l falls in an interval between 1.9 and 2.7 without a clear temperature or density dependence; in first approximation it can be, therefore, posed $l = 2$. The extrapolated τ_0 values are around the estimated τ_{Δ} for all the analyzed thermodynamic points. In summary, the behavior of $\tau_c^{Ne(He)}$ seems to be well described in the frame of two temperature theory as a two step relaxation process (characterized by τ_{Max} and τ_{Δ} time scales) which has been approximated by the data analysis presented in this work, with a single timescale model. Indeed, the obtained Q -trend of τ_c seems to reflect the long relaxation process at a given lengthscale, while the dependence of τ_c from thermodynamic parameters seems to be well represented by the parameters τ_{Max} and τ_{Δ} , which were independently calculated.

³The value of n_S is estimated following [69]

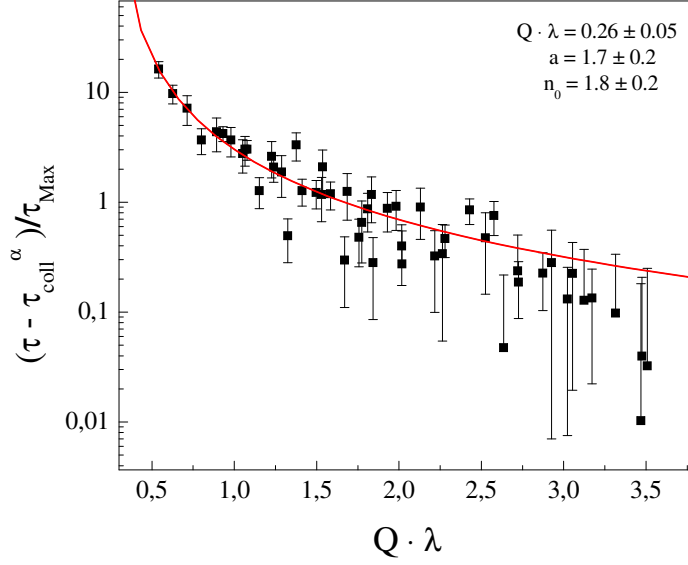


Figure 3.12: Values of $\tau_c^{He(Ne)} - \tau_{coll}^{He(Ne)}$ normalized to the stress relaxation time $\tau_{Max}^{(n,T)}$ vs. $Q^* = Q \cdot \lambda_{He(Ne)}$. The observed trend is independent from specie particles and thermodynamic conditions, and was empirically described with an exponential decay law.

Taking in mind the above considerations, in fig. 3.12 are reported the quantity $\tau_c - \tau_{coll}^\alpha / \tau_{Max}$. It follows that all data can be interpolated with the following power law:

$$\frac{\tau_c - \tau_{coll}^\alpha}{\tau_{Max}} = \frac{n_0}{[Q \cdot (\lambda^\alpha - \lambda_0)]^a}, \quad (3.18)$$

where $a = 1.7 \pm 0.2$, $n_0 = 1.8 \pm 0.2$ and $Q\lambda_0 = 0.26 \pm 0.05$. This result can be interpreted in the following way: n_0 can be identified with n_S^{-1} , whereas λ_0 is a lengthscale that define the Q range of validity of the previous description. It is, in fact, expected that at Q approaching the hydrodynamic limit τ_c loses its Q dependence and flattens toward a Q -independent plateau. This plateau, in agreement with the previous findings [39], represents the long range value of structural relaxation time. This $Q \rightarrow 0$ limit of τ_c is related to the average time scale for

3. The Helium/Neon mixtures from the mesoscopic to the single particle regimes

		$\tau_\infty(ps)$	$\tau_{coll}(ps)$	1	$\tau_0(ps)$	$\tau_\Delta(ps)$
$T = 33 K$	<i>He</i>	0.24 ± 0.03	0.24	2.6 ± 0.1	0.92 ± 0.05	0.76
$n = 34.4 nm^{-3}$	<i>Ne</i>	0.42 ± 0.03	0.31			
$T = 82 K$	<i>He</i>	0.20 ± 0.03	0.27	1.9 ± 0.2	0.80 ± 0.05	0.90
$n = 18.45 nm^{-3}$	<i>Ne</i>	0.39 ± 0.03	0.36			
$T = 184 K$	<i>He</i>	0.22 ± 0.03	0.28	2.7 ± 0.2	1.17 ± 0.06	0.92
$n = 12.2 nm^{-3}$	<i>Ne</i>	0.40 ± 0.03	0.37			

Table 3.1: Asymptotic values of compliance relaxation time, τ_∞ , compared with the mean free time of single specie, τ_{coll} . The parameters extrapolated from the power decay interpolations of $\tau_c^{He(Ne)} - \tau_{coll}^{He(Ne)}$ (see eq. 3.17) are also reported and compared with the temperatures relaxation time, τ_Δ .

collective rearrangements of local structure, described with macroscopic parameters of the system, while microscopic details are lost. The proposed expression for τ_c in the probed kinematic range is therefore:

$$\frac{\tau_c - \tau_{coll}^\alpha}{\tau_{Max}} = \frac{n_S^{-1}}{[Q \cdot (\lambda^\alpha - \lambda_0)]^2}. \quad (3.19)$$

3.4.6 Viscosity

In the viscoelastic framework for one-component system, the Q -dependent longitudinal viscosity is defined as:

$$\eta_L(Q) = \frac{Mn}{Q^2} NK^{-1}. \quad (3.20)$$

The definition is based on the comparison between the viscoelastic memory function and the hydrodynamic counterpart, that (neglecting the thermal contribution) is:

$$M_{hydro}(Q, t) = 2\Gamma Q^2 \delta(t) = \frac{\eta_L Q^2}{Mn} \delta(t), \quad (3.21)$$

being Γ the attenuation coefficient of sound waves and η_L the longitudinal viscosity. In the low Q limit the viscoelastic memory function should reach its hydrodynamic asymptote, i.e.:

$$\eta_L(Q) |_{Q \rightarrow 0} = \eta_L. \quad (3.22)$$

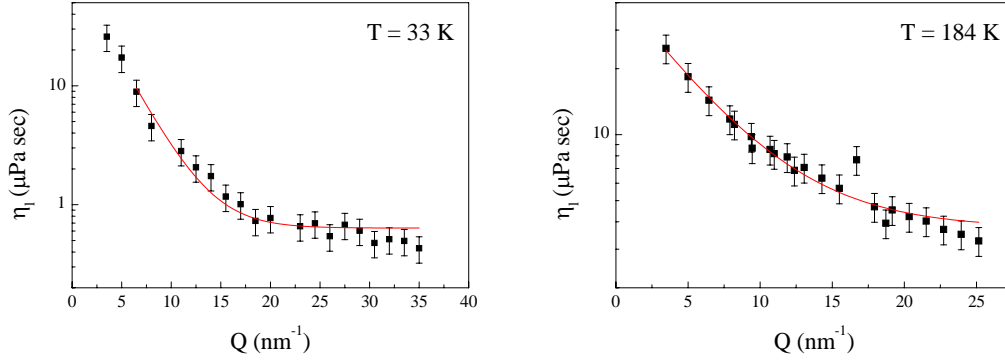


Figure 3.13: $\eta_L(Q)$ of He at $T = 184\text{ K}$, $n = 9.8\text{ nm}^{-3}$ (left graph) and at $T = 33\text{ K}$, $n = 27.5\text{ nm}^{-3}$ (right graph). The red solid lines are interpolations performed with an empiric exponential decay function.

For the *He* spectra at $T = 33\text{ K}$ and $T = 184\text{ K}$ the $\eta_L(Q)$ values are reported in fig. 3.13. The solid lines through the data are interpolations performed with an exponential decay function:

$$\eta_L(Q) = \eta_L e^{-\frac{Q}{Q_L}} + \eta_{L\infty}. \quad (3.23)$$

The values of η_L obtained from this interpolation are reported in tab. 3.2 and compared with those of the shear viscosity, η_S , obtained from the EoS and by direct calculation in the kinetic theory framework. The ratio of η_L/η_S well fits the general trend observed for simple liquids. This finding can be therefore considered as a further consistency check of the performed data analysis.

For a binary mixture the relationship between hydrodynamic quantities and memory function formalism is more complicated and, so far, not well assessed. The difficulties principally arise from the fact that in the hydrodynamic limit the sound propagation is related only to total density fluctuations, whereas in the mesoscopic regime a correct description of collective modes takes into account also kinetic modes that in the $Q \rightarrow 0$ limit have zero intensity. Nevertheless, the equivalent

3. The Helium/Neon mixtures from the mesoscopic to the single particle regimes

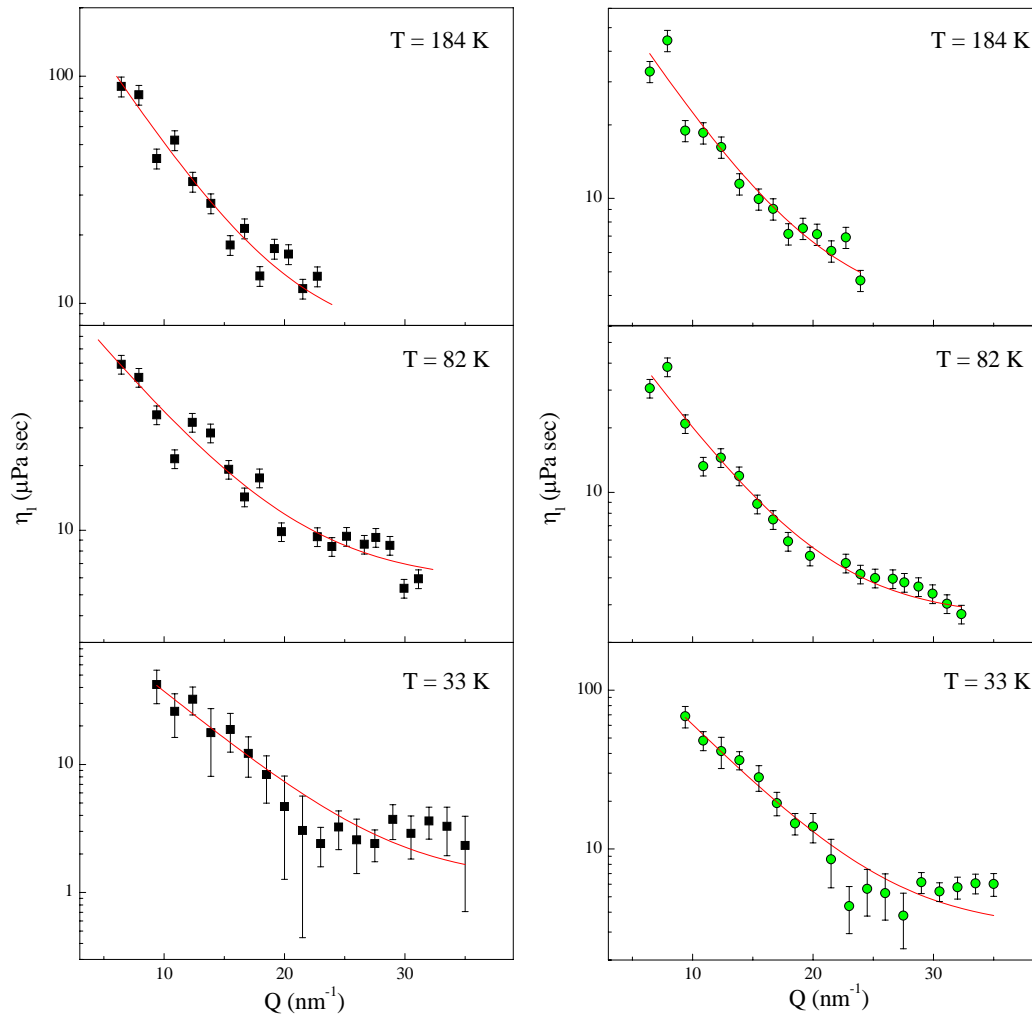


Figure 3.14: Diagonal elements $\eta_L^{HeHe}(Q)$ and $\eta_L^{NeNe}(Q)$ of the matrix $\eta_L(Q) \equiv \frac{Mn}{Q^2} \mathbf{N} \mathbf{K}^{-1}$. The red solid line are interpolations performed with an exponential decay function.

		$Q_L (nm^{-1})$	$\eta_L (\mu Pa sec)$	$\eta_S^{EoS} (\mu Pa sec)$
$T = 33 K$	<i>He</i>	6.1 ± 0.9	35 ± 8	10.5
$n = 27.5 nm^{-3}$				
$T = 184 K$	<i>He</i>	4.8 ± 0.3	42 ± 3	16.3
$n = 9.8 nm^{-3}$				
$T = 33 K$	<i>He</i>	5.6 ± 0.9	220 ± 60	16.1
$n = 34.4 nm^{-3}$	<i>Ne</i>	5.6 ± 0.5	340 ± 40	
$T = 82 K$	<i>He</i>	6.3 ± 0.9	150 ± 30	11.3
$n = 18.45 nm^{-3}$	<i>Ne</i>	5.6 ± 0.9	110 ± 30	
$T = 184 K$	<i>He</i>	5 ± 1	290 ± 70	14.9
$n = 12.2 nm^{-3}$	<i>Ne</i>	6 ± 2	110 ± 50	

Table 3.2: Parameters of eq.3.23. The extrapolated values of $\eta_L^{HeHe}(Q)$ and $\eta_L^{NeNe}(Q)$ are compared with the values of the shear viscosity, η_S^{EoS} , calculated by the EoS.

of 3.20 can be formally defined substituting the memory function moments with their matrix equivalent. The diagonal elements of the resulting matrix are plotted in fig.3.14 and compared with the *He* and *Ne* shear viscosity calculated in the kinetic theory framework and the total mixture viscosity estimated by EoS ⁴. As for the one component fluid the data are interpolated with an exponential decay function and the extrapolated parameters are reported in tab.3.2. Comparing abruptly the value of $\eta_L = \eta_L^{He} + \eta_L^{Ne}$ to η_S the discrepancy with the one-component system is evident: their ratio is two or three time bigger than the single fluid case. The attenuation coefficient of sound waves, Γ , of a neutral binary mixture in the hydrodynamic limit is reported in 1.91 and 1.92. Keeping off an exact treatment of the hydrodynamic memory function, a comparison between $\eta_L^{He} + \eta_L^{Ne}$ and Γ can be done. ⁵ The condition of material stability requires that $(\frac{\partial \mu}{\partial c})_{P,T} >$

⁴The viscosity for the mixtures is calculated exploiting the one-fluid approximation [70] and the results valid for Lennard-Jones fluids.

⁵A more correct approach could be to compare Γ with the density-density matrix element of $\tilde{\eta}(Q) = \frac{Mn}{Q^2} \mathbf{N}(\mathbf{Q}) \mathbf{K}(\mathbf{q})^{-1}$, where $\tilde{\mathbf{N}}$ and $\tilde{\mathbf{K}}$ are the forth and sixth moments of the memory function in the Bathia-Tornton representation. They can be obtained from $N(Q)$ and $K(Q)$ by considering that $\tilde{\omega}^n(Q) = \mathbf{X} \omega^n(Q) \mathbf{X}$.

0. Consequently the extra term in 1.91 to respect the single fluid equivalent is positive, so explaining the larger value of $\frac{\eta_L}{\eta_S}$ in binary system. Tab. 3.2 shows that $\eta_L(T = 184 K) > \eta_L(T = 82 K)$. This can be explained by the observation that the hydrodynamic viscosity in gaseous systems scales as $T^{1/2}$, as reported in the last column of tab. 3.2, and, moreover, the interdiffusion coefficient, D , scales as $T^{3/2}$. The particularly large value of the extrapolated η_L at $T = 33 K$ can be rather related to the demixing tendency of the analyzed mixture at low temperature. This is a general finding for He/Ne mixtures and is confirmed, for this specific case, by the low Q trend of the static structure factors (see 1.37 and 1.81). As a consequence at low temperatures $(\frac{\partial \mu}{\partial c})_{P,T} \rightarrow 0$, the extra contribution in 1.91 increases. However, even if the above arguments may qualitatively explain the large viscosity estimated for binary systems, it is rather evident how a more detailed analysis of the relation between lineshape parameters and viscosity is needed in order to draw a more reliable conclusions.

3.5 Single particle regime

In subsec. 3.4.4 has been remarked that for the $He_{0.8}Ne_{0.2}$ mixture at $n = 12.2 nm^{-3}$ and $T = 184 K$ the characteristic frequency of longitudinal mode for $Q \geq 20 nm^{-1}$ is consistent with that expected in the IA regime. This finding is validate in the following where the data acquired in the high Q region have been analyzed in the IA framework. The information one can obtained by an inelastic scattering study of a fluid in the IA regime is basically momentum distribution function $n(P)$ (sec. 1.4). In the case of a disparate mass binary mixture this kind of information, and more generally the analysis of $S(Q, \omega)$ in the IA region, is particularly useful because it can characterize the peculiar equilibration process described in the “two temperature theory” (see sec. 1.2.2.2 and sec. 3.4.5). For the specific case of $He_{0.8}Ne_{0.2}$ this theory has been successful applied to describe the behavior of re-

laxation time in the mesoscopic region. Aim of the following study is, then, to characterize the momentum distribution of this mixture with particular emphasis to its relationship with the “two temperature framework”.

In the probed Q range $25 \div 52 \text{ nm}^{-1}$ the condition of high- Q limit is fulfilled for both He and Ne particles, being $Q \cdot \lambda_{He}$ in the range $5.6 \div 14.6$ and $Q \cdot \lambda_{Ne}$ in the range $3.3 \div 8.5$. The short time hypothesis can be proved by assuming a Maxwell momentum distribution. The width of the momentum distribution is, therefore, supposed to be $\Delta P = 2\sqrt{\ln(2)}\sqrt{M_{He(Ne)}k_B T}$. The decay time, $\tau_D^{He(Ne)}$, of the $He(Ne)$ self-correlation function 1.182 is then compared with the respective Einstein frequencies ω_E^{He} and ω_E^{Ne} . These quantities can be taken as a measure of the typical interaction frequency between first neighbors and, consequently, used to estimate the oscillation frequency in eq. 1.183. The short time hypothesis result fulfilled in the above Q range, being $\omega_E^{He}\tau_D^{He} \sim \omega_E^{Ne}\tau_D^{Ne} \approx 0.9 \div 0.4$

The data acquired in the aforementioned Q range are therefore analyzed in the IA framework.

3.5.1 Data analysis

The general expression relating the raw data $I(Q, \omega)$ to $S^{ex}(Q, \omega)$ is supposed to be (see eq. 4.1):

$$I(Q, \omega) = I(Q)[S^{ex}(Q, \omega) \otimes R(Q, \omega)] + c(Q), \quad (3.24)$$

where the symbols are the same used in sec. 3.3. In the high Q limit the cross term $S^{12}(Q, \omega)$ is assumed equal to zero, also in view of the previously described data analysis. Therefore, $S^{ex}(Q, \omega)$ in the IA regime can be approximated by:

$$S^{ex}(Q, \omega) = x_{He}[f^{He}(Q)]^2 S_{IA}^{HeHe} + x_{Ne}[f^{Ne}(Q)]^2 S_{IA}^{NeNe}, \quad (3.25)$$

where $f^{He(Ne)}(Q)$ are defined as in subsec. 2.1.2.

The minimization routines employed was the same described in subsec. 3.3.

3. The Helium/Neon mixtures from the mesoscopic to the single particle regimes

The expression of the dynamical structure factor in the IA regime for a one-component system is reported in eqs. 1.180 and 1.181. The generalization to a binary system is straightforward:

$$S_{IA}^{\alpha\alpha}(Q, \omega) = \int d\mathbf{P} n^\alpha(P) \delta(\hbar\omega - \hbar\omega_r^\alpha - \mathbf{P} \cdot \hbar\mathbf{Q}), \quad (3.26)$$

where

$$\hbar\omega_r^\alpha = \frac{\hbar^2 Q^2}{2M_\alpha} \quad (3.27)$$

is the recoil energy of the specie α . If it is assumed that $n(P)$ is Maxwellian with temperature T , 3.26 reduces to:

$$S_{IA}^{\alpha\alpha}(Q, \omega) = \frac{e^{-\frac{(\omega - \omega_r^\alpha)^2}{2Q^2 k_B T / M}}}{Q \left(\frac{2\pi k_B T}{M_\alpha} \right)^{1/2}}, \quad (3.28)$$

which is represented by a Gaussian function centered in ω_r^α and of variance $\sigma_\alpha = Q\sqrt{k_B T / M_\alpha}$. This model function has been also applied to a fitting procedure on pure *He* spectra at $n = 9.8 \text{ nm}^{-3}$ and $T = 184 \text{ K}$ acquired in the Q range $8.2 \div 40.6 \text{ nm}^{-1}$. The expression in eq. 3.25 in this case assume the form:

$$S^{ex}(Q, \omega) \propto e^{-\frac{(\omega - \omega_r(Q))^2}{2\sigma(Q)^2}}. \quad (3.29)$$

The parameters $\omega_r(Q)$ and $\sigma(Q)$ have been kept free to vary in the fitting routines, together with the intensity factor $I(Q)$ and the background $c(Q)$. In fig. 3.15 raw IXS data at selected Q value (black circles) are reported with the best fit lineshape (red line). From the two parameters $\omega_r(Q)$ and $\sigma(Q)$ it is possible, in principle, to extrapolate the temperature of the system. However, it should be stressed that the zero of the energy scale in a given spectrum is dependent on the experimental condition. From the peculiar shape of $S(Q, \omega)$ in the IA it follows that, for a given spectra, there are no mean to identify the zero energy position from the spectrum, if $\omega_r(Q)$ is unknown. The more reliable information is therefore contained in the

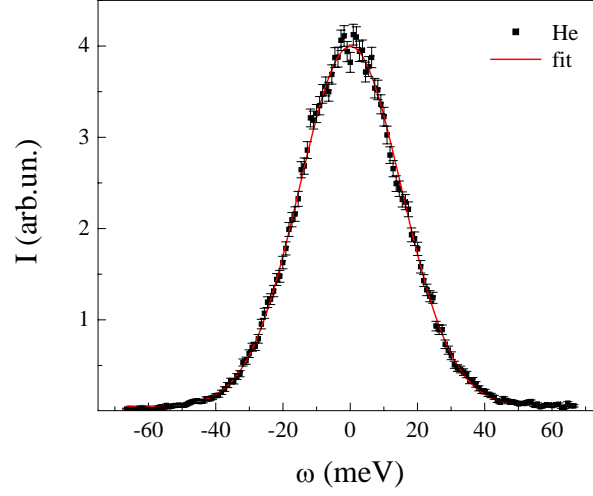


Figure 3.15: IXS spectrum at $Q = 36 \text{ nm}^{-1}$ of He at $T = 184 \text{ K}$ (black circles) with the best fit curve (red line). The model function is obtained hypothesizing a Maxwell momentum distribution to describe $S(Q, \omega)$ in the impulse approximation regime.

parameter $\sigma(Q)$. In fig. 3.16 is reported $\sigma^2(Q)$ vs. Q^2 . The black solid line is the ideal gas behavior calculated through the expression $\sigma(Q)^2 = Q^2 k_B T / M_{He}$, where T is fixed to the thermodynamic equilibrium value of 184 K . The green solid line represent the values of $\sigma^2(Q)$ where final state corrections to the IA have been taken into account [24]. These corrections, at the first order, can be expressed into the form:

$$\tilde{\sigma}(Q)^2 = Q^2 \frac{k_B T}{M} (1 - \Gamma(Q)), \quad \Gamma(Q) = \frac{0.4486}{Q \cdot \lambda}. \quad (3.30)$$

By comparing the experimental $\sigma(Q)^2$ values with theoretical predictions it can be concluded that: 1) the single particle regime is reached for $Q \geq 20 \text{ nm}^{-1}$, 2) in the Q interval between 20 and 30 nm^{-1} final state corrections have a non negligible weight, 3) at $Q \geq 30 \text{ nm}^{-1}$ final state corrections are less relevant and the $n(P)$ of the system is correctly described by a Maxwell distribution with macroscopic temperature $T = 184 \text{ K}$, i.e. the equilibrium distribution appropriate to a classical

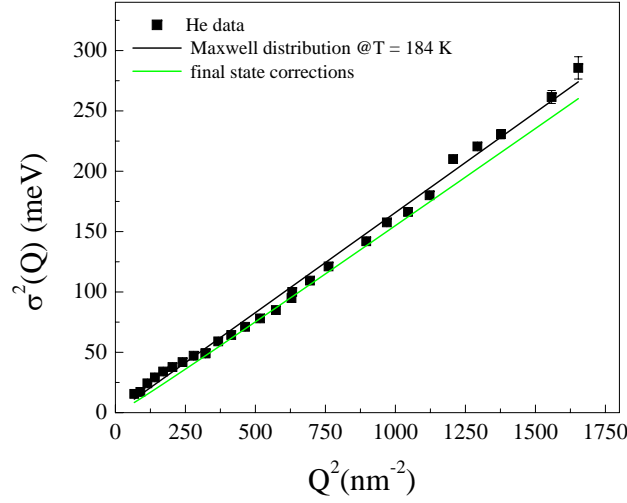


Figure 3.16: $\sigma^2(Q)$ (black squares) of He at $T = 184 K$ and $n = 9.76 nm^{-3}$. The solid lines are the theoretical estimation by assuming: 1) a Maxwellian momentum distribution function at the equilibrium temperature T (black line) and 2) a Maxwellian function plus final state corrections (green line).

system. In the case of binary system, the FZ representation is used again. In this case $S^{ex}(Q, \omega)$ can be written as:

$$S^{ex}(Q, \omega) = x_{He} [f^{He}(Q)]^2 e^{-\frac{(\omega - \Delta\omega_r(Q) - \omega_r^{Ne}(Q))^2}{2(\sigma^{He}(Q))^2}} + x_{Ne} [f^{Ne}(Q)]^2 e^{-\frac{(\omega - \omega_r^{Ne}(Q))^2}{2(\sigma^{Ne}(Q))^2}}, \quad (3.31)$$

where $\Delta\omega_r(Q) = \omega_r^{He}(Q) - \omega_r^{Ne}(Q)$ and $f^{He(Ne)}(Q)$ were kept fix during the minimization routine. A preliminary set of fit was performed leaving free in the minimization routine the parameters ω_r^{Ne} , $\Delta\omega_r$, $\sigma^{He}(Q)$ and $\sigma^{Ne}(Q)$. It was, however, observed that the extrapolated values of the parameter $\Delta\omega_r(Q)$ was well approximated, for all the probed wavevectors, by its theoretical prediction obtained assuming an ideal gas behavior. To this respect, it has to observe that the final state

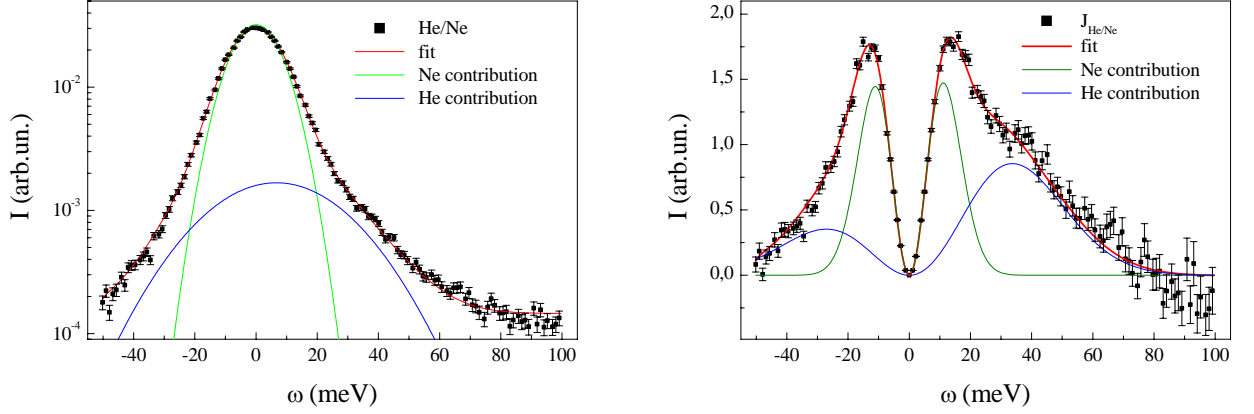


Figure 3.17: *Left graph:* IXS spectrum at $Q = 41 \text{ nm}^{-1}$ of $He_{0.8}Ne_{0.2}$ mixture at $T = 184 \text{ K}$ (black circles) with the best fit curve (red line). The model function is reported in eqs. 3.24 and 3.31. *Right graph:* corresponding $J(Q, \omega)$. The He contribution is more evident.

corrections to $\omega_r^{He(Ne)}$ can be expressed as:

$$\begin{aligned} \tilde{\omega}_r^{He(Ne)} &= \omega_r^{He(Ne)} (1 - \Phi(Q)^{He(Ne)}), \\ \Phi(Q)^{He(Ne)} &= 1.95 \left(\frac{10}{\sigma_{He(Ne)} \cdot Q} \right)^2 + O(Q^{-4}). \end{aligned} \quad (3.32)$$

The corrective term $\Phi(Q)^{He(Ne)}$ has been calculated following the treatment for Lennard-Jones (LJ) fluids [24] considering He and Ne LJ sphere diameters of $\sigma_{He} \approx 0.262 \text{ nm}$ and $\sigma_{Ne} \approx 0.279 \text{ nm}$ respectively [71]. The final state corrections to $\Delta\omega_r$ are, indeed, estimated to be less than 10% with respect to the ones of $\omega_r^{He(Ne)}$. Therefore, in the final fitting procedure the parameter $\Delta\omega_r(Q)$ was kept fix to its ideal gas value, i.e. $\frac{\hbar^2 Q^2}{2} \left(\frac{1}{M_{He}} - \frac{1}{M_{Ne}} \right)$. Raw IXS data with the relative best fit curves and instrumental resolutions are reported in fig. 3.17. The agreement between the model function and the experimental spectra is good for the whole analyzed Q range.

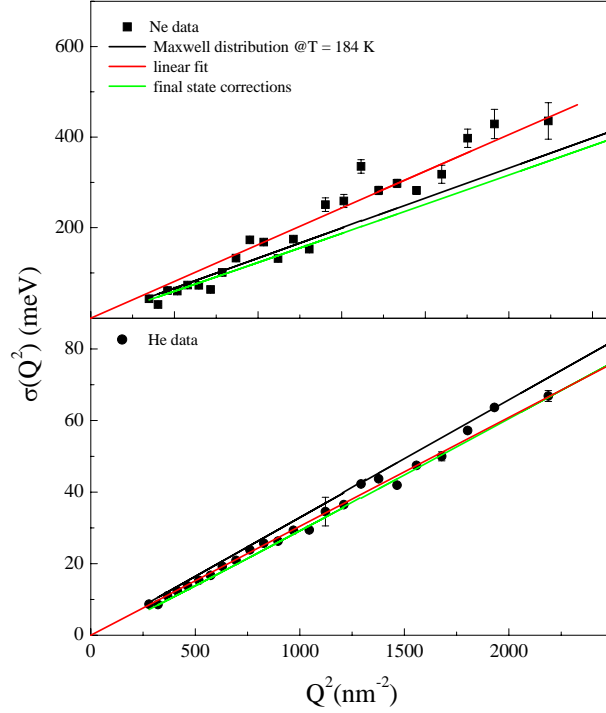


Figure 3.18: $\sigma(Q)$ of *He* and *Ne* as a function of Q^2 . The solid black lines are from theoretical estimation by assuming a Maxwellian momentum distribution function at the equilibrium temperature T . Green solid lines refer to final state corrections. Red solid lines are linear interpolations.

3.5.2 Experimental results

The extrapolated values of the parameters $[\sigma^{He}(Q)]^2$ and $[\sigma^{Ne}(Q)]^2$ vs. Q^2 are reported in fig. 3.18. As in the case of fluid *He*, the black solid line is the ideal gas behavior of $\sigma^2(Q)$ calculated assuming a Maxwell distribution where T is fixed to the thermodynamic equilibrium value of 184 K. The green solid line represent the values of $\sigma(Q)^2$ where final state corrections are considered. They have been calculated as reported in eq. 3.30 for a one-component system, where it was assumed $\lambda \equiv \lambda_{He(Ne)}$ for *He* and *Ne* respectively. The red solid line is a linear interpolation. The data reported in fig. 3.18 show that, for the subsystem of *Ne* particles, the IA region has been reached for $Q > 20 \text{ nm}^{-1}$. The value of $\sigma(Q)$ calculated assuming

a Maxwell distribution characterized by the equilibrium temperature T and taking into account final state corrections fit enough accurately the $\sigma(Q)$ data in all the probed Q range. In the case of the He subsystem, conversely, it is observed an anomalous behavior of $\sigma(Q)$ for $Q \geq 30 \text{ nm}^{-1}$. Its value is, in fact, systematically higher than that one estimated by a Maxwell distribution function with temperature T . As shown in figure, final state interactions cannot take into account this anomaly because they manifest in a narrowing of the gaussian function describing $S_{IA}(Q, \omega)$, i.e. they act in opposite direction. In order to fit experimental data a Maxwell distribution function with $T = 220 \pm 10 \text{ K}$, i.e. $\sim 40 \text{ K}$ higher than the macroscopic one, has to be supposed.

A qualitative interpretation of this result can be given in the framework of the previously introduced two temperature theory. Correlation functions in gaseous mixtures are related to the solutions of the linear Boltzmann equations describing the system. For a multicomponents system, the linear form of the Boltzmann equations results the following expression for the single particle momentum distribution function of specie α :

$$n^\alpha(\mathbf{P}, T_\alpha) = n_0^\alpha(\mathbf{P}, T_0)(1 + \psi_\alpha(\mathbf{P}, t)), \quad (3.33)$$

where $n_0^\alpha(\mathbf{P}, T_0)$ is the absolute Maxwellian characterized by the equilibrium temperature T_0 and ψ_α denotes the deviation of $n^\alpha(\mathbf{P})$ from absolute equilibrium. This deviation can lead to an overall shift of actual temperature, T_α , of subsystem of specie α with respect to T_0 . In a first approximation, if the decay time of the correlation function (see eq. 1.182) is larger than the equilibration time, i.e. if $\tau \geq \tau_\Delta$, it can be assumed that in eq. 3.26 $n^\alpha = n_0^\alpha$. On the other hand, if $\tau \ll \tau_\Delta$, deviations from the absolute equilibrium may be observed within the experimental timescale. The decay time τ can be estimated by using ΔP obtained from the absolute equilibrium momentum distribution. It results that in the explored Q region, τ^{Ne} ranges from 0.43 psec to 0.18 psec , and τ^{He} ranges from 0.19 psec to

3. The Helium/Neon mixtures from the mesoscopic to the single particle regimes

0.08 *psec*, whereas the temperature relaxation time is estimated to be (see sub-sec. 3.4.5) 0.92 *psec*. τ^{He} is one order of magnitude lower than τ_{Δ} , whereas τ^{Ne} is, except for the highest Q 's, of the same order as τ_{Δ} .

So far the “two temperature” theory has been applied to explain experimental data in the hydrodynamic or in the mesoscopic region but never in the IA limit. This investigation, conversely, points towards such a theory, being related to the equilibration process in a binary mixture, can be exploited also in the IA region. Moreover, it has been shown how a distribution of local equilibrium can be probed by inelastic scattering in the IA regime, if the decay time of the intermediate scattering function is enough short. Whenever, a deeper investigation to confirm these findings is required, in particular it is worth studying mixtures as a function of n_S , since the condition $n_S = 1$, should set the limit of applicability of the two temperature theory.

From hydrodynamic to kinetic modes: crossover region in molten *RbF*

This chapter reports on the Inelastic Neutron Scattering (INS) experiment performed on a prototype binary ionic mixture: molten *RbF* (melting temperature $\sim 1100\text{ K}$). The chosen sample was investigated in the momentum transfer (Q) range of $2 \div 11\text{ nm}^{-1}$, which corresponds to the transition from the hydrodynamic to the mesoscopic regime.

4.1 The INS experiment

The experiment was performed at the BRISP time of flight thermal neutron spectrometer of the Institut Laue-Langevin (Grenoble, France). The energy of incoming neutrons, E_i , was set at 54.1 meV by exploiting the Cu(1,1,1) Bragg reflection of the monochromator, which is able to provide an overall resolving power of $E_i/\Delta E_i \approx 40$. In time of flight neutron spectrometers all the Q and energy transfer, E , ranges accessible by the instrument for a given experimental geometry and E_i -value are simultaneously measured. In other words, the (Q, ω) -dependence of $S(Q, \omega)$ can be directly derived in all the (Q, ω) -range allowed for a given experimental configuration. However, the brilliance of typical neutron sources is so

low (several order of magnitude lower than a synchrotron source) that the time needed to acquire a full $S(Q, \omega)$ spectrum with good statistics was several days. The obtained $S(Q, \omega)$ spectrum was then binned in the Q parameter in order to obtain the E -dependence of $S(Q, \omega)$ at a given Q ¹. The final outcome was a set of 11 spectra separated by a constant offset of 1 nm^{-1} in the $2 \div 12 \text{ nm}^{-1}$ Q -range, which corresponds to a scattering angle range of $1 \div 15$ degrees (see also sec. 2.4 for further detail on the instrument). The statistical quality of the spectra is enough to observe in the same spectrum the basic features of two inelastic excitations for $Q > 4 \text{ nm}^{-1}$ (see fig. 4.2). However, the statistics of INS data is much lower than that of IXS ones, so that the data analysis performed on $He_{0.8}Ne_{0.2}$ and discussed in the previous chapter could not be successfully applied in the present case.

The high purity *RbF* sample (Sigma-Aldrich) was loaded in the *Nb* cell described in 2.5.3, which can provide outstanding corrosion and high temperature resistance. The sample loading was performed in a vacuum environment in order to avoid contamination, the *Nb* cell was then welded by using an electron beam welding technique (made by *KE-Technologie GmbH*). The sample cell was finally placed in a high temperature furnace able to reach 1900 K . The cell is equipped with *Nb* shielding and it was kept in vacuum ($\sim 10^{-6} \text{ mbar}$) environment in order to avoid thermal gradient and spurious scattering from air. The sample temperature was set to 1130 K (i.e., 50 K above the melting). The overall temperature stability was better than 5 K during all the experiment.

4.1.1 Ancillary measurements

As preliminary operation, the energy resolution curves, $R(Q, \omega)$, have been obtained by measuring the INS signal from a Vanadium slab at room temperature. At each Q the experimental resolution curve can be fitted with a Gaussian with

¹The software *LAMP* was exploited.

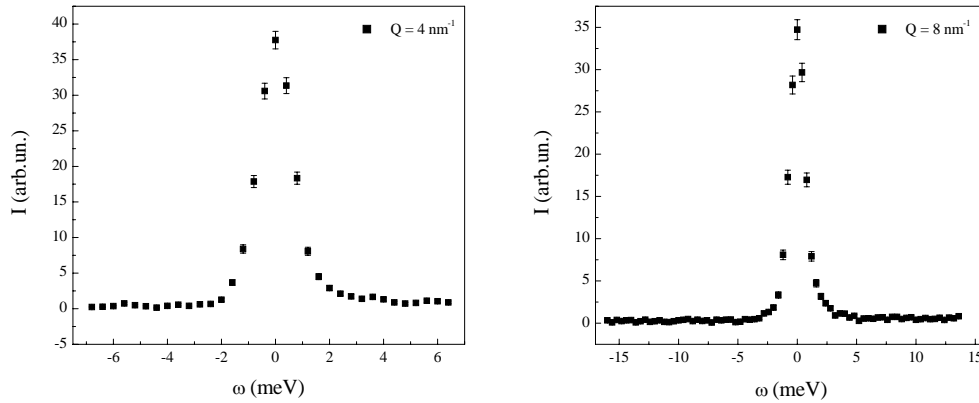


Figure 4.1: Selection of the resolution functions at the reported Q -values, as measured from a Vanadium slab.

$FWHM$ of about 1.8 meV . A selection of the measured resolution functions is shown in fig. 4.1.

At the selected incident neutron energy the INS signal scattered by the Nb cell and the furnace is not negligible. The empty cell contribution was, then, carefully normalized for the incident flux, detector efficiency and sample absorption (experimentally measured) and subtracted from the sample signal. To quantify the scattering from the furnace and empty cell INS measurements without sample have then been accomplished at the exploited experimental conditions. The acquisition time was set to be 40 hours, i.e. $\sim 2/3$ with respect to the sample measurement. Before empty cell signal subtraction, normalization of the sample and empty cell signals to counts of a proper monitor has been done.

4.1.2 Data analysis

Raw INS data, $I(Q, \omega)$, can be related to dynamic structure factors through the relation 4.1 only if empty cell and multiple scattering contributions have been properly considered. The empty cell contribution, $EC(Q, \omega)$, was subtracted from the measured signal, using the measured value of the transmission coefficient,

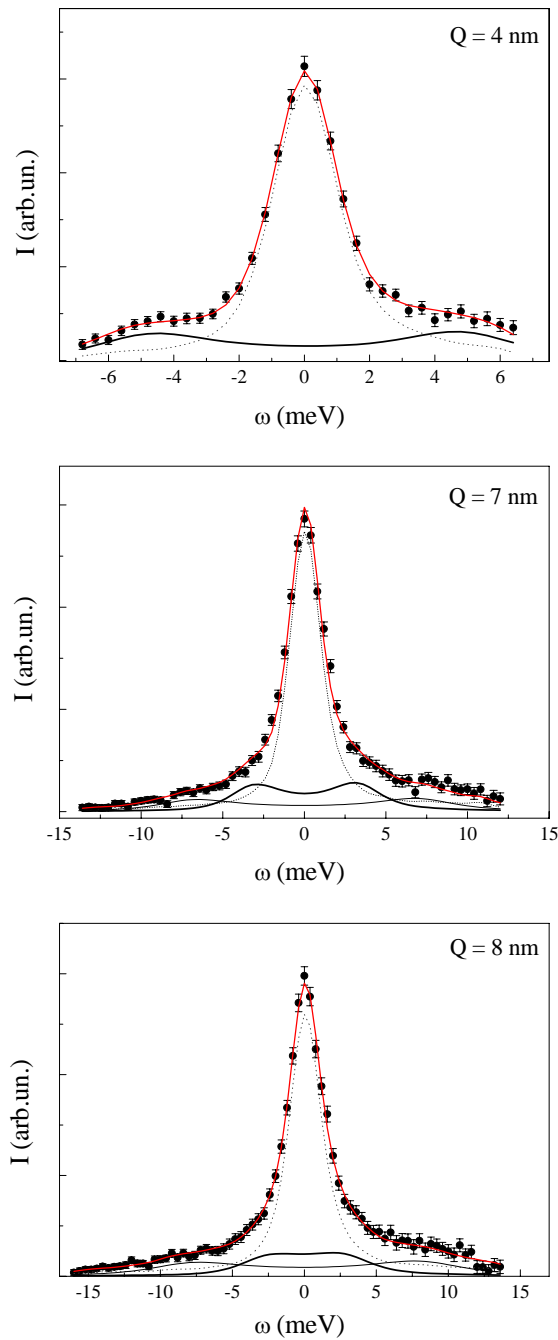


Figure 4.2: Selected INS spectra of molten RbF at the indicated k -values. The experimental data (full circles) and their error bars are shown together with the best fit function (red full line). The Lorentzian function (dashed line) and the DHO functions (black lines), which take into account the inelastic features are shown as well.

$T = 0.86$, at the given incident neutron energy:

$$I^0(Q, \omega) = I(Q, \omega) - T \cdot EC(Q, \omega). \quad (4.1)$$

Multiple scattering was computed evaluated employing an iterative Monte Carlo method [72], which uses as input the dynamic structure factors computed from Molecular Dynamics (MD) simulation performed with the rigid-ion model [73]. After multiple scattering subtraction ², the “raw” INS data, $I^1(Q, \omega)$, was analyzed using the same fitting procedure described in sec. 3.3, i.e.:

$$I^1(Q, \omega) = I(Q)[n(\omega, T)S^{ex}(Q, \omega) \otimes R(Q, \omega)] + c(Q), \quad (4.2)$$

where $n(\omega, T)$ is the Bose factor, $c(Q)$ is a flat background and $I(Q)$ is an overall intensity factor. As for the neutral mixture (3.3), the FZ representation has been chosen:

$$S^{ex}(Q, \omega) = \sum_{\alpha\beta=Rb,F} \sqrt{x_\alpha x_\beta} b_\alpha b_\beta S_{\alpha\beta}(Q, \omega), \quad (4.3)$$

where b_α is the coherent neutron scattering length of specie α . Since $x_{Rb} = x_F = 0.5$ and $b^{Rb}/b^F = 1.57$ it results that all $S^{\alpha\beta}$ have a similar weights in 4.3. The incoherent contribution to S^{ex} has been neglected because the incoherent to coherent cross sections ratios are very low, i.e.: $\sigma_{Rb}^{inc}/\sigma_{Rb}^{coh} = 0.08$ and $\sigma_F^{inc}/\sigma_F^{coh} = 0.0002$. It is possible to infer by inspecting the INS spectra reported in fig. 4.2 that for $Q > 4 \text{ nm}^{-1}$ two inelastic excitations can be distinguished. However, the statistics of experimental data did not permit to perform a viscoelastic analysis, as the one employed in the IXS experiment on neutral mixture (3.3). Therefore, it has been chosen, as empirical model function, the sum of a zero-centered Lorentzian function and two DHO functions (1.69):

$$S^{ex}(Q, \omega) = \sum_{i=1,2} I_{DHOi} \frac{\Omega_i^2 \Gamma_i}{[\omega^2 - \Omega_i^2]^2 + \omega^2 \Gamma_i^2} + I_L \frac{G_L}{G_L^2 + \omega^2}, \quad (4.4)$$

²As evidenced a posteriori by the data analysis the multiple scattering contribution were fairly negligible.

where Ω_i and Γ_i are the characteristic frequency and linewidth of inelastic excitations, G_L is the broadening of the quasi-elastic peak, while I_{DHO_i} and I_L are multiplicative factors. The data analysis consists in fitting procedure based on a standard minimization of the χ^2 , similar to that described in 3.3. The minimization was performed by the software MINUIT [74], employing two routines: a Nelder-Mead Simplex algorithm, and, if the correlation among the parameters was not too high, a successive refined search of the χ^2 minima using a gradient method (MIGRAD). The errors were calculated through the calculation of the covariance matrix. The parameters $I_{DHO_{1(2)}}$, $\Omega_{1(2)}$, $\Gamma_{1(2)}$, I_L , G_L , together with the background $c(Q)$ have been kept free to vary in the fitting routines. For Q values lower than 4 nm^{-1} , I_{DHO_2} was found to be consistent with zero, and therefore only one DHO function was used. The employed model function accurately describes experimental data in the whole Q -range, as can be evidenced from fig. 4.2, where a selection of INS spectra are reported together with the corresponding best fit results.

4.1.3 Experimental results

Fig. 4.3 reports the Q dispersion of $\Omega_{1(2)}$, $\Gamma_{1(2)}$ and G_L as extrapolated from the fitting procedure.

It can be clearly observed how in the probed Q -range both Ω_1 and Ω_2 have a linear Q dispersion which can be associated to a constant propagation velocity of $1890 \pm 70 \text{ m/sec}$ and $720 \pm 70 \text{ m/sec}$, respectively. A rough estimation of the adiabatic sound velocity gives $c_s \simeq 1450 \text{ m/sec}$ ³, i.e. a value in between the propagation velocities of the experimentally observed collective excitations. The accuracy of the given estimation, however, doesn't permit, however, to reject the

³The adiabatic sound velocity was estimated through the relation $c_s = \sqrt{\frac{\gamma k_B T}{m S(0)}}$, where it is assumed $\gamma \sim 1$ and $m = x_{Rb} M_{Rb} + x_F M_F$, while $S(0) \equiv S_{nn}(0)$ has been extrapolated from rigid-ion MD simulations [75].

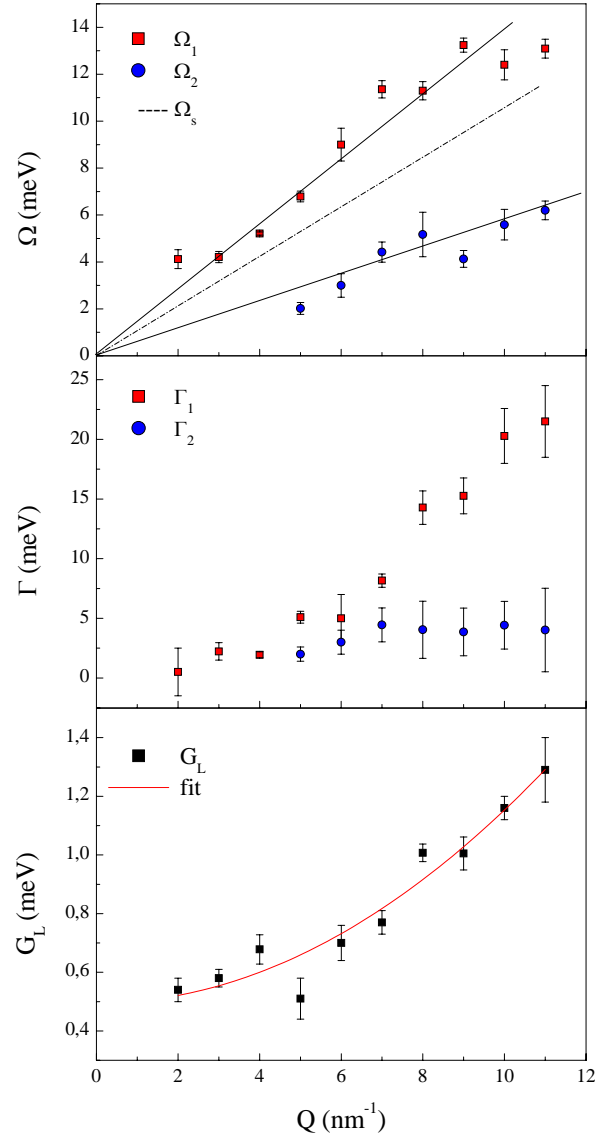


Figure 4.3: *Upper panel.* Dispersion relations of high-frequency and low-frequency collective mode, as derived from the analysis of INS spectra. It is also displayed the Q dispersion of the estimated adiabatic sound velocity, Ω_s . *Middle panel.* Value of the parameters Γ corresponding to DHO functions fitting the two excitations. *Lower panel.* Width, $G_L(Q)$, of the Lorentzian exploited in the fit model function to describe the contribution of the central peak of the spectra. The red full line is a parabolic curve fit.

hypothesis that to the higher frequency mode can be associated a velocity propagation equal to c_s . The inverse of the mixture average mean free path ⁴ was estimated to be 12 nm^{-1} . Therefore, in all the probed Q region the condition $Q \cdot \lambda < 1$ is fulfilled. In such a condition, if the ionic binary mixture is in the Kubo regime, an optic-like branch associated to charge fluctuations collective mode should appear at frequencies near the plasma frequency, Ω_P (see sec. 1.3.3). The estimated value for Ω_P is 28.3 meV , i.e. well above the characteristic frequencies of both observed collective modes. This fact, together with the observed linear Q dispersion of both modes permit to rule out the hypothesis that an optic-like mode is observed in the probed kinematic plane. Therefore, also in view of the observed Q -dispersion, it may ascribed to both high and low frequency mode an acoustic nature. Moreover, since the propagation velocity of high and low frequency branch is higher and lower than c_s , respectively, one can tentatively associate the observed behavior to a dynamical decoupling characterizing the fast and slow sound phenomenology, in analogy with previous results obtained in non-ionic mixtures. In the next section it will be shown how the phenomenology of neutral binary mixtures can be applied to the particular case of molten *RbF*. Unfortunately, the limited instrumental energy resolution does not permit to discriminate if the low-frequency mode has, at $Q < 4 \text{ nm}^{-1}$, a propagation gap or if it merges into the higher frequency branch. It is to observe, however, that the parameters $G_1(Q)$ doesn't show any discontinuity in low- Q trend, so partially supporting the first hypothesis.

4.1.3.1 A ionic mixture in the two-component regime?

More insights on a possible dynamical decoupling can be gained from the analysis of G_L . As assessed in 1.136, a peculiarity of ionic binary mixtures, directly related to

⁴It is defined as the Enskog mean free path $\lambda = (\sqrt{2}\pi n\sigma^2)^{-1}$ of an equivalent monoatomic fluid with number density $n = n_F + n_{Rb} = 33 \text{ nm}^{-3}$ and atomic diameter $\sigma = (x_F\sigma_F^3 + x_{Rb}\sigma_{Rb}^3)^{1/3} = 0.142 \text{ nm}$, being $\sigma_{F(Rb)}$ the ionic diameters.

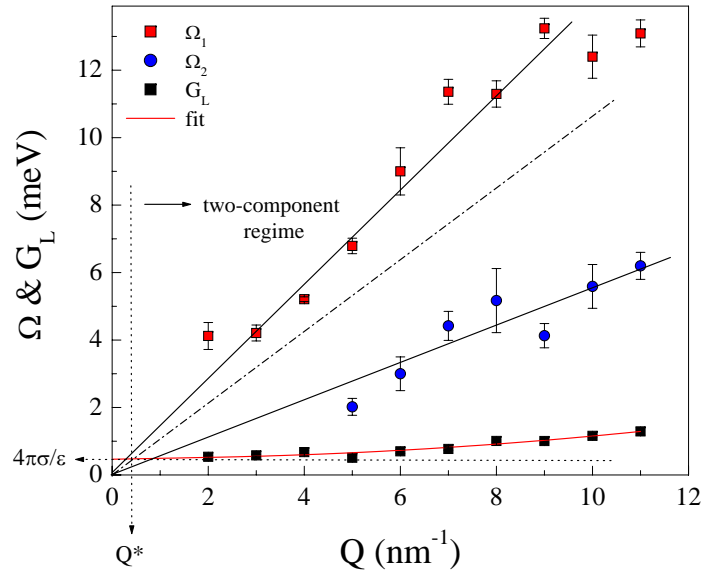


Figure 4.4: The Q dispersion of the estimated adiabatic sound velocity and of the two observed collective mode is compared with the $Q = 0$ extrapolated value of $G_L(Q)$, i.e. G_0 . This last quantity can be identified with $4\pi\sigma/\epsilon$. The condition $4\pi\sigma/\epsilon \ll \Omega_s$, which define the range of validity of the two-component regime, is always fulfilled in the Q range probed by the INS experiment.

the properties of the Coulomb potential, is that the central line width of $S_{ij}(Q, \omega)$ is different from zero for $Q \rightarrow 0$, as it is the case for neutral systems, but is equal to $4\pi\sigma/\epsilon$. At higher Q , a Q^2 dependence is expected. The polynomial law: $G_{L0} + G_{L1}Q^2$ well describe the observed trend of G_L and allows extrapolating the $Q \rightarrow 0$ limit, G_{L0} (see the lower panel of fig. 4.3). Assuming that $G_{L0} = 4\pi\sigma/\epsilon$, a quite low value (0.49 ± 0.06 meV) of this last quantity is found for molten *RbF*, if compared with typical value for molten salt (~ 5 meV) [76]. In fig. 4.4 $G_L(Q)$ is plotted together with $\Omega_{1(2)}(Q)$ and $\Omega_s = c_s Q$. It is possible to infer that in the probed Q range the condition $4\pi\sigma/\epsilon \ll c_s Q$ is always fulfilled, and then it is expected that the two-component regime for a molten salt is reached. Consequently, a simple data interpretation focused on the treatment based on the hypothesis of decoupling between charge and mass-density or temperature fluctuations (Kubo regime), described in sec. 1.3.3, seems not appropriate. Possible explanation of two acoustic modes with linear Q -dispersion in the region $Q \cdot \lambda < 1$ and with characteristic frequency lower and higher, respectively, than the adiabatic one (both of them well below the plasma frequency), can be found hypothesizing that the ionic system has, in its two-component regime, a behavior similar to that of neutral system. In fact, as reported in 1.2.2.3, if the condition $\omega(4\pi\sigma/\epsilon c_s) \gg \xi_i$ ⁵, is fulfilled the ‘‘hydrodynamic’’ description of fast and slow sound mode could in principle be applied. The observed phenomenology can be, thus, interpreted in terms of sound decoupling phenomena characteristic of binary neutral mixtures.

The static electrical conductivity is related to the electric-current autocorrelation function $J^z(t)$, through the relation:

$$\sigma = \frac{e^2}{k_B T V} \int_0^\infty J^z(t) dt = \frac{e^2}{k_B T V} \int_0^\infty \sum_{\alpha=1,N} \sum_{\beta=j,N} \langle z_i \mathbf{v}_\alpha(\mathbf{r}, t) \mathbf{v}_\beta(\mathbf{r}, t) \rangle dt. \quad (4.5)$$

If the self-correlation term ($i = j$) are separated from the cross term ($i \neq j$), 4.5

⁵ ξ is defined by the expression 1.135

reduces to:

$$\sigma = \frac{e^2}{k_B T} \rho (1 - \Theta) \sum_{\alpha=1,2} x_{\alpha} z_{\alpha} D_{\alpha}, \quad (4.6)$$

where D_{α} is the self-diffusion coefficient of the specie α . The value of the deviation factor Θ is a measure of the relevance of the cross correlation term. In the case of alkali halides Θ is different from zero and always positive [25]. The positive value of Θ means that the motion of a pair of oppositely charged particles is in the same direction and contributes to self-diffusion but not to electrical conduction. A high value of Θ , related to such physical mechanism and then to the behavior of the pair interaction potential, can be responsible of a lowering the value of σ . With the aim to corroborate the above frame, a more reliable estimation of the electrical conductivity is demanding. In fact the extrapolation from the central line width of the spectra can be trust only by an empirical point of view. In fact all the contribution coming from different relaxation phenomena and from different dynamic structure factors have been ‘‘averaged’’ in the power law expression used to interpolate experimental data. A possible way is to exploiting MD simulations to calculate the expression 4.5.

4.1.3.2 Thermal fluctuations kinetic mode and GCM approach

An alternative interpretation of the experimental results obtained can be done in the framework of the Generalized Collective Mode (GCM) approach. It consists of parameter-free analysis of time correlation function derived by MD simulations. In such an approach the solution of the Generalized Langevin Equation of motion (eq. 1.141) is given, within the Markovian approximation, in terms of the eigenvalues and eigenvectors of the generalized hydrodynamic matrix:

$$\mathbf{T}(Q) = \mathbf{F}(Q, t = 0) \cdot [\tilde{\mathbf{F}}(Q, z = 0)]^{-1}, \quad (4.7)$$

where $\mathbf{F}(Q, t)$ is the matrix of the time correlation functions, constructed on a suitable basis set of M dynamical variables $\mathbf{A}^{(M)}(Q, t) = \{A_1(Q, t), \dots, A_M(Q, t)\}$.

The choice of the dynamical variables is done, on general ground, by considering the set of hydrodynamic variables and their time derivative, which are supposed to describe correctly short time processes. In the case of longitudinal dynamics of binary mixtures, it is convenient to choose a set of eight dynamical variables, accounting for the most important microscopic processes: three variables $\{n(Q, t), J(Q, t), \frac{\partial J(Q, t)}{\partial t}\}$ which describe viscoelastic properties, $A_e^{(3)}(Q, t) = \{c(Q, t), J_c(Q, t), \frac{\partial J_c(Q, t)}{\partial t}\}$ which account for the mass-concentration dynamics and two variables $A_e^{(2)}(Q, t) = \{e(Q, t), \frac{\partial e(Q, t)}{\partial t}\}$ which describe energy fluctuations. Since total density and mass-concentration can be represented as linear combinations of partial densities, the first six variables can be changed with the corresponding partial dynamical variables without changing the eigenvalues of $\mathbf{T}(Q)$. The definition of the Q -dependent elements of $\mathbf{T}(Q)$ requires the knowledge of $t = 0$ values of time correlation functions, $F_{ij}(Q, 0)$, as well as the correlation times of the kind $\tau_{ij} = \frac{\int_0^\infty F_{ij}(Q, t) dt}{F_{ij}(Q, 0)}$ with $i, j = n, c, e$ [6], which are the input of the GCM analysis. These quantities are usually calculated through *MD* simulations. As general result for molten salts, three branches of propagating longitudinal modes are reported [28–30]. They are:

- a low-frequency branch corresponding to heat wave. It has a propagation gap in the long-wavelength range⁶ while in the Q region where its characteristic frequency is different from zero, it shows an almost linear Q dispersion.
- A second branch, located at higher frequencies and dispersing following an almost linear law, which accounts for longitudinal acoustic excitations.
- A high-frequency branch, located in a frequency region $\sim \Omega_P$ at $Q \rightarrow 0$ and well separated by the other two modes by a frequency gap. This mode is associated to an optic-like mode of kinetic nature, which cannot be observed

⁶For *NaCl* the propagation gap is at Q lower than 5 nm^{-1} .

in the hydrodynamic limit.

In the GCM approach it's possible to estimate the contribution of each mode to the partial dynamic structure factors. Comparing the dispersions of collective modes of RbF obtained by INS experiment (fig. 4.3) with the general insights obtained by the GCM approach, one can pose the following hypothesis: the lowest-frequency branch observed in the INS experiment can be referred to propagating kinetic mode associated to thermal fluctuations (heat waves), whereas the high frequency branch is related to longitudinal sound dispersion. The optic-like collective mode predicted by GCM theory is not observable in the INS experiment due to kinematic limitations. In order to observe the eventual presence of this optic-like mode, one can plain to perform an IXS experiment which is not affected by kinematic limitations.

Conclusions

In this thesis work we investigated the collective dynamics in two prototype binary mixtures: $He_{0.8}Ne_{0.2}$ and molten RbF , which can be regarded as archetypes of neutral and ionic systems, respectively. The differences in the behavior of these two kind of samples can be basically associated with the long range nature of Coulomb potential. An extensive review of some theoretical frameworks used to describe dynamics in neutral and ionic binary mixture is presented in Chapter 1. The energy spectra of density fluctuations, $S(Q, \omega)$, of $He_{0.8}Ne_{0.2}$ sample were collected by Inelastic X-ray Scattering (IXS) technique as a function of momentum transfer ($Q = 5 \div 50 \text{ nm}^{-1}$) in correspondence to three distinct thermodynamic states, ranging from liquid-like to gas-like temperature and density values. The exploited Q -range was enough large to allowed us probing both the so-called “mesoscopic” and “impulsive approximation” (IA) regimes. Experimental data on molten RbF were instead collected using Inelastic Neutron Scattering (INS) technique. The employed time of flight spectrometer allowed us to measure the Q -region ($2 \div 12 \text{ nm}^{-1}$) across the transition between the hydrodynamic and the mesoscopic regime. Further details on IXS and INS techniques and spectrometers, as well as on the various sample environments we used for performing the aforementioned experiments are reported in Chapter 2.

IXS spectra from $He_{0.8}Ne_{0.2}$ mixture in the mesoscopic regime ($Q < 30 \text{ nm}^{-1}$)

have been analyzed through a generalization to binary systems of the viscoelastic model derived within the memory function frame [20]. So far, this model has been largely used to describe $S(Q, \omega)$ of single-component systems in such a regime, but it was never applied in the analysis of experimental data of multi-component systems. For sake of simplicity and in order to not introduce too many free parameters in the fitting procedure, a model based on a single time decay of memory function was proposed. However, the correlations between fitting parameters were quite high and, therefore, we decided to further reduce the free parameters by relating the matrix of relaxation time with to the spectra momenta, which, in turns, were derived by the other fitting parameters. The employed relation was also used to estimate the relaxation time in pure He at the equivalent mixture density and at the same temperature. In this case the obtained results show a remarkable agreement with data directly derived from a parallel fitting procedure of IXS spectra in which the relaxation time was treated as a free parameter, and thus supporting the correctness of the data analysis. Further positive consistency checks were achieved by comparing the partial static structure factors with the results computer simulations, performed to this purpose, and by the comparing the experimental values of infinite frequency sound velocity with the estimations obtained from the calculation of the Einstein frequency. As a matter of fact, the proposed model accurately described the experimental data in all the exploited thermodynamic conditions and the obtained results for fitting parameters were quite reasonable. We can then assess that the first result of this thesis work was to demonstrate the reliability of a the proposed model function, which is used for the first time to fit experimental data from binary mixtures. This data analysis strategy permitted to derive: 1) the partial dynamic structure factors from the measured spectrum and, therefore, the associated spectra of the longitudinal current correlation functions. 2) The characteristic frequencies of collective excita-

tions, which can be straightforwardly obtained by longitudinal current spectra. 3) The relaxation parameters associated to both mixture components, i.e. the zero and infinite frequency sound velocities (c_0 and c_∞) and the relaxation times (τ_c), characterizing the microscopic dynamics in binary mixture.

The analysis of the partial dynamic structure factors and of the characteristic frequencies of collective excitations revealed the existence of different modes, having a different nature depending on the probed Q -range. In particular, for low $Q\lambda$ -values, being λ the average mixture mean free path, we observed: 1) a low-frequency mode which can be associated to a longitudinal acoustic mode of the whole system. In fact, both *He* and *Ne* current correlation functions show a peak at the same frequency. Moreover, in this frequency range the cross current correlation function is positive, thus indicating in-phase motion of *He* and *Ne* particle. The characteristic frequency of this mode is close to the adiabatic expectations. 2) An high-frequency mode, supported prevalently by partial density fluctuations of lighter element, i.e. *He*. For this mode the cross current correlation function suggests a counter-phase motion, thus indicating an optic-like character. 3) A very-low-frequency mode common to both specie and associated with counter-phase motion. Its characteristic frequency is consistent with the inverse interdiffusion time, therefore suggesting a diffusive nature of the mode. For $Q\lambda \approx 1$ the high-frequency optic-like mode is still present with the same feature, while the acoustic-like mode involving both specie tends to disappear. Concurrently, the interdiffusion mode becomes the dominant feature in the *Ne* spectrum and its weight in the *He* spectra also increase as well. Finally, in the high $Q\lambda$ -region the *He* and *Ne* dynamics is completely decoupled. The partial dynamic structure factors are, moreover, reaching their single particle limit.

Concerning the behavior of the other fitting parameter at a give thermodynamic condition, we found that their Q -dependencies can be parameterized by

using the mean free path associated to single specie components, λ^α . In particular, we found for both mixture components a qualitatively common trend of τ_c consisting in a low- Q increase of τ_c with respect to an high frequency asymptote identifiable with the average mean free time between intermolecular collisions, τ_{coll}^α . The observed deviations of τ_c with respect to τ_{coll}^α can be quantitatively cast in the same trend if reported as a function of $Q\lambda^\alpha$. A further common trend of τ_c data corresponding to different thermodynamic conditions can be obtained if we introduce the Maxwellization time, τ_{Max} , which provides a quantitative estimation of the characteristic time needed for the two species subsystems in order to reach the (microscopic) Maxwellian momentum distribution. As a result we found the following empirical expression for the relaxation time:

$$\frac{\tau_c^\alpha - \tau_{coll}^\alpha}{\tau_{Max}} = \frac{n_S^{-1}}{[Q \cdot (\lambda^\alpha - \lambda_0)]^2}, \quad (4.8)$$

where the suffix $\alpha = He, Ne$ labels the two species. The above expression emphasizes how a simple kinetic description seems to be satisfactory describe the relaxation dynamics of the system. This result was interpreted in the frame of the “two temperature” theory. This approach is based on the assumption that in disparate mass binary mixtures inefficient kinetic energy exchanges basically induce a two step process for the relaxation of density fluctuations towards the thermodynamic equilibrium. These processes are characterized by two distinct timescales: 1) the intra-specie collision time, τ_{coll}^α , where the each specie subsystem reaches a condition of “local” thermodynamic equilibrium associated with a temperature, T^α and 2) a characteristic time, τ_Δ , for the equilibration of the microscopic temperatures to the equilibrium temperature T through inter-specie collisions. Indeed, our results assert that in the high $Q\lambda^\alpha$ -range the physical mechanism responsible for the relaxation process is essentially the intermolecular intra-specie collision time. This implies that intermolecular interactions based on intra-species collisions are

quite ineffective. Therefore, in such a high- Q region the kinetic energy exchanges are inefficient, in agreement with the “two temperature” theory. On the other hand, on increasing Q the interactions between particles of different species become important in describing the relaxation process⁷. Since the Q^{-2} -behavior of relaxation time is usually associated with a diffusive dynamics, the $(Q\lambda^\alpha)^{-2}$ factor can be qualitatively regarded as a contribution to the relaxation time coming from the energy exchanges, essentially based on diffusive dynamics, between the two subsets corresponding to the two species. According to the “two-temperature” theory this relaxation process should be connected to the relaxation of the (microscopic) temperature differences between subsets. The characteristic timescale for this process, i.e. τ_Δ , is indeed related to $\tau_{Max} = n_S^{-1}\tau_\Delta$, which is the scaling quantity we used to obtain the common trend reported in the above equation. In summary, exploiting the basic ideas behind the “two temperature” theory we can suppose that the observed deviation of τ_c with respect to τ_{coll} is related with an equilibration process consisting in a temperature equalization of the two specie subset. This process cannot be observed in the hydrodynamic limit, i.e. when the period of acoustic wave perturbing the system is much lower than τ_Δ^{-1} . Moreover, on lowering the probed (Q, ω) -range dynamics related to the structural relaxation process is expected to dominate the decay of density fluctuations. These dynamics involve intermolecular correlations among a large number of particles leading to continuous rearrangements of local structures. In this respect, the empirical parameter $\lambda_0 \sim 4 \lambda$ can be regarded as the characteristic length scale for the breakdown of the observed “two temperature” phenomenology. A further corroboration of the above picture can be found from the analysis of IXS spectra of low density $He_{0.8}Ne_{0.2}$ sample ($T = 184 K$ and $n = 12.2 nm^{-3}$) collected at $Q = 30 \div 50 nm^{-1}$. In this case the experimental data can be analyzed with the frame of the Impulsive Approx-

⁷Kinetic energy exchange becomes more efficient increasing the number of collisions.

imation (IA), which allowed extrapolating the momentum distribution functions of the specie subsets. As a results, an anomalous behavior has been noticed on the He momentum distribution function. In particular, the apparent temperature ($T = 220 \pm 10 K$) associated with this distribution function is $\sim 40 K$ higher than the macroscopic one. This striking result can be straightforwardly interpreted as a fingerprint of the peculiar “two temperature” equilibration process. In fact, in the case of the He particles subset the decay time of the partial density self-correlation function (1.177), from which the experimental momentum distribution is extrapolated, is much shorter than τ_{Δ} ⁸. One can therefore infer that, in this case, we are directly probing the momentum distribution corresponding to the “local” equilibrium of He subset, while temperatures equilibration of the entire system is not yet accomplished.

The second part of this work has been dedicated to the study of molten RbF . The aim of this experiment was to characterize the role of Coulomb potential on collective dynamics at the transition from hydrodynamic to mesoscopic region. As described in sec. 1.2.2.3, it is possible to individuate two Q -ranges as function of the relative values of electrical conductivity, σ , and adiabatic sound velocity, c_s , characterized by a different lineshape of $S(Q, \omega)$. Specifically, if $4\pi\sigma/\epsilon \gg c_s Q$ the so-called Kubo regime is met. Here concentration and density/temperature fluctuations are decoupled. The collective modes associated to the latter variables are analogous to the ones of one-component fluid, while concentration fluctuations give rise to an optic-like kinetic mode with a characteristic frequency close to the plasma frequency, Ω_P , and with an intensity which vanishes in the hydrodynamic, $Q \rightarrow 0$, limit [25]. On the other hand, the condition $4\pi\sigma/\epsilon \ll c_s Q$ characterize the so-called two-component regime. Here the behavior of ionic mixtures becomes isomorphous to that of non-ionic ones, with electric conduction playing the role of

⁸This is not the case for the Ne particles subset.

interdiffusion. With typical values for molten salts, i.e. $4\pi\sigma/\epsilon \sim 5 \text{ meV}$ and $c_s \sim 1 \text{ meV/nm}^{-1}$, one finds that the Q -value for this transition is located at around 10 nm^{-1} . At such Q -range the mesoscopic regime is usually reached, so that the crossover between classical hydrodynamics and mesoscopic region usually belongs into the Kubo regime. Therefore, the presence of the optic-like kinetic mode is usually observed in this crossover region. However, if the electrical conductivity of the studied ionic mixture is particularly low, the transition from the Kubo to the two-component regimes can fall before that the mesoscopic region is met. In this case one can argue that the behavior of ionic and non-ionic mixtures at the transition from the hydrodynamic and the mesoscopic regime is the same, provided that the transport coefficients are redefined properly in order to account for the role of electric conductivity.

The INS data on molten RbF cover the Q -range from 2 to 12 nm^{-1} . The results obtained can be synthesized in what reported in the following. In view of the rather poor statistics of these data with respect to the $\text{He}_{0.8}\text{Ne}_{0.2}$ IXS data we could not perform the lineshape analysis based on the memory function formalism. We then decided to employ a simpler model function, which consists in a sum of a Lorentian function centered at zero energy transfer and two damped harmonic oscillator functions accounting for the inelastic excitations. This kind of data analysis allowed us to identify the simultaneous presence of two dispersive collective modes for $Q > 4 \text{ nm}^{-1}$ and to determine their characteristic frequencies. For lower Q 's the limitation imposed by the resolution function did not allow us to follow the evolution of the low frequency mode. Therefore, we cannot assess if it disappears from the spectrum or if it merges into the high frequency branch. Nevertheless, in the probed Q -range we clearly observed a linear Q -dispersion for both modes. Moreover, the energy transfer range ($1 \div 10 \text{ meV}$) where these excitations are observed is situated well below the estimated value of Ω_P , which is

largely above 20 meV . This definitively rules out the possibility that any of the two observed mode has a kinetic optic-like nature. An acoustic-like character for both modes can be therefore postulated. Finally, the sound velocities associated to the high and low frequency modes are higher and lower than the estimated value of c_s , respectively. The employed analysis also permitted to derive the Q -dependence of the central peak broadening, $G_L(Q)$. This was found to be well described by a constant term plus a parabolic trend: i.e., $G_L(Q) = G_{L0} + G_{L1}Q^2$. Since G_{L0} corresponds to the $Q \rightarrow 0$ value of $G_L(Q)$, it can be identified with the quantity $4\pi\sigma/\epsilon$. Indeed, a quite low value ($0.49 \pm 0.06 \text{ meV}$) of G_{L0} was found, as compared with typical values of molten salts. The comparison between the extrapolated $4\pi\sigma/\epsilon$ -value and the quantity $c_s Q$ suggests that in the probed Q -range we are already in the two-component regime. The observed phenomenology can be thus interpreted in terms of double sound propagation phenomenon, already observed in rarefied non-ionic gaseous mixtures [3, 77, 78]. This effect originates two distinct branches of longitudinal acoustic modes, also referred to as fast and slow sound modes, each one associated with a given specie.

However, we have to remark that the determination of $4\pi\sigma/\epsilon$ from the width of quasi-elastic peak can be done only via an empirical approach. In fact, all the contributions, coming from different relaxation phenomena and from different dynamic structure factors, have been “averaged” in the power law expression used to interpolate experimental data. A more accurate determination should come from independent measurements or calculations, which are actually in progress. Finally, we also highlight how an alternative interpretation of these experimental results can be qualitatively provided within the frame of the generalized collective mode approach. In this case the high frequency mode is identified with the extension of the adiabatic longitudinal sound mode beyond the hydrodynamic limit that, in analogy to what observed in several fluids, follows a linear dispersion with an

associated sound velocity larger than c_s . The low frequency mode could be instead associated with a propagating kinetic mode related to energy fluctuations (heat waves). The presence of heat waves in the $S(Q, \omega)$ was indeed predicted for other molten salts, e.g. molten NaCl, by generalized collective mode framework.

Bibliography

- [1] Bosse, J., Jacucci, G., Ronchetti, M., and Schirmacher, W. *Phys. Rev. Lett.* **57**, 3277 (1986).
- [2] Clouter, M. J. *Phys. Rev. A* **41**, 2239 (1990).
- [3] Wegdam, G. H., Bot, A., Schram, R. P. C., and Schaink, H. M. *Phys. Rev. Lett.* **63**(25), 2697 (1989).
- [4] Boon, J. P. and Yip, S. *Molecular Hydrodynamics*. McGraw-Hill International Book Company, New York, (1980).
- [5] Mori, H. *Prog. Theor. Phys.* **33**, 423 (1965).
- [6] Bryk, T., Mryglod, I., and Kahl, G. *Phys. Rev. E* **56**, 2903 (1997).
- [7] Goldman, E. and Sirovich, L. *Phys. Fluids* **10**(9), 1928 (1967).
- [8] R.J.Huck and Johnson, E. A. *Phys. Rev. Lett.* **44**(3), 142 (1979).
- [9] Chapman, S. and Cowling, T. G. *The Mathematical Theory of Non-Uniform Gases*. Cambridge University Press, New York, (1960).
- [10] Goebel, C. J., Harris, S. M., and Johnson, E. A. *Phys. Fluids* **33**, 423 (1965).
- [11] Campa, A. and Cohen, E. G. D. *Phys. Rev. Lett* **61**(7), 853 (1988).

BIBLIOGRAPHY

- [12] Campa, A. and Cohen, E. G. D. *Phys. Rev. A* **41**(10), 5451 (1990).
- [13] Miyazaki, K. *Phys. Lett. A* **409-413**, 409 (1997).
- [14] Montfrooij, W., Westerhuijs, P., de Haan, V. O., and de Schepper, I. M. *Phys. Rev. Lett.* **63**, 544 (1989).
- [15] Westerhuijs, P., Montfrooij, W., de Graaf, L. A., and de Schepper, I. M. *Phys. Rev. A* **45**, 3749 (1992).
- [16] Sampoli, M., Bafle, U., Guarini, E., and Barocchi, F. *Phys. Rev. Lett.* **88**(8), 085502 (2002).
- [17] Alvarez, M., Bermejo, F. J., Verkerk, P., and Roessli, B. *Phys. Rev. Lett.* **80**, 2141 (1989).
- [18] Montfrooij, W., Verkerk, P., and Schepper, I. D. *Phys. Rev. A* **33**(1), 540 (1985).
- [19] Bove, L. E., Formisano, F., and Guarini, E. *Europhys. Lett.* **79**(1), 16002 (2007).
- [20] Anento, N., Gonzales, L., González, D. J., Chushak, Y., and Baumketner, A. *Phys. Rev. E* **70**, 041201 (2004).
- [21] Bencivenga, F., Cunsolo, A., Krisch, M., Monaco, G., Ruocco, G., and Sette, F. *Phys. Rev. E* **75**, 051202 (2007).
- [22] Monaco, G., Cunsolo, A., Ruocco, G., and Sette, F. *Phys. Rev. E* **60**, 5505 (1999).
- [23] Cunsolo, A., Pratesi, G., Rosica, F., Ruocco, G., Sampoli, M., Sette, F., Verbeni, R., Barocchi, F., Krisch, M., Masciovecchio, C., and Nardone, M. *J. Phys. and Chem. of Solids* **61**(3), 477 (2000).

- [24] V.F.Sears. *Phys. Rev. A* **7**(1), 340 (1973).
- [25] Hansen, J. and McDonald, I. *Theory of Simple Liquids*. Accademic Press, New York, (1976).
- [26] McGreevy, R. L., Mitchell, E. W., and Margaca, F. M. A. *J. Phys C: Solid State Phys.* **17**, 775 (1984).
- [27] Copley, J. R. D. and Dolling, G. *J. Phys C: Solid State Phys.* **11**, 1259 (1978).
- [28] Bryk, T. and Mryglod, I. *Cond. Matt. Phys.* **6**(3(35)), 395 (2003).
- [29] Bryk, T. and Mryglod, I. *Phys. Rev. B* **71**, 132202 (2005).
- [30] Bryk, T. and Mryglod, I. *Chem. Phys. Lett.* **466**, 56 (2008).
- [31] Bryk, T., Mryglod, I., and Kahl, G. *Phys. Rev. E* **56**, 2903 (1997).
- [32] Bhatia, A. B. and Thornton, D. E. *Phys. Rev. B* **2**, 3004 (1970).
- [33] Faber, T. E. and Ziman, J. M. *Phylos. Mag.* **11**, 153 (1965).
- [34] Hove, L. V. *Phys. Rev.* **95**, 249 (1954).
- [35] Price, D. L. and Copley, J. R. D. *Phys. Rev. A* **11**, 2124 (1975).
- [36] Clark, N. A. *Phys. Rev. A* **12**(5), 2092 (1975).
- [37] Berne, B. J. and Pecora, R. *Dynamic Light Scattering*. John Wiley, (1975).
- [38] Johnson, E. A. *J. Stat. Phys.* **57**(3/4), 647 (1989).
- [39] Balucani, U. and Zoppi, M. *Dynamics of the liquid state*. Clarendon Press, Oxford, (1994).
- [40] Sette, D. *Encyclopedia of Physics*. edited by S. Flugge, Vol. 'Acoustic I and II'(Springer-Verlag, Berlin), (1998).

BIBLIOGRAPHY

- [41] Herzfeld, E. and Litovitz, T. A. *in Absorption and Dispersion of Ultrasonic Waves*. Accademic Press, New York, (1959).
- [42] Copley, J. R. D. and Lovesey, S. W. *Rep. Prog. Phys.* **38**, 461 (1975).
- [43] Abramo, M. C., Parrinello, M., and Tosi, M. P. *J. Phys. C: Solid State Phys.* **7**, 4201 (1974).
- [44] Dirac, P. *The principles of quantum mechanics*. Oxford University Press, (1958).
- [45] Pike, E. and Sarkar, S. *The quantum theory of radiation*. Oxford University Press, (1995).
- [46] *International tables for crystallography*. Kluwer Academic Publishers, (2004).
- [47] Krisch, M. *J. Raman Spectrosc.* **34**, 628 (2003).
- [48] Zachariasen, H. *Theory of X-ray Diffraction in Crystals*. Dover, New York, (1944).
- [49] Hildebrand, G. *Acta Cryst. A* **35**, 696 (1979).
- [50] Verbeni, R., Sette, F., Krisch, M. H., Bergmann, U., Gorges, B., Halcoussis, C., and C. Masciovecchio, K. M., Ribois, J. F., Ruocco, G., and Sinn, H. *J. Synchrotron Radiat.* **3**, 62 (1996).
- [51] Masciovecchio, C., Bergmann, U., Krisch, M., Ruocco, G., Sette, F., and Verbeni, R. *Nucl. Instrum. Methods B* **111**, 181 (1996).
- [52] Masciovecchio, C., Bergmann, U., Krisch, M., Ruocco, G., Sette, F., and Verbeni, R. *Nucl. Instrum. Methods B* **117**, 339 (1996).
- [53] Glinka, C., Rowe, J., and Rock, J. L. *J. Appl. Crystallogr.* **19**, 427 (1986).

- [54] Petrillo, C., Guarini, E., Formisano, F., Sacchetti, F., and Babucci, E. *Nucl. Instr. and Meth. A* **489**, 304 (2002).
- [55] Lagarias, J. C., Reeds, J. A., Wright, M. H., and Wright, P. E. *SIAM Journal of Optimization* **9**(1), 112 (1998).
- [56] Coleman, T. F. and Li, Y. *SIAM Journal on Optimization* **6**, 418 (1996).
- [57] Coleman, T. F. and Li, Y. *Mathematical Programming* **67**(2), 189 (1994).
- [58] Cunsolo, A. *Relaxation Phenomena in the THz Dynamics of Simple Fluids Probed by Inelastic X-Ray Scattering, PhD Thesis* (1999).
- [59] Ailawadi, N. K., Rahman, A., and Zwanzig, R. *Phys. Rev. A* **4**, 1616 (1971).
- [60] Cunsolo, A., Pratesi, G., and Verbeni, R. *J. Chem. Phys.* **114**, 2259 (2001).
- [61] Hirschfelder, J. O. and Curtiss, C. F. *Molecular theory of gases and liquids*. John Wiley & Sons, (1954).
- [62] Fiocco, D. *private communication* .
- [63] Caccamo, G. *Physics Reports* **274**(1) (1996).
- [64] Gillan, M. J. *Mol. Phys.* **38**, 1781 (1979).
- [65] Cunsolo, A., Pratesi, G., Rosica, F., Ruocco, G., Sampoli, M., Sette, F., Verbeni, R., Barocchi, F., Krisch, M., Masciovecchio, C., and Nardone, M. *J. Chem. Phys* **5**, 2020 (1996).
- [66] Clouter, M. J., Luo, H., Kiefte, H., and Zollweg, J. A. *Phys. Rev. A* **41**(9), 1989 (2005).
- [67] Gaskell, T. and Miller, S. *J. Phys. C: Solid State Phys.* **11**, 3749 (1978).

BIBLIOGRAPHY

- [68] Goldman, E. and Sirovich, L. *Phys. of Fluids* **10**(9), 1928 (1967).
- [69] Bonatto, J. R. and Jr, W. M. *J. Stat. Mech. P09014* **2005**(9), P09014 (2005).
- [70] Vidal, J. *Thermodynamique Pétrolière*. Technip, Paris, (1997).
- [71] Livesley, D. M. *J. Phys. C: Solid State Phys.* **16**, 2889 (1983).
- [72] Orecchini, A. *private communication* .
- [73] Pastore, G. and Smargiassi, E. *private communication* .
- [74] MINUIT, D.-C. *Computer 7600*. Interim Program Library.
- [75] Baranyai, A., Ruff, I., and McGreevy, R. L. *J. Phys. C: Solid State Phys.* **19**, 453 (1986).
- [76] Janz, G. *Molten Salts Handbook*. Academic Press, New York, (1967).
- [77] Schram, R. P. C., Wegdam, G. H., and Bot, A. *Phys. Rev. A* **44**(12), 8062 (1991).
- [78] Clouter, M. J., Luo, H., Kiefte, H., and Zollweg, J. A. *Phys. Rev. A* **41**(4), 2239 (1990).